

**High precision optical and near-infrared velocimetry with  
CARMENES**

Dissertation  
zur Erlangung des Doktorgrades  
an der Fakultät für Mathematik, Informatik und Naturwissenschaften  
Fachbereich Physik  
der Universität Hamburg vorgelegt von

Evangelos Nagel

Hamburg  
2019

---

|   |  |
|---|--|
| Gutachter der Dissertation:                     | Prof. Dr. Jürgen Schmitt<br>Prof. Dr. Ignasi Ribas   |
| Zusammensetzung der Prüfungskommission:         | Prof. Dr. Jochen Liske<br>Prof. Dr. Jürgen Schmitt<br>Prof. Dr. Robi Banerjee<br>Prof. Dr. Stefan Dreizler<br>Prof. Dr. Dieter Horns |
| Vorsitzende/r der Prüfungskommission:           | Prof. Dr. Jochen Liske   |
| Datum der Disputation:                          | 25.05.2020   |
| Vorsitzender Fach-Promotionsausschusses PHYSIK: | Prof. Dr. Günter H. W. Sigl  |
| Leiter des Fachbereichs PHYSIK:                 | Prof. Dr. Wolfgang Hansen  |
| Dekan der Fakultät MIN:                         | Prof. Dr. Heinrich Graener   |

---

## Abstract

The search for Earth-like planets in their habitable zones is one of the main goals in exoplanet research. When orbiting solar-like stars, these planets cause Doppler signals on the order of  $\sim 10 \text{ cm s}^{-1}$  over a period of roughly one year. For that reason planet searches started to focus on low-mass stars, where Doppler signals are larger and periods are shorter. A radial velocity based planet search campaign is conducted by CARMENES, which is a spectrometer that operates from the visual to the near-infrared wavelength range. Over a period of several years CARMENES monitors a sample of  $\sim 300$  M dwarf stars to detect low-mass planets in their habitable zones.

In the first part of this thesis I put the focus on how to improve the radial velocity precision of CARMENES by mitigating the effect of the Earth's atmosphere on the data. Beside stellar magnetic activity, telluric contamination is one of the main obstacles in achieving higher radial velocity precision. Synthetic transmission models of the Earth's atmosphere are an excellent alternative to other telluric correction methods. However, M dwarf stars exhibit numerous intrinsic features and fitting synthetic transmission models is quite problematic. Therefore, I developed a new method dubbed Template Division Telluric Modeling (TDTM), that is suited to disentangle telluric and stellar spectral components, to fit a transmission model, and to subsequently derive telluric-free spectra. The performance of the TDTM technique is demonstrated on visual and near-infrared CARMENES spectral time series of the fast rotating telluric standard star 109 Vir and the M3.5 V dwarf GJ 273.

To study the impact of the telluric correction on the achievable radial velocity precision, I applied the TDTM technique to observations of GJ 1012, a M4.0 V dwarf that shows a low level of radial velocity variability. The radial velocity precision was compared to that produced by the standard CARMENES radial velocity pipeline, which incorporates conservative masking of telluric lines. In the visual wavelength range it turned out that the radial velocity precision after the correction is comparable to that achieved using the telluric masking approach. The impact of the telluric correction is significantly higher in the near-infrared range, where the radial velocity scatter was decreased by almost a factor of two from  $9.5 \text{ m s}^{-1}$  to  $5.7 \text{ m s}^{-1}$ . These results imply that the impact of the telluric correction on radial velocity precision is negligible in the visual range. In the near-infrared regime, however, the proper treatment of telluric lines is crucial to fully exploit the potential of near-infrared spectrographs to measure low-amplitude radial velocities.

The second part of this thesis is an in-depth study of the detection and characterization of an extrasolar planetary system around the cool low-mass M dwarf star GJ 4276 using precise Doppler spectroscopy obtained with CARMENES. I studied the radial velocity variability of GJ 4276 and found a periodic signal at 13.35 days. Since M dwarf stars are among the magnetically most active stars, I examined various activity indicators to ensure that the radial velocity variation is not activity related.

After establishing the planetary origin of the radial velocity signature, I juxtaposed three Keplerian models, in particular, a single-planet with a circular orbit, a single-planet with an eccentric orbit, and two planets on circular orbits with a period ratio 2:1, and derived the best-fit orbital parameters. To compare the fit qualities I carried out likelihood ratio tests on the grounds of which the circular single-planet scenario was rejected. Based on my statistical analyses, I found that the eccentric single-planet solution is slightly preferred revealing an exoplanet with a minimum mass of  $\sim 16 M_{\oplus}$  with one of the most eccentric orbits known today. However, the two planet solution could not be excluded with high confidence. These results highlight a general problem inherent in radial velocity observations related to the model degeneracy between a single-planet eccentric orbit and two planets in circular orbits near the 2:1 mean-motion resonance.

---

## Zusammenfassung

Die Suche nach erdähnlichen Planeten in der habitablen Zone ist eines der Hauptziele der Exoplanetenforschung. Wenn sich Planeten um sonnenähnliche Sterne bewegen, verursachen sie über einen Zeitraum von etwa einem Jahr Dopplersignale in der Größenordnung von  $\sim 10 \text{ cm s}^{-1}$ . Aus diesem Grund wurde der zuletzt Fokus von Planetensuchen auf massearme Sterne gelegt, da bei diesen die Dopplersignale größer und die Umlaufperioden kürzer sind. Eine Suchkampagne, die auf der Radialgeschwindigkeitsmethode beruht, wird zurzeit von CARMENES durchgeführt. CARMENES ist ein Spektrometer, welches im optischen und nahinfraroten Wellenlängenbereich sensitiv ist. Über einen Zeitraum von mehreren Jahren beobachtet CARMENES eine Auswahl von  $\sim 300$  M Zwergen, um massearme Planeten in der habitablen Zone zu detektieren.

Im ersten Teil dieser Arbeit befasse ich mich mit der Verbesserung der Messgenauigkeit von Radialgeschwindigkeiten bei CARMENES, indem der Einfluss der Erdatmosphäre auf die Spektren verringert wird. Neben der stellaren magnetischen Aktivität gehört tellurische Kontamination zu einer der wesentlichen Hürden auf dem Weg zu einer höheren Messgenauigkeit von Radialgeschwindigkeiten. Synthetische Transmissionsmodelle der Erdatmosphäre sind eine ausgezeichnete Alternative im Vergleich zu anderen Methoden der tellurischen Korrektur. M Zwerge jedoch weisen eine große Anzahl von Spektrallinien auf, so dass sich das Fitten von Transmissionsmodellen als problematisch erweist. Daher habe ich eine neue Methode namens Template Division Telluric Modeling (TDTM) entwickelt, welche das tellurische und stellare Spektrum voneinander trennt, um anschließend ein Transmissionsmodell an das tellurische Spektrum zu fitten mit dem die tellurischen Linien korrigiert werden können. Die Fähigkeiten der TDTM Methode wird an optischen und nahinfraroten CARMENES Spektren von dem schnell rotierenden tellurischen Standardstern 109 Vir und dem M3.5 V Stern GJ 273 gezeigt.

Um den Einfluss der tellurischen Korrektur auf die Messgenauigkeit der Radialgeschwindigkeiten zu untersuchen, habe ich die TDTM Methode auf Spektren von GJ 1012 angewendet, einem M4.0 V Stern, der eine geringe Radialgeschwindigkeitsvariabilität aufweist. Die Messgenauigkeit wurde daraufhin mit der von der CARMENES Pipeline verglichen, welche auf der Ausgrenzung der tellurischen Linien basiert. Es hat sich herausgestellt, dass die Messgenauigkeit im optischen Wellenlängenbereich vergleichbar ist mit der durch die Abdeckung erzielten. Im Nahinfraroten hingegen hat sich die Messgenauigkeit signifikant erhöht. Die Streuung in den Radialgeschwindigkeiten wurde von  $9.5 \text{ m s}^{-1}$  auf  $5.7 \text{ m s}^{-1}$  um fast einen Faktor zwei verringert. Dieses Ergebnis verdeutlicht, dass der Einfluss der tellurischen Korrektur im Optischen vernachlässigbar klein ist. Im nahinfraroten Bereich hingegen ist die Korrektur der tellurischen Linien ein entscheidender Faktor, um das Potential von optischen und nahinfraroten Spektrographen voll auszuschöpfen und somit Radialgeschwindigkeitssignale mit kleinen Amplituden zu messen.

Der zweite Teil dieser Arbeit befasst sich mit der Detektion und Charakterisierung eines extrasolaren Planetensystems um den kühlen, massearmen M Zwerg GJ 4276. Ich habe die Variabilität der Radialgeschwindigkeit von GJ 4276 untersucht und ein periodisches Signal bei 13.35 Tagen entdeckt. Da M Zwerge zu den magnetisch aktivsten Sternen gehören, habe ich verschiedene Aktivitätsindikatoren untersucht, um sicherzustellen, dass die Radialgeschwindigkeitsvariation nicht von der Aktivität herrührt.

Nachdem das Radialgeschwindigkeitssignal auf einen Planeten zurückgeführt werden konnte, habe ich drei Keplermodelle betrachtet: eines mit einem Planeten auf einer Kreisbahn, eines mit einem Planeten auf einer exzentrischen Bahn, und eines mit zwei Planeten auf Kreisbahnen in einem Umlaufverhältnis von 2:1. Von diesen Modellen habe ich die am besten passendsten Bahnelemente bestimmt. Um die Fitqualitäten zu vergleichen, habe ich Likelihood-Quotienten-Tests durchgeführt, aufgrund dessen das Modell mit einem Planeten auf einer Kreisbahn verworfen wurde. Meine statistischen Analysen haben ergeben, dass das Modell mit einem Planeten auf einer exzentrischen Bahn leicht zu bevorzugen ist. Dieses ergibt für den Planeten um GJ 4276 eine minimale Planetenmasse

---

von  $\sim 16M_{\oplus}$  und eine Exzentrizität, die mit zu den höchsten heute bekannten zählt. Das Modell mit den zwei Planeten kann jedoch nicht mit hinreichender Wahrscheinlichkeit ausgeschlossen werden. Die Resultate verdeutlichen ein generelles Problem von Radialgeschwindigkeitsmessungen bezüglich der Entartung eines Modells mit einem Planeten auf einer exzentrischen Bahn und dem zweier Planeten auf Kreisbahnen in einem Umlaufverhältnis von 2:1.

---

# Contents

|          |  |           |
|----------|--|-----------|
| <b>1</b> | <b>Introduction</b>  | <b>9</b>  |
| <b>2</b> | <b>Exoplanets</b>  | <b>13</b> |
| 2.1      | Exoplanet definition . . . . .   | 13        |
| 2.2      | Exoplanet detection methods . . . . .  | 13        |
| 2.2.1    | Radial velocity method . . . . .   | 14        |
| 2.2.2    | Photometry and transits . . . . .  | 17        |
| 2.2.3    | Direct imaging . . . . .   | 19        |
| 2.2.4    | Microlensing . . . . .   | 21        |
| 2.2.5    | Astrometry . . . . .   | 22        |
| 2.3      | Occurrence rates . . . . .   | 22        |
| <b>3</b> | <b>Planethunting with CARMENES</b>   | <b>25</b> |
| 3.1      | Instrument . . . . .   | 25        |
| 3.2      | Wavelength calibration . . . . .   | 25        |
| 3.3      | CARMENES exoplanet survey . . . . .  | 26        |
| 3.4      | Radial velocity measurement techniques . . . . .   | 28        |
| 3.5      | Stellar activity indicators . . . . .  | 29        |
| 3.6      | Radial velocity precision and stellar noise . . . . .  | 31        |
| 3.7      | Radial velocity study of the planetary system GJ 4276 . . . . .  | 33        |
| <b>4</b> | <b>Telluric contamination</b>  | <b>35</b> |
| 4.1      | Telluric correction techniques . . . . .   | 35        |
| 4.2      | Impact on Radial velocity . . . . .  | 37        |
| 4.3      | Telluric correction in CARMENES . . . . .  | 39        |
| <b>5</b> | <b>Publications</b>  | <b>41</b> |
| 5.1      | Overview . . . . .   | 41        |
| 5.1.1    | My contributions . . . . .   | 41        |
| 5.1.2    | Publication status . . . . .   | 42        |
| 5.2      | The template division telluric modeling technique and its application to optical and near-infrared radial velocities . . . . . | 43        |
| 5.3      | The enigmatic planetary system GJ 4276: one eccentric planet or two planets in a 2:1 resonance? . . . . .                      | 59        |
| 5.4      | Further publications . . . . .   | 73        |

**6 Summary**

**77**



# 1 Introduction

The advent of robotic spacecrafts has dramatically increased our knowledge of the planets in the Solar System. Since then we know that each of the planets is quite unique. With temperatures that allow liquid water on the surface and an atmosphere that protects the surface from high energy radiation, only the Earth provides conditions for human life. Other examples are Saturn's huge ring system composed of countless numbers of icy and rocky particles and the retrograde rotation of Venus.

Until the mid 90's astronomers established a theory of the formation and evolution of the Solar System based on fundamental physical and chemical laws and observations of the Solar System constituents. It was believed that rocky terrestrial planets have orbits close to their host star and gas giants orbit farther out. However, it was impossible to decide whether the major properties of the Solar System were essential properties of any system because only the Solar System was known (e.g. Williams & Cremin 1968). With the detection of the first extrasolar planet around a solar-like star in 1995, the situation has fundamentally changed (Mayor & Queloz 1995).

The discovery of 51 Peg b in 1995 was a breakthrough in the search for extrasolar planetary systems. At a distance of 14.7 pc and with a mass of  $0.47 M_J$  51 Peg b has an orbital period of 4.2 d and a semi-major axis of 0.053 AU, placing it within the orbit of Mercury. This was very surprising because planet formation models predict that gas giants could not form that close to their host star and that 51 Peg b has probably formed at a larger distance ( $\sim 5$  au) and subsequently migrated inwards through interactions with the material of the circumstellar disk (Lin et al. 1996).

In the last two decades thousands of exoplanets have been discovered beyond our Solar System. At the time of writing, 4118 confirmed exoplanets and 671 multiplanet systems have been reported ([exoplanet.eu](http://exoplanet.eu), accessed: 2019-10-09) and the number steadily increases on a weekly basis. Very recently, the Royal Swedish Academy of Sciences awarded the Nobel Prize in physics 2019 to Michel Mayor and Didier Queloz from the University of Geneva "for the first discovery of an exoplanet orbiting a solar-type star outside our Solar System" ([www.nobelprize.org](http://www.nobelprize.org), accessed: 2019-10-10).

Direct observations of extrasolar planets are extremely difficult because they are exceptionally small by virtually every physical measure, especially when compared to their host stars. Considering a Jupiter-like planet and a solar-like star, the size ratio is 1 to 10, the mass ratio is 1 to  $10^3$ , and the flux ratio in the visible is 3 to  $10^9$  (National Academies of Sciences & Medicine 2018). The dissimilarity is even more extreme in the case of an Earth-like planet, where the size ratio is 1 to 100, the mass ratio 1 to  $3 \cdot 10^5$ , and the flux ratio 1 to  $2 \cdot 10^9$ . Except for detections obtained with direct imaging, the existence of planets are inferred indirectly, since most of our detection techniques are based on measurable effects that a planet induces on its host star.

Figure 1.1 shows the minimum mass and the semi-major axis for the known exoplanets that have been discovered by various methods. The diagram indicates that the mass and

semi-major axis parameter space is broadly populated with masses in the range of  $\sim 0.5 M_{\oplus}$  up to the brown dwarf regime at  $\sim 13 M_{\text{J}}$  and orbital periods ranging from hours up to hundreds of years. Many planetary systems harbor planets with characteristics that cannot be found in the Solar System, for instance, planets with close orbits heated to  $> 1000\text{K}$  (Howard 2013). The unpopulated parameter space at lower planet masses at larger orbital distances follows from observational biases and is a consequence of the survey durations, the sensitivity of the detection methods, and the sensitivity of the instruments. Except for Jupiter, the parameter space occupied by Solar System planets is empty, which means that our current knowledge of the exoplanet population is incomplete.

The diagram also illustrates the complementarity of the different detection methods. Each method explores different regimes of the planetary mass versus orbital distance diagram. Radial velocity and transit surveys are most sensitive to exoplanets with relatively short periods and distances of a few au. The instrumental precisions of such state of the art surveys are sensitive enough to detect Earth-like planets. In contrast, direct imaging surveys are sensitive to massive planets at large separations. To obtain a complete picture of the exoplanet population and its characteristics, the full arsenal of detection methods is required.

### **This thesis**

The focus of this thesis is on the analysis of high precision optical and near-infrared radial velocities from the CARMENES survey in the context of extrasolar planets. The thesis is divided into two parts that are independent from each other. At first I present my Template Division Telluric Modeling technique and its application to CARMENES spectra. The detection and characterization of the planetary system around GJ 4276 based on radial velocities obtained with CARMENES is presented afterwards.

Section 2 is an overview of exoplanet research. I introduce the different types of exoplanets followed by a description of current detection methods. Lastly I introduce our present knowledge on the exoplanet occurrence rate.

In Section 3 I present the CARMENES spectrometer and the CARMENES M dwarf survey before I focus on the impact of stellar activity on radial velocity measurements.

Section 4 is dedicated to telluric contamination. I introduce current correction techniques and summarize studies that investigated the impact of telluric contamination on radial velocity precision.

Section 5 is the main part of this thesis. Here I present my contributions to the CARMENES project that culminated into two publications.

I finally summarize my findings and the main conclusions in Section 6.

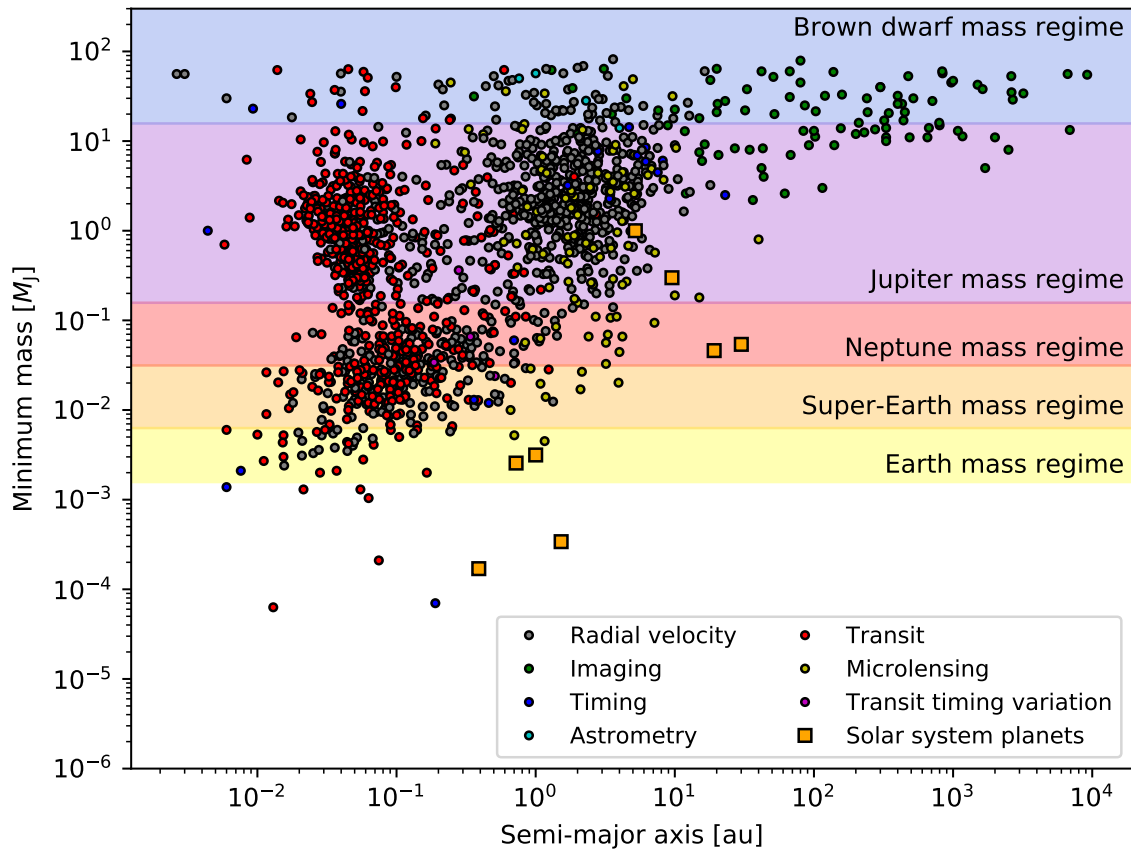


Figure 1.1: Minimum mass as a function of semi-major axis for the exoplanets known as of October 2019 (circles). The colors indicate the detection method. The planets of the Solar System are indicated by the yellow squares. From left to right the squares correspond to Mercury, Venus, Earth, Mars, Jupiter, Saturn, Uranus, and Neptune.



# 2 Exoplanets

## 2.1 Exoplanet definition

There is no official definition for exoplanets and the different types of exoplanets. An exoplanet is simply a body with a mass below the deuterium-burning limit of roughly  $13M_J$ , that orbits around a star other than our Sun. However, several terms based on exoplanet properties are established within the exoplanet community.

Giant planets are bodies that are primarily composed of hydrogen and helium without solid or liquid surfaces. When gas giants are located very close to their host stars, typically within 0.1 au with orbital periods  $< 10d$ , they are referred to as hot Jupiters. A secondary type of giant planets exist in our Solar System, the so-called ice giants. Below the outer hydrogen envelope, that is smaller in size compared to that of gas giants, ice giants have a mantle consisting of water, ammonia, or methane. In the context of exoplanets, planets with masses in the range of  $10 - 25M_{\oplus}$  are typically referred to as Exo-Neptunes.

Apart the giant planets, the Solar System harbors terrestrial planets. These planets are primarily composed of silicate rocks or metals and can have a thin gaseous atmosphere. From theoretical considerations, it is expected that terrestrial planets have masses smaller than  $5 - 10M_{\oplus}$  because larger planets likely capture gas during the accretion and develop into giant planets (Seager 2010). As a subcategory of terrestrial planets, the term Super-Earth describes planets with masses  $\sim 2 - 10M_{\oplus}$  with radii  $\leq 1.75R_{\oplus}$ . The smallest planets in terms of mass and radius with properties similar to the Earth of approximately  $1M_{\oplus}$  and  $1R_{\oplus}$  are dubbed Earth-like planets.

Of particular importance in exoplanet research are rocky planets that are located within the habitable zone of a star. The habitable zone is a range of distances from a star, where a planet maintains surface water in a liquid form over a longer period of time. During the lifetime of main sequence stars, the habitable zone moves outwards because stars get brighter with time. The location of the habitable zone further depends on the spectral type. Habitable zones of massive hot stars are farther out compared to those of cool low-mass stars.

## 2.2 Exoplanet detection methods

Various methods to detect exoplanets have been developed in the last decades. The most important methods comprise Doppler measurements, transit observations, direct imaging, microlensing, and astrometry. In particular the radial velocity and the transit methods preferably detect massive planets with short orbital periods. The sensitivity of those methods further depends on the host stars. The radial velocity amplitude scales with the stellar mass as  $M_{\star}^{-2/3}$ , and the transit depth with the stellar radius as  $R_{\star}^{-2}$  (Cumming et al. 1999; Seager & Mallén-Ornelas 2003). In contrast, direct imaging and astrometry are more sensitive to

massive planets at larger star-planet separations. With a sensitivity for planets with masses greater than that of Mars at orbital distances greater than a few au, microlensing effectively complements the other methods. Altogether, the current detection methods in principle allow us to probe a wide parameter space including planets covering the mass range from rocky planets to gas giants at almost arbitrary distances around stars with spectral types from A to M placed at distances from the solar vicinity to a few kpc, and even free-floating planets.

### 2.2.1 Radial velocity method

A very prolific method to search for extrasolar planets is the radial velocity method. With this method several hundreds of exoplanets including single and multiple systems on orbits around nearby stars have been detected so far. Radial velocity follow-up observations of transiting exoplanet candidates are also essential to establish or exclude the planetary nature of these objects and to eliminate impostors among transit candidates. Significant milestone discoveries have been made based on radial velocity measurements, for instance hot Jupiters (Mayor & Queloz 1995), multiplanet systems (Butler et al. 1999), the planet-metallicity correlation (Fischer & Valenti 2005), and Proxima Centauri b, which is an Earth-like planet orbiting the closest star to the Sun within the habitable zone (Anglada-Escudé et al. 2016).

The basic idea behind the radial velocity method is rather simple. Objects such as planets, stars, and even galaxies move relative to the Earth with a certain velocity. Their radial velocity describes the velocity component of these objects towards to or away from the Earth. Due to the relative movement of the object, the Doppler effect causes a change in the wavelength of the spectral lines. By measuring the displacement of the spectral lines with respect to their laboratory reference wavelengths, it is possible to obtain the radial velocity of the object. If a star is now being orbited by a companion, a periodic radial velocity modulation will occur and reveal the presence of the body. This is the result of the periodic motion of the star and the planet around the system barycenter.

The first exoplanet that has been detected with the radial velocity method was 51 Peg b. Figure 2.1 shows the radial velocity curve of 51 Peg (Mayor & Queloz 1995) obtained with the ELODIE spectrograph (Baranne et al. 1996). The discovery of 51 Peg b was possible due to the unprecedented increase in precision reached by simultaneously monitoring the spectrograph using a second fiber illuminated by a Thorium-Argon lamp.

#### Orbital elements inferred from radial velocities

A three-dimensional Keplerian orbit can be described by seven parameters (Perryman 2011):

- the semi-major axis  $a$ ,
- the eccentricity  $e$ ,
- the orbital period  $P$ ,
- the time  $\tau$  that corresponds to the position of the planet with respect to a certain reference time (usually the time of the periastron passage)
- the orbit inclination  $i$ , which is the angle between the orbit plane and a reference plane (the reference plane is usually the sky plane in the context of exoplanets),

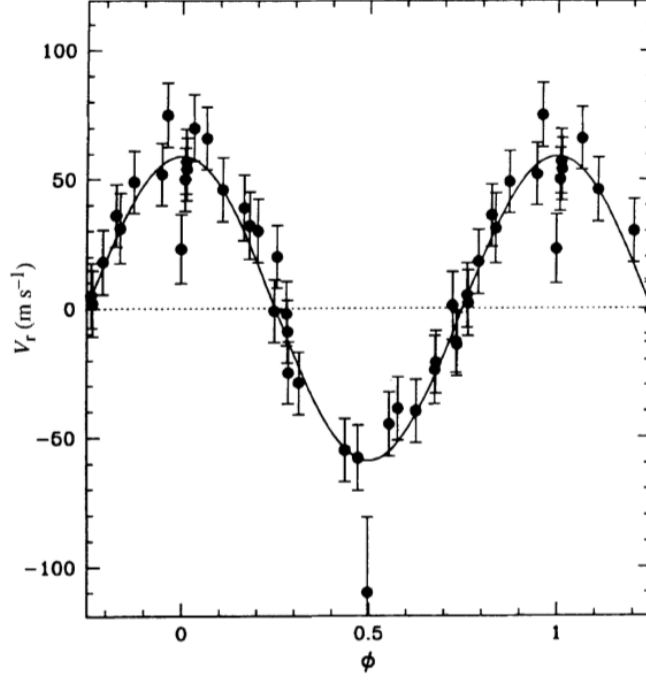


Figure 2.1: Phase-folded radial velocity measurements of 51 Peg, the first exoplanet discovery orbiting a Sun-like star. The black curve indicates the best-fit model. From Mayor & Queloz (1995).

- the argument of periastron  $\omega$ , which is the angle between the periastron direction and the ascending node through the reference plane,
- and the longitude of the ascending node  $\Omega$ , which is the angle between the reference direction and the direction of the ascending node both measured in the reference plane.

The size and the shape of a Keplerian orbit is characterized through the semi-major axis  $a$  and the eccentricity (left panel of Fig. 2.2). The orbital period  $P$  is related to the semi-major axis via Kepler's third law

$$P^2 = \frac{4\pi^2}{G(M_\star + M_p)} a^3, \quad (2.1)$$

where  $G$  is the universal gravitational constant,  $M_\star$  is the mass of the host star, and  $M_p$  is the mass of the planetary companion. The projection of the three-dimensional orbit into the observed two-dimensional plane is described by  $i$ ,  $\omega$ , and  $\Omega$ . The orbit inclination  $i = 90^\circ$  usually characterizes an edge-on orbit, while  $i = 0^\circ$  corresponds to a face-on orbit. The projected motion of a star moving around the system barycenter is specified by,  $z$  as illustrated in the right panel of Fig. 2.2. Using trigonometric relations, one can connect the radial velocity measurements to the radial velocity amplitude  $K$  via

$$v_{\text{rad}} = K[\cos(\omega + v) + e \cos(\omega)], \quad (2.2)$$

where  $v(t)$  is the true anomaly and  $K$  is expressed by

$$K^3 = \frac{2\pi G}{P} \frac{M_p^3 \sin^3 i}{(M_\star + M_p)^2} \frac{1}{(1 - e^2)^{3/2}}. \quad (2.3)$$

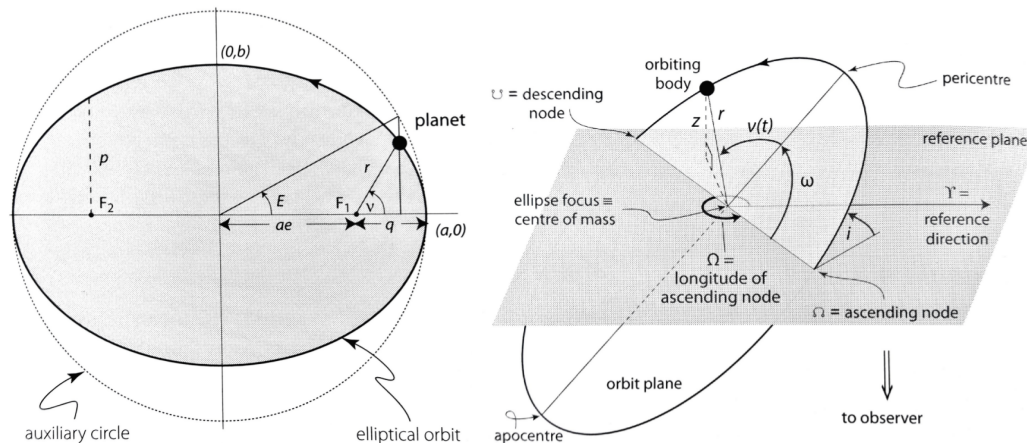


Figure 2.2: Two dimensional (left panel) and three dimensional (right panel) elliptical orbits illustrating the characteristic properties. From Perryman (2011).

With  $M_p \ll M_*$  the second factor of Eq. (2.3), which is dubbed as the mass function, can be simplified to

$$\frac{M_p^3 \sin^3 i}{(M_* + M_p)^2} \approx \frac{M_p^3 \sin^3 i}{M_*^2}. \quad (2.4)$$

Ultimately, only five parameters can be determined by fitting a Keplerian orbit to a radial velocity time series:  $e$ ,  $\omega$ ,  $P$ ,  $\tau$ , and  $K$ . From these parameters, only the minimum planetary mass  $m \sin i$  can be determined. If the orbital inclination is known, for instance by transit observations, the absolute planetary mass can be inferred.

Equations (2.2) and (2.3) indicate that planets with high masses and short orbital periods orbiting less massive stars lead to higher radial velocity amplitudes and require less instrumental precision. For stellar mass companions  $K$  is in the order of  $\text{km s}^{-1}$ . However, an Earth-like planet orbiting a Sun-like star on a one year orbit produces a radial velocity signal with an amplitude of  $K = 9 \text{ cm s}^{-1}$ , which is beyond reach of current instrument precision. Apart from planetary properties, the radial velocity uncertainty depends on several factors. The uncertainty due to photon noise depends on the apparent magnitude of the star. The stellar information content is also critical and depends on the spectral type. Compared to solar-like stars, cool low-mass stars have a large amount of spectral features. However, cool stars are among the most active stars Schmitt et al. (1995). Those stars introduce a stellar jitter, which increase the radial velocity uncertainty.

### State of the art spectrometer

Numerous high-performance instruments that produce precise radial velocity measurements on a  $\text{m s}^{-1}$  level are operational at present. The most successful planet finder employing the radial velocity method is the HARPS<sup>1</sup> spectrograph (Mayor et al. 2003) with 173 planet discoveries so far<sup>2</sup>. HARPS is mounted on the 3.6 m telescope at La Silla and covers the southern sky. Its counterpart, HARPS-N (Cosentino et al. 2012), is installed on the 3.6 m TNG telescope at La Palma and observes the northern hemisphere. Another example is the

<sup>1</sup>High Accuracy Radial Velocity Planet Searcher

<sup>2</sup>Retrieved on 11 September 2019 from the Nasa Exoplanet Archive, <https://exoplanetarchive.ipac.caltech.edu/>



HIRES<sup>3</sup> spectrograph mounted on the 10 m Keck I telescope on Mauna Kea (Vogt et al. 1994) and the ESPRESSO<sup>4</sup> spectrograph installed on ESO's VLT (Pepe et al. 2010). The latter aims at reaching an instrumental radial velocity precision of  $10 \text{ cm s}^{-1}$  to study rocky exoplanets in the habitable zones around G to M dwarfs.

Equation (2.3) implies that the radial velocity amplitude is larger for planets orbiting low-mass stars. The fact that these cool stars emit their bulk energy in the near-infrared has led to the development of a new generation of spectrographs, which cover the near-infrared spectral range. The first high-resolution spectrograph that was specifically designed and built to probe a large sample of M dwarf stars is CARMENES (Quirrenbach et al. 2018). Comparable instruments have been recently constructed to tackle very similar scientific questions as CARMENES, for instance HPF<sup>5</sup> (Mahadevan et al. 2014), SPIRou (Artigau et al. 2014), and NIRPS<sup>6</sup>, which is the near-infrared counterpart of HARPS.

## 2.2.2 Photometry and transits

When the orientation of an exoplanetary orbit is almost perpendicular to the plane of the sky so that an observer on Earth sees the system edge-on, the light of the host star is periodically attenuated when the planet transits in front of its disk and causes a dip in the light curve (Fig. 2.3). The loss of the light reflected from the planetary surface as the planet moves behind the star causes a secondary eclipse. The drop in flux is even smaller than during the primary transit and very challenging to measure with ground-based facilities.

The first exoplanet transit was measured by Henry et al. (2000) and independently by Charbonneau et al. (2000) around the Sun-like star HD 209458 (Fig. 2.4). With a mass of  $M_p = 0.6 M_J$  and a radius of  $R_p = 1.3 R_J$ , HD 209458 b belongs to the class of highly irradiated hot Jupiters. While it was known from radial velocity observations that HD 209458 has a planetary companion and the transit was found by photometric follow-up, the first detection of an exoplanet via transit method was reported by Konacki et al. (2003).

Since then, ground-based automated transit searches conducted with wide-field telescopes and camera arrays such as HATNet<sup>7</sup> (Bakos et al. 2004), WASP<sup>8</sup> (Pollacco et al. 2006), and MEarth (Nutzman & Charbonneau 2008) monitor a large number of stars over a long period of time leading to continuous exoplanet discoveries.

The era of space-based observatories dedicated to the search for extrasolar planets began with the launch of the CoRoT<sup>9</sup> satellite in 2006 and Kepler in 2009 (Auvergne et al. 2009; Koch et al. 2010). Long continuous observations of a large sample of stars combined with the absence of the Earth's atmosphere, which limits the photometric accuracy due to scintillation and variable atmospheric extinction, have made the transit method one of the most effective and sensitive approach to exoplanet detection. Especially the Kepler mission has provided valuable insights into the diversity of exoplanets and their occurrence rate, and has revolutionized the field of exoplanets. The recently launched TESS<sup>10</sup> satellite and the up-

<sup>3</sup>High Resolution Echelle Spectrometer

<sup>4</sup>Echelle SPectrograph for Rocky Exoplanets and Stable Spectroscopic Observations

<sup>5</sup>Habitable Zone Planet Finder

<sup>6</sup>Near Infra Red Planet Searcher

<sup>7</sup>Hungarian Automated Telescope Network

<sup>8</sup>Wide Angle Search for Planets

<sup>9</sup>Convection, Rotation and planetary Transits

<sup>10</sup>Transiting Exoplanet Survey Satellite

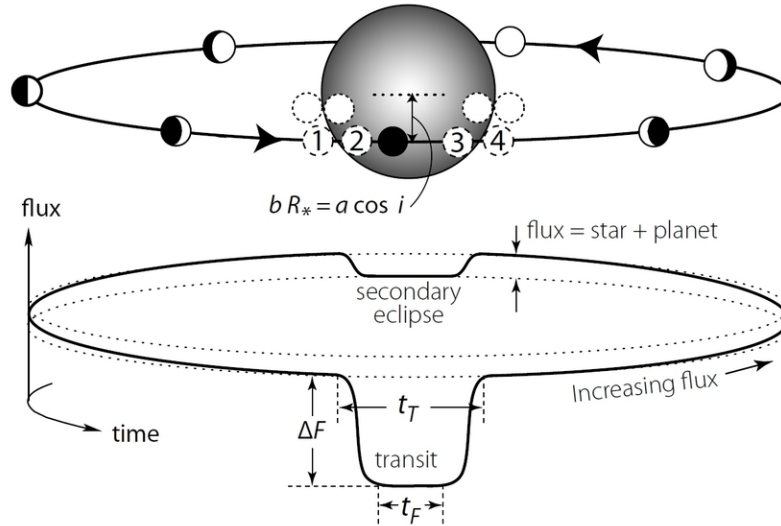


Figure 2.3: Illustration of a transit and a secondary eclipse. When the planet moves in front of the star a fraction of the stellar light is blocked and causes a dip in the light curve. When the planet moves around the star, the reflected light from the planet’s dayside causes an increase in the measured flux. When the planet moves behind the star the measured flux drops again due to the absence of the reflected light. The figure also indicates the four contact points of a transit. From Perryman (2011).

coming PLATO<sup>11</sup> and CHEOPS<sup>12</sup> missions will find and characterize numerous exoplanets, and will serve as pathfinders for spectroscopic follow-up missions measuring the structure and composition of the exoplanet atmospheres (Fortier et al. 2014; Rauer et al. 2014; Ricker et al. 2015).

### Parameters inferred from transit light curves

Four parameters can be directly measured from a transit light curve. Following the parametrization of Seager & Mallén-Ornelas (2003), the ratio of the planetary and stellar radius,  $R_P$  and  $R_*$ , can be derived from the transit depth  $\Delta F$  following the relation

$$\frac{\Delta F}{F} = \left( \frac{R_P}{R_*} \right)^2. \quad (2.5)$$

By measuring the time of the transit duration between the first and fourth contact  $t_T$  as well as the time of the fully occulted transit duration between the second and third contact  $t_F$ , the transit shape can be described with

$$\frac{\sin(t_F \pi / P)}{\sin(t_T \pi / P)} = \frac{\{[1 - (R_P / R_*)]^2 - [(a / R_*) \cos i]^2\}^{1/2}}{\{[1 - (R_P / R_*)]^2 - [(a / R_*) \cos i]^2\}^{1/2}}, \quad (2.6)$$

<sup>11</sup>PLANetary Transits and Oscillations of stars

<sup>12</sup>CHaracterising ExOPlanets Satellite

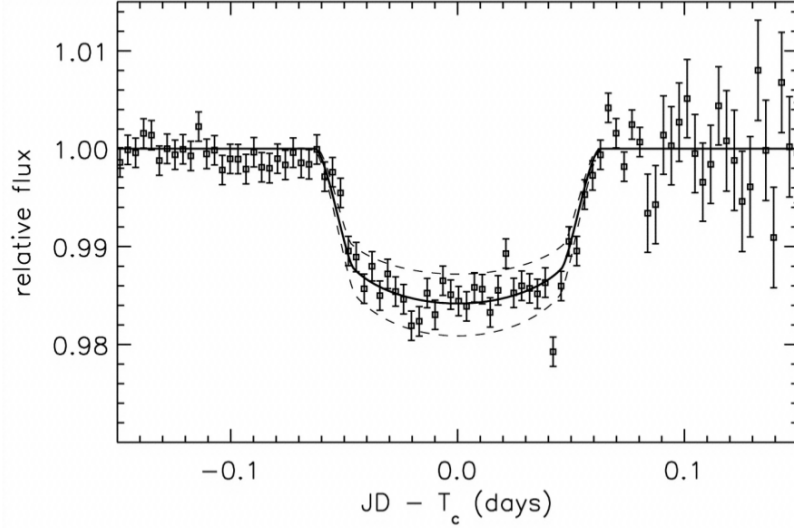


Figure 2.4: First observation of a transit light curve of HD 209458. The scatter at the end of the transit is due to increasing airmass. The solid curve indicates the best-fit model while the dashed lines are the transit curves assuming that the planetary radius is  $\pm 10\%$  larger and smaller, respectively. From Charbonneau et al. (2000).

where  $P$  is the orbital period,  $a$  is the semi-major axis, and  $i$  is the orbital inclination. Lastly, the total transit duration  $t_T$  can be inferred from the relation

$$\sin(t_T \pi / P) = \frac{R_\star}{a} \left( \frac{[1 + (R_P/R_\star)]^2 - [(a/R_\star) \cos i]^2}{1 - \cos^2 i} \right)^{1/2}. \quad (2.7)$$

Transits can only be observed in systems with nearly edge-on geometric configurations that fulfill the relation  $\cos i \leq (R_\star + R_P)/a$ . Assuming a randomly oriented planet on a circular orbit, the geometric probability of transit occurrence is given by

$$p \left( \cos i < \frac{R_\star + R_P}{a} \right) = \frac{R_\star + R_P}{a} \approx \frac{R_\star}{a}, \quad \text{with } R_\star \gg R_P, \quad (2.8)$$

hence,  $p$  increases for larger stellar radii and close-in planets. The transit probability of a Jupiter-like planet around a solar-like star with a radius of  $R_\star = R_\odot \approx 10^6$  km at a distance of  $a \approx 5$  au is 0.1 %, and 0.5 % for  $a \approx 1$  au. To overcome such low probabilities, thousands of stars must be monitored to discover transit events. For hot-Jupiters at  $a \approx 0.05$  au, however, the transit probability is about 10 %. Transit surveys are biased towards planets with short periods and large radii. For a given planet radius and period, low-mass stars produce deeper transit signals compared more massive stars because of their small size.

### 2.2.3 Direct imaging

The vast majority of exoplanets have been discovered with indirect detection techniques, where the presence of the planet is inferred from observations of the host star, either by measuring variations of the star's radial velocity or by measuring attenuations of the star's light when a planet moves across its disk. Those techniques are biased towards short-period close-in planets. The most practical technique to detect long-period planets at large orbital

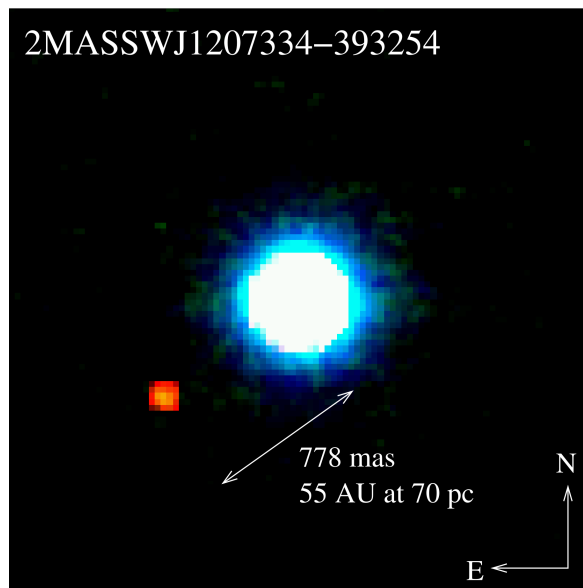


Figure 2.5: First exoplanet discovered with the direct imaging method. Imaged with the NACO adaptive optics instrument of the VLT, the image is a composition of three photometric bands ( $H$ ,  $K_S$ ,  $L'$ ). The planetary companion is clearly distinguishable from its host star in the lower left. From Chauvin et al. (2004).

separations in a reasonable amount of time is direct imaging. Measuring the reflected light from its host star in the visible or its thermal emission in the infrared results in a point source image of the exoplanet itself.

In the case of reflected light, the flux ratio of the planet and the star can be determined with the relation

$$\frac{f_P(\alpha, \lambda)}{f_*(\lambda)} = p(\lambda) \left( \frac{R_P}{a} \right)^2 g(\alpha), \quad (2.9)$$

where  $p(\lambda)$  is the geometric albedo,  $R_P$  is the planet radius,  $a$  is the semi-major axis, and  $g(\alpha)$  is the phase function (Perryman 2011). In the visible, the flux ratio is  $\sim 10^{-9}$  for a Jupiter-like planet around a solar-like star and the angular separation is 0.5 arcsec at a distance of 10 pc. Under these circumstances, direct imaging of most exoplanet systems remains out of reach with today's imaging facilities. However, exoplanets formed around young stars of up to 100 Myr have higher temperatures and are therefore more self-luminous at infrared wavelengths since they are still in phase of ongoing contraction. At  $\sim 5 \mu\text{m}$  the planet/star flux ratio can reach  $10^{-4}$  for distances of 0.2-15 au and masses of  $0.5 - 8 M_J$  (Burrows et al. 2004).

To overcome the technical challenges associated with direct imaging, numerous techniques have been developed to increase the achievable angular resolution and the contrast between the star and the planet. The use of telescopes with large apertures improves the signal-to-noise ratio (S/N) and spatial resolution. If the telescopes are equipped with adaptive optics, seeing effects from turbulent atmospheric refraction are minimized. By using coronagraph masks to block the light from the host star and post-processing techniques based on angular differential imaging and spectral differential imaging, the starlight is further suppressed.

The first direct imaging exoplanet orbiting a brown dwarf was discovered in 2004 by Chauvin et al. (2004). 2M1207 b has an estimated mass of  $\sim 5 M_J$  and orbits its host star in

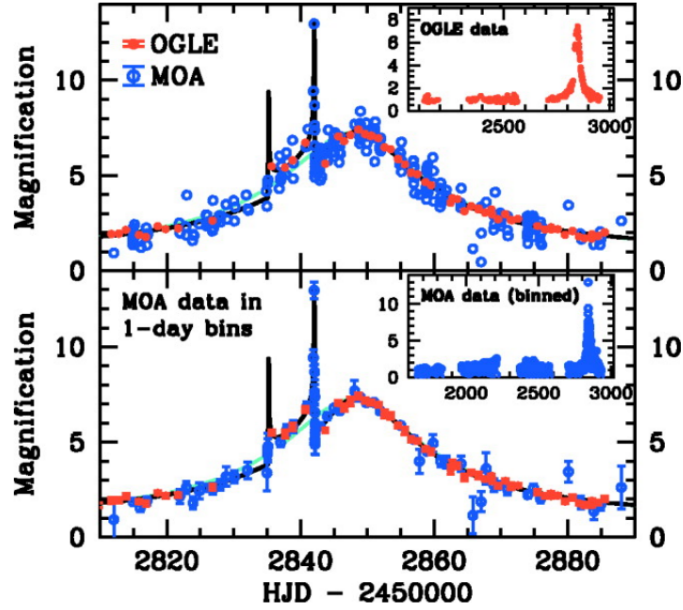


Figure 2.6: Microlensing light curve showing deviations from a planetary companion. The solid black and cyan lines indicate the binary- and single-lens fits. From Bond et al. (2004).

a projected separation of 55 au (Fig. 2.5). Due to the technical challenges only a few dozens exoplanets have been discovered so far with direct imaging. However, such observations play an important role in the field of exoplanets since they complement other detection techniques that are most sensitive to planets with small orbits.

## 2.2.4 Microlensing

According to Einstein’s theory of general relativity, the presence of a massive object causes a curvature in space time. This curvature deflects the light rays coming from a distant background object. This effect is known as gravitational lensing. The light from the background source appears in multiple distorted images around the foreground object, which acts as a lens. In case of perfect alignment between source and lens, the distorted light from the source appears as a ring of light. When both the background source and the lens are stars, the distorted images cannot be resolved with current instruments because the angular distances between the images are on the order of milli-arcseconds (Tsapras 2018). However, the variation in the brightness of the source can be measured. A microlensing event is usually observed as an increase in the brightness of the source star as the lens moves along the sky plane, followed by a decrease of the brightness as the lens moves away. If the star that acts as a lens harbors a planet, the planet itself can distort the light from the lensed star causing an anomaly in the light curve.

The first exoplanet detected by a microlensing event was reported by Bond et al. (2004). Figure 2.6 shows the light curve of this event over a time span of more than two months with the typical long-term behavior of single point mass microlensing events. The two spikes indicate an extreme mass ratio binary lensing system with a mass ratio of 0.0039. Assuming a main sequence primary, they derived for the secondary a mass of  $\sim 1.5 M_J$  at an orbital distance of  $\sim 3$  au.

With a probability of  $10^{-8}$  per star, the chance to observe microlensing anomalies caused by planetary companions is extremely low (Tsapras 2018). With typical distances on the order of few kpc, microlensing planets are very far away and are therefore not suited for follow-up observations. However, the method is not biased to nearby stars or the type of the host star and can even detect planets that have been ejected from their system. Also, the perturbations in the microlensing light curves are not as sensitive to the planetary mass as it is for the radial velocity and transit method. Therefore, microlensing events are well-suited to detect low-mass planets at larger orbital distances. A prominent example was reported by Beaulieu et al. (2006), where a microlensing event revealed the presence of a Super-Earth with a mass of  $5.5 M_{\oplus}$  at an orbital distance of 2.6 au.

### 2.2.5 Astrometry

The astrometry method deals with the precise measurement of the star's apparent position in the plane of the sky. If a star is orbited by a planet, the two components will orbit around their mutual barycenter. To measure the reflex motion induced by a planet with a mass of  $5 M_J$  on a three year orbit on a solar-like star requires an accuracy of  $< 1$  milli-arcsec (Sahlmann et al. 2014). So far, only two exoplanet discoveries have been announced by Muterspaugh et al. (2010) and Sahlmann et al. (2014). Although the astrometry method is still far from fulfilling its potential,  $\mu$ arcsec accuracy is in sight. With an expected astrometric precision of  $10 \mu$ arcsec for the brightest stars, the Gaia mission is expected to deliver astrometric positions suitable to detect  $21\,000 \pm 6000$  long-period exoplanets with masses of  $1\text{--}15 M_J$  out to distances of 500 pc for the nominal 5 year mission (Gaia Collaboration et al. 2018; Perryman et al. 2014).

## 2.3 Occurrence rates

Most of the early radial velocity planet searches were focussed on G and K stars. Wright et al. (2012) studied the occurrence rate of hot Jupiters among 836 FGK dwarfs in the solar neighborhood. They reported a rate of  $1.2 \pm 0.4\%$ , a value that is consistent with the rate of  $1.2 \pm 0.2\%$  reported by Marcy et al. (2005). Jupiter-mass planets have also been detected at semi-major axes beyond the ice line, where gas giants are thought to form (e.g. Giguere et al. 2015). In the case of gas giants, the parameter space at orbital distances of 30 – 300 au has been populated by detections with the direct imaging method. Based on direct imaging observations of 384 young stars with masses between  $0.1$  and  $3.0 M_{\odot}$ , the occurrence rate of gas giants with masses of  $5 - 13 M_J$  is  $0.6_{-0.5}^{+0.7}$  (Bowler 2016). Interestingly, the occurrence rate of giant planets apparently depends on the metallicity of the host star. The so-called planet-metallicity correlation was firstly reported by Gonzalez (1997) and has been confirmed by Santos et al. (2004) and Fischer & Valenti (2005). Less than 3% of the stars with metallicities  $-0.5 < [\text{Fe}/\text{H}] < 0.0$  are surrounded by giant planets. At  $[\text{Fe}/\text{H}] > +0.3$  dex, however, the occurrence rate increases to 25%.

The occurrence rate of close-in planets with orbital periods of less than 50 d has been studied by Howard et al. (2010). Based on radial velocity measurements of 166 solar-like stars, the authors found an increasing planet occurrence with decreasing planet mass. Moreover, they predict that 23% of stars harbor a close-in planet in the mass range of  $0.5 - 2.0 M_{\oplus}$ . Similarly, Mayor et al. (2011) found that 50% of solar-like stars host planets in the mass range of Super-Earths and Neptune-like planets with  $< 30 M_{\oplus}$ , and orbital periods of less

than 100 d. The analysis of the Kepler GK dwarf target sample was examined by Burke et al. (2015). For planet radii,  $0.75 \leq R_p \leq 2.5R_\oplus$ , and orbital periods,  $50 \leq P \leq 300$  d, they measured an occurrence rate of 0.77 planets per star.

The planet radius distribution was examined by Fulton et al. (2017) using precise planetary radii for 2025 Kepler planets. A gap found at  $1.5 - 2.0R_\oplus$  splits the population of planets with orbital periods of less than 100 d into two populations. The authors concluded that Sub-Neptunes and Super-Earths are two different classes and that the detected bimodal distribution separates larger gas-rich planets from rocky planets with a thin or nonexistent atmosphere.

### Planetary occurrence rate of M dwarf stars

Much research in recent years has focused on the occurrence rate of planets around M dwarfs, because, for a given planet mass, the radial velocity amplitude increases with decreasing stellar mass, and therefore, exoplanets around low-mass stars are an obvious choice to reach down to the terrestrial planet range.

Based on HARPS observations of a volume-limited M dwarf sample encompassing 102 stars closer than 11 pc and magnitudes  $< 14$  mag, Bonfils et al. (2013) reported that Super-Earths ( $m \sin i = 1 - 10M_\oplus$ ) are very abundant with occurrence rates of  $0.36_{-0.10}^{+0.25}$  planets per star for orbital periods  $P = 1 - 10$  d and  $0.52_{-0.16}^{+0.50}$  for  $P = 10 - 100$  d. This is consistent with the occurrence rate of  $1.08_{-0.72}^{+2.83}$  reported by Tuomi et al. (2014), who re-analyzed UVES and HARPS radial velocities of 41 nearby M dwarfs. Although both studies yield consistent results, the stellar sample in both studies is rather small and their occurrence rate estimations are based on  $\sim 10$  detections.

With Kepler observations of thousands of M dwarf stars, the M dwarf planet occurrence rate was set on a more solid foundation. Based on the analysis of transit events in the Kepler light curves of 3897 cool stars with temperatures below 4000 K, Dressing & Charbonneau (2013) found an occurrence rate of  $0.90_{-0.03}^{+0.04}$  planets per star with radii in the range of  $0.5 - 4R_\oplus$  and periods shorter than 50 d. In a more recent study, Dressing & Charbonneau (2015) searched the full four-year Kepler data set for transiting planets and reported a cumulative planet occurrence rate of  $2.5 \pm 0.2$  planets per M dwarf with radii  $1 - 4R_\oplus$  and periods shorter than 200 d. Moreover, Ballard & Johnson (2016) stated that half of the M dwarf population even harbor five or more planets in coplanar orbits.

The situation is somewhat different for gas giants, which appear to be rare in M dwarf systems. Within the mass range of  $100 - 1000M_\oplus$  Bonfils et al. (2013) found an occurrence rate of  $< 1\%$  with periods  $P = 1 - 10$  d and  $0.02_{-0.01}^{+0.03}$  for  $P = 10 - 100$  d. The low occurrence rate has been confirmed by numerous studies, for instance by Johnson et al. (2007), who derived an occurrence rate of  $1.8 \pm 1.0\%$  for giant planets within 2.5 au, and (Endl et al. 2006), who found a value of  $< 1.27\%$  at a  $1\sigma$  level for close-in gas giants. In a recent study, the CARMENES collaboration extended the small sample of known giant exoplanets around M dwarfs by a giant planet with a minimum mass of  $0.46M_J$  on an eccentric orbit ( $e = 0.44$ ) with an orbital period of 204 d and a potential long-period candidate orbiting a very low-mass M5.5-type star (Morales et al. 2019).

Considering that M dwarfs are the most abundant type of star in the solar vicinity, the occurrence rate of planets orbiting these stars will dominate the mean planet occurrence rate around all stellar types.





# 3 Planethunting with CARMENES

## 3.1 Instrument

CARMENES (Calar Alto high-Resolution search for M dwarfs with Exoearths with Near-infrared and optical Echelle Spectrographs) is an instrument designed, built, and operated by a collaboration of 11 Spanish and German institutions. Mounted on the 3.5 m telescope of the Calar Alto Observatory in Spain, the two ultra-stable high-resolution spectrographs were specifically constructed to obtain high long-term stability for delivering high precision radial velocities on the order of  $1 \text{ m s}^{-1}$ . The visible-light spectrograph covers the wavelength range from  $0.52 \mu\text{m}$  to  $0.96 \mu\text{m}$  providing a spectral resolution of  $R = 94\,600$ . Its counterpart in the near-infrared covers the spectral range from  $0.96 \mu\text{m}$  to  $1.71 \mu\text{m}$  and has a resolution of  $R = 80\,400$ .

The optical design and layout of the spectrographs are very similar. The light is directed to the Cassegrain focus of the telescope, where it passes a dichroic beam splitter. Sent through a pair of optical fibers, light with wavelengths  $< 0.96 \mu\text{m}$  is fed to the visible-light spectrograph and light with wavelengths  $> 0.96 \mu\text{m}$  is fed to the near-infrared spectrograph. In each of the spectrographs, the light is dispersed by an échelle grating and the orders are separated by a grism cross-disperser. The opto-mechanical components of the spectrographs are mounted on optical benches that are enclosed inside vacuum tanks, which are located in temperature-controlled chambers. A thermal system keeps the temperature of the optical benches constant to within  $\pm 0.01 \text{ K}$  over 24 h. While the optical spectrograph is operated at room temperature, the near-infrared spectrograph is actively cooled down to 140 K to reduce the thermal background of the detector (Quirrenbach et al. 2016, 2018).

## 3.2 Wavelength calibration

An accurate wavelength calibration is crucial in order to measure tiniest wavelength shifts of the stellar spectrum. Once the dispersed light falls on the detector CCDs, its wavelengths cannot be directly inferred. Instead, the pixel positions must be converted into absolute wavelengths.

To perform the wavelength calibration of the CARMENES spectrographs three different hollow-cathode lamps (HCLs) are in use, namely a thorium-neon lamp (Th-Ne), an uranium-neon lamp (U-Ne), and an uranium-argon lamp (U-Ar). These lamps produce a dense forest of emission lines over the entire wavelength range. The properties of these lines can be measured in a laboratory and are gathered in line lists. However, several drawbacks arise from the use of HCLs. Figure 3.1 shows an excerpt of an U-Ar HCL exposure, in which the light from the HCL is fed into both fibers. Beside the limited number of lines, the irregular line distribution requires an interpolation of the wavelength solution in spectral ranges without lines resulting in an increase of the uncertainty in those pixels. Furthermore, the noble gas

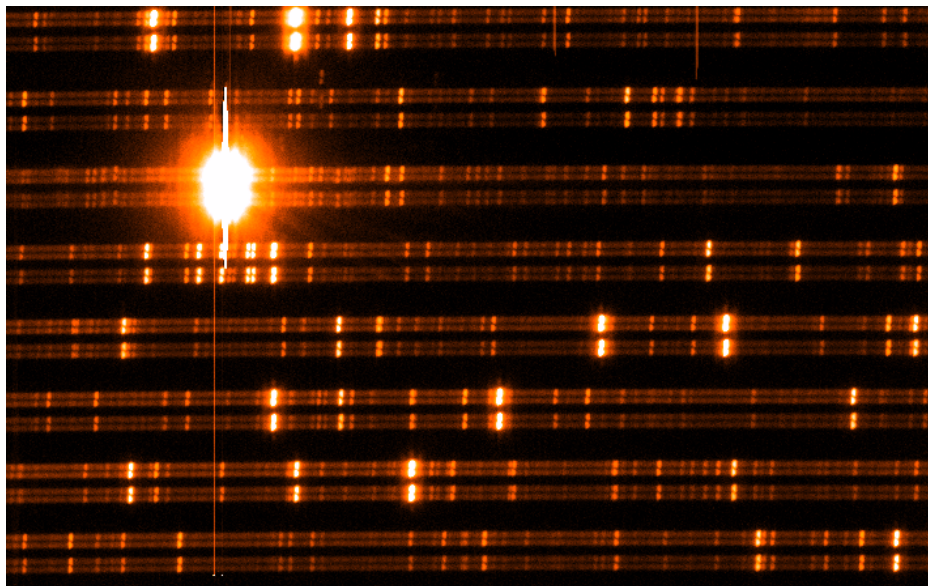


Figure 3.1: Excerpt of a U-Ar hollow-cathode lamp exposure obtained with the CARMENES visible-light spectrograph.

component emits very bright lines and hampers the simultaneous calibration of the stellar spectrum. To overcome problems introduced by the HCLs, the CARMENES spectrographs integrate a temperature stabilized Fabry-Pérot interferometer (FPI, Bauer et al. 2015). An FPI incorporates two partly transparent plane-parallel mirrors. Light rays passing the FPI are reflected between the two mirrors, interfere with each other, and produce a repetitive interference pattern. The transmission spectrum produces a repetitive interference pattern that shows maxima at wavelengths that fulfill the interference condition, which is a function of the distance between the two mirrors. The FP emission lines cover the entire wavelength range and therefore complement the wavelength calibration scheme of CARMENES together with the HCLs. Measured simultaneously with the science observations, the FP spectrum is used to monitor nightly short-term as well as long-term instrumental drifts. Figure 3.2 shows a segment of a raw frame exposure covering five orders. The equally spaced emission line pattern of the regular FP spectrum is placed below the stellar spectrum.

### 3.3 CARMENES exoplanet survey

The main scientific objective of CARMENES is to carry out a survey of roughly 300 cool low-mass stars during 750 Guaranteed Time Observation nights and to detect low-mass planets that are located in their habitable zones (Quirrenbach et al. 2016). As reported in Sect.2, statistical studies based on surveys conducted with HARPS and Kepler imply an occurrence rate of 1-2.5 planets per M dwarf that occupy the Earth and Neptune mass regime (Bonfils et al. 2013; Dressing & Charbonneau 2015). Jupiter-like planets are predicted to appear less frequent around M dwarfs (Laughlin et al. 2004). With the goal to gather  $\sim 60$  observations per star, the CARMENES data set will provide statistical information about the population of planets around these late-type stars, in particular the occurrence rate, their masses, and their orbital parameters. With a radial velocity precision of  $1 \text{ m s}^{-1}$ , CARMENES is able to reveal a  $2 M_{\oplus}$  planet in the habitable zone of a M5.0V star and a planet with  $5 M_{\oplus}$  or smaller in orbits around stars with spectral types later than M4.0V (Quirrenbach et al. 2016). These

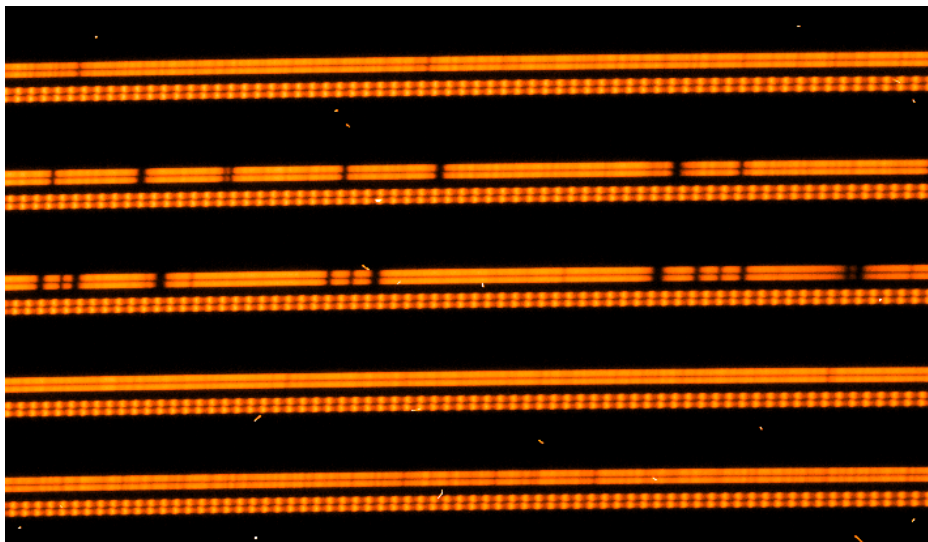


Figure 3.2: Excerpt of a CARMENES spectrum with simultaneous FPI calibration measurements.

limits are illustrated in Fig. 3.3, where the habitable zone is shown as a function of stellar mass and orbital distance for different masses and radial velocity precisions.

A secondary goal of the survey is to study the amount of spectral radial velocity information and the stellar jitter as a function of wavelength (Reiners et al. 2018b). By now, this goal has been accomplished. Based on the analysis of CARMENES spectra, it has been shown empirically that highest radial velocity precision can be reached in the wavelength range  $0.7 - 0.9 \mu\text{m}$  (Reiners et al. 2018b).

In order to maximize the scientific outcome of the CARMENES survey and to efficiently use the available telescope time, much effort has been put into a thorough analysis of possible target candidates. The parameters of almost 2200 M dwarfs in the solar vicinity brighter than  $J = 11.5$  mag and with declination  $\delta \leq -23^\circ$  were gathered from the literature and compiled in the Carmencita<sup>1</sup> database (Caballero et al. 2016). This database includes astrometric parameters (coordinates, parallaxes), kinematic parameters (proper motions, absolute radial velocities, galactocentric space velocities, secular acceleration, stellar kinematic group memberships), spectral types, fundamental stellar parameters ( $T_{\text{eff}}$ ,  $\log g$ ,  $[\text{Fe}/\text{H}]$ ,  $L$ ,  $R$ ,  $M$ ,  $v \sin i$ ), stellar population associations, rotation periods, activity indicators ( $\text{H}\alpha$  pseudo-equivalent widths,  $\log \text{H}\alpha/L_{\text{bol}}$ , X-ray count rates and hardness ratios), photometry ranging from ultraviolet to mid-infrared, and information on multiplicity (angular separations and information of the companions). In the course of the preparation of the final input catalogue, the spectral types, surface gravities, metallicities, and activity indices of 753 stars were determined using low-resolution optical spectroscopy with CAFOS at the 2.2 m Calar Alto telescope (Alonso-Floriano et al. 2015). Another preparatory study was carried out by Cortés-Contreras et al. (2017), who obtained high-resolution images in the  $I$  band of 490 M dwarfs with the lucky imaging instrument FastCam at the 1.5 m Telescopio Carlos Sánchez. Among the 490 targets, they found 80 gravitationally bound companions in 67 systems. The correlation of activity and rotation of the  $\sim 2200$  Carmencita targets were investigated by Jeffers et al. (2018), who obtained 1374 new high-resolution spectra for 480 M dwarf stars to measure projected rotational velocities  $v \sin i$  and  $\text{H}\alpha$  activity indices. Furthermore, they investigated the radial velocities of their sample to search for possible stellar companions.

<sup>1</sup>CARMEN(ES) Cool dwarf Information and daTa Archive

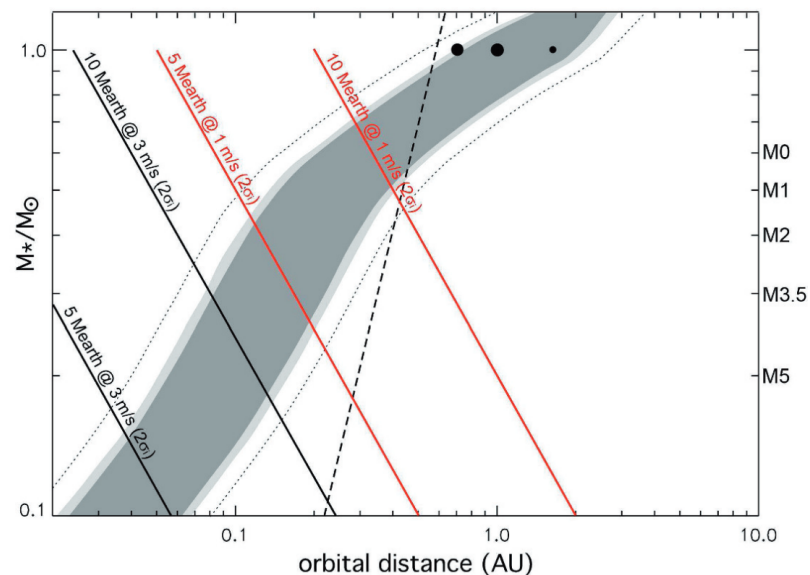


Figure 3.3: Location of the habitable zone (grey area) and its dependence on stellar mass. While the dashed line represents the tidal locking distance, the solid lines show  $5 M_{\oplus}$  and  $10 M_{\oplus}$  detection limits on a  $2\sigma$  significance level assuming  $1 \text{ m s}^{-1}$  (red) and  $3 \text{ m s}^{-1}$  (black) radial velocity precisions. The regions that can be probed by CARMENES are on the left side of the lines. The three black dots represent the location of Venus, Earth, and Mars. From Quirrenbach et al. (2010).

The final M dwarf GTO sample for the CARMENES survey was formed from the Carmencita database. M dwarf binaries for which the companion has an angular separation  $< 5''$  were excluded to ensure that radial velocity modulation is not induced by the companion. Within each spectral subtype the remaining targets were sorted by their apparent  $J$  band magnitude and only the brightest stars were chosen. Figure 3.4 shows the distribution of the Carmencita stars and the GTO stars as a function of spectral type.

### 3.4 Radial velocity measurement techniques

There are several algorithms to compute precise radial velocities. However, only three of them are implemented in the pipelines of current state of the art instruments all producing radial velocities on a  $\sim 1 \text{ m s}^{-1}$  level.

The cross-correlation function technique is a well-established and effective method to determine the relative Doppler velocity shifts between an externally wavelength calibrated stellar spectrum and a template (Baranne et al. 1996; Pepe et al. 2002; Tonry & Davis 1979). A binary mask, which serves as a template, is correlated with the stellar spectrum, whereas the non-zero chunks of the mask correspond to the laboratory positions and widths of the stellar absorption lines, and each non-zero chunk is weighted by the relative depth of the stellar line compared to the local continuum. The cross-correlation function (CCF) is then evaluated by shifting the mask as a function of Doppler velocity. The CCF is further a way to compress the information of the available spectral lines into a mean line. This mean line reflects the profile of an average stellar absorption line. The location of the minimum of the CCF corresponds to the relative velocity shift between the mask and the spectrum. The cross-correlation method is regularly applied for instance to HARPS and CORALIE

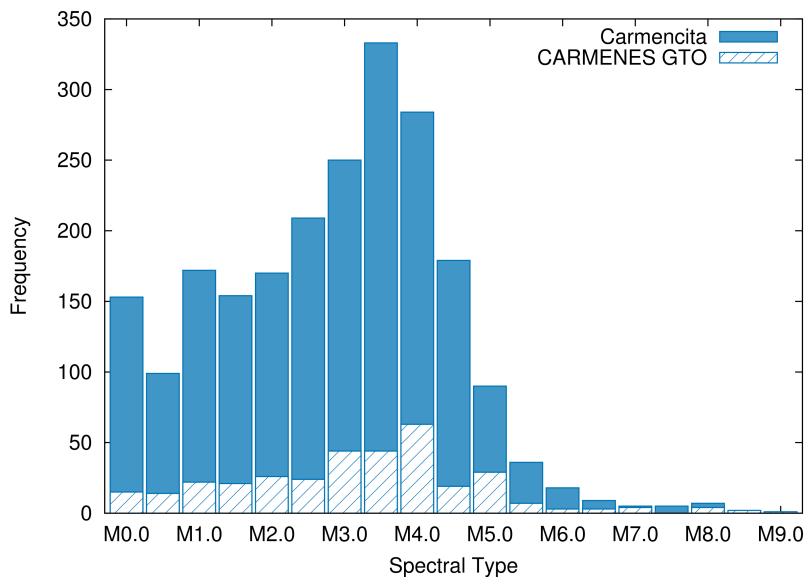


Figure 3.4: Spectral type distribution of Carmencita targets and the subsample that comprises the final CARMENES GTO sample. From Jeffers et al. (2018).

observations.

Another leading technique to derive precise radial velocities makes use of an absorption cell filled with iodine gas at low pressure. This gas cell is placed in front of the entrance slit of the spectrograph, and when the starlight passes the iodine cell prior to entering the spectrograph, the iodine spectrum is imprinted on top of the stellar spectrum. The forward-model developed by (Butler et al. 1996) incorporates a high S/N iodine transmission template multiplied by a high S/N stellar template and convolved with the instrumental broadening function. The free model parameters include the wavelength solution, the instrumental profile, and the star’s Doppler shift. Although it turned out that obtaining high-resolution perfectly calibrated stellar templates is one of the major limitations of this method, many spectrographs are equipped with absorption cells, for instance HIRES/Keck and PFS (Crane et al. 2010; Vogt et al. 1994). In addition, the field of application has been extended to the near-infrared wavelength range as demonstrated by Bean et al. (2010), who used an ammonia gas cell instead of an iodine cell.

In recent years, Anglada-Escudé & Butler (2012) proposed a method based on least-squares matching of an observed spectrum to a high S/N template spectrum of the same star created by co-adding all available spectra. The authors also demonstrated that this method yields higher accuracies compared to the CCF method when applied to M dwarf stars. This algorithm has been implemented in SERVAL, which is the standard radial velocity pipeline of CARMENES (Zechmeister et al. 2018).

### 3.5 Stellar activity indicators

Stellar activity indicators are frequently used to help in distinguishing planetary signals from radial velocity modulation caused by stellar activity. Any correlation between the radial velocity signature and the activity indicators suggests that the periodic variations originate from rotating spots, and casts serious doubts on the interpretation of a planetary induced

radial velocity variability. The examination of the activity indicators is therefore an integral component of every planet detection analysis.

If the lifetime of stellar spots is larger than the rotation period of the star, activity related radial velocity observations produce a periodic signal that mimic the presence of a planet. A prominent example is the young T Tauri star TW Hya. Setiawan et al. (2008) reported the detection of a planet with a mass of  $10M_J$  that showed radial velocity variations with a period of 3.56 d. Later it was shown by Huélamo et al. (2008) that the detected signal was associated with the presence of a cool stellar spot. It is important to ensure that radial velocity variation are not caused by stellar activity. For the analysis of the CARMENES stars, several spectral diagnostics are provided by the radial velocity pipeline SERVAL that are briefly introduced in the following.

The wavelength range covered by the visible channel of CARMENES includes four diagnostic lines that are sensitive to chromospheric activity, the Balmer  $H\alpha$  line at  $\lambda = 6562.8 \text{ \AA}$  and the Ca II infrared triplet (IRT) at  $\lambda = 8498 \text{ \AA}$ ,  $\lambda = 8542 \text{ \AA}$ , and  $\lambda = 8662 \text{ \AA}$ . As described in Kürster et al. (2003) and Zechmeister et al. (2018) the line indices are computed as

$$I = \frac{\langle f_0 \rangle}{0.5 \cdot (\langle f_1 \rangle + \langle f_2 \rangle)}, \quad (3.1)$$

where  $\langle f_0 \rangle$  is the mean flux in an interval around the line center and  $\langle f_1 \rangle$  and  $\langle f_2 \rangle$  are the mean fluxes in an nearby reference wavelength interval.

A novel spectral diagnostic was introduced by Zechmeister et al. (2018) taking advantage of the large wavelength coverage of CARMENES. The chromatic index is defined as the radial velocity gradient as a function of wavelength (Fig.3.5). It is based on the assumption that active regions are cooler or hotter than the photosphere. Therefore, the contrast to the photosphere is lower in longer wavelengths. As shown by Reiners et al. (2010), the temperature contrast between spots and photosphere induces a radial velocity signal that becomes weaker at longer wavelengths. This wavelength dependent radial velocity variation is captured by the chromatic index.

Additional activity indicators can be inferred from the analysis of the CCF. The CCF can be interpreted as the profile of an average stellar absorption line. Variations of the line shape in a spectral time series hint at the presence of radial velocity variability induced by stellar activity. In SERVAL, the CCF is computed using a weighted binary mask that was built from the template spectrum of the star itself (Reiners et al. 2018a). A Gaussian function is then fitted to the CCF to analyse the properties of the CCF, in particular the full width at half maximum (FWHM), the amplitude (usually referred to as the CCF contrast), and the bisector span. When active regions cross the stellar disc, the CCF parameters change in a characteristic manner. For example, a spot on the stellar surface produces a change of the CCF contrast in addition to variations in the CCF bisector or CCF FWHM. Asymmetries in the line profile can be quantified with the line bisector. In cool stars, solar-like granulation causes a C-shaped bisector. More insights about the nature of the photospheric velocity fields that distort the CCF line shape can be inferred from the covered velocity span and the absolute wavelength position. Moreover, they provide physical information about velocity fields that vary in depth since the line cores are formed higher in the photosphere than the line wings (Gray 2005).

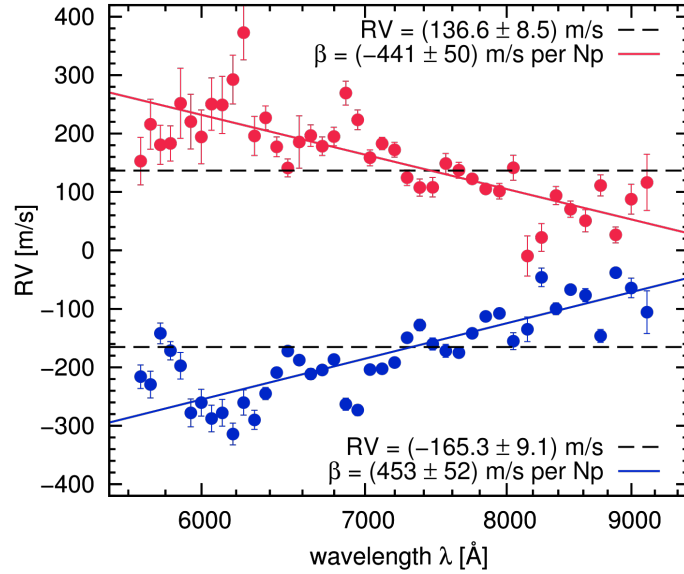


Figure 3.5: Orderwise measured radial velocities for two observations of YZ CMi obtained with the visible CARMENES channel. The dashed black line indicates the weighted mean radial velocity of the two observations and the solid red and blue lines indicate the chromatic index. From: Zechmeister et al. (2018).

### 3.6 Radial velocity precision and stellar noise

During the last decades the instrumental radial velocity precision has been improved from  $\sim 15 \text{ m s}^{-1}$  in the 1980s, to  $\sim 3 \text{ m s}^{-1}$  in the 1990s, and to a  $\text{cm s}^{-1}$  level today (Butler et al. 1996; Campbell & Walker 1979; Pepe et al. 2010). A radial velocity precision of  $10 \text{ cm s}^{-1}$  corresponds to a displacement of a few silicon atoms on the CCD detector (Fig. 3.6) and therefore requires hardware (in particular mechanical and thermal stability) and software based techniques to preserve the required metrological stability over years. The increase of the radial velocity precision has been accomplished by the development of innovative instrument designs and improvements in detector technology and wavelength calibration, for example by equipping spectrographs with laser frequency combs that produce a spectrum of discrete and equally spaced frequency lines generated from mode-locked femtosecond pulsed lasers.

Beside the precision limits set by the instrument, radial velocity precision also depends on the S/N. Precise radial velocity measurements are therefore limited by photon noise and radial velocity surveys are usually biased towards brighter stars. Typically, the integration time of CARMENES observations is such that a photon noise limit of  $1\text{-}2 \text{ m s}^{-1}$  is achieved (Quirrenbach et al. 2018).

The achievable radial velocity precision is further constrained by the star itself. The stellar information content is defined by the amount of spectral information that is available in a certain wavelength interval and can be used to measure the Doppler shift. In cool low-mass stars, spectral lines produced by atomic and molecular electronic transitions in the optical typically outnumber the lines in the near-infrared leading to a higher radial velocity information content in the optical compared to the near-infrared. For very late-type M8-M9 stars, however, the radial information is equal in both spectral ranges - a result that has been first demonstrated by CARMENES (Reiners et al. 2018b).

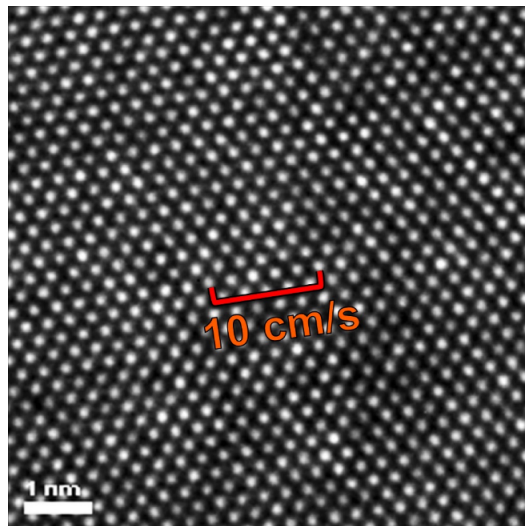


Figure 3.6: Transmission electron microscope image of a silicon wafer lattice. The shown segment corresponds to the size of  $1/1000^{\text{th}}$  CCD pixel. Credit: Sam Halverson.

Another limit of achievable radial velocity precision is set by stellar noise, which is a term comprising various phenomena that contribute jitter on characteristic timescales and amplitudes to radial velocity measurements. Stellar jitter can be introduced by stellar oscillations (minutes), surface granulation (hours), rotationally modulated inhomogeneities of the stellar atmosphere such as spots and plages (days to months), magnetic activity cycles (years), and even by unrecognized planetary companions (Perryman 2011; Plavchan et al. 2015).

Pressure waves propagating at the stellar surface manifest as dilatation and contraction of the external envelopes on timescales of 5-15 minutes for solar-like stars. Depending on spectral type and evolutionary stage, stellar oscillations cause radial velocity variations between  $10 \text{ cm s}^{-1}$  and  $4 \text{ m s}^{-1}$  (Dumusque et al. 2011). Stellar oscillation noise can be averaged out by adjusting the exposure times to time spans longer than the oscillation time scale. Also, the periods as well as the amplitudes of the oscillations decrease when going towards late-type stars leading to an even shorter exposure time to average them out.

Surface granulation is a phenomenon that can only be seen on the Sun but is expected to be present also on other stars. Granulation is caused by convective pattern with lifetimes of less than 25 minutes and sizes of about 2 Mm (Dumusque et al. 2011). Except at locations with spots, granules cover the entire photosphere. Supergranulation is a very similar phenomenon. The convective patterns, however, have sizes of 15-40 Mm and lifetimes of up to 33 hours. When integrating granulation and supergranulation perturbations over the entire stellar disk, radial velocity measurements are affected with signatures on the order of  $\text{m s}^{-1}$ .

A major problem for exoplanet searches are radial velocity variations induced by magnetic activity related phenomena. Rotating spots and plages cause characteristic deformations in the line profiles, since they disturb the symmetry between light emitted by the approaching blue shifted limb and light emitted from the preceding red shifted limb. These spurious perturbations produce Doppler shifts that can mimic a planetary signal. Doppler signals are correlated with stellar chromospheric activity. Activity indicators and spectral diagnostics are therefore broadly used to discriminate between real planetary signals and stellar activity.



### **3.7 Radial velocity study of the planetary system GJ 4276**

This publication deals with the discovery of a Neptune-mass planet orbiting the M4.0 dwarf GJ 4276. The study includes the in-depth analysis of radial velocity measurements obtained with the visual channel of CARMENES. GJ 4276 belongs to the CARMENES survey sample of  $\sim 300$  M dwarf stars and was monitored between 2016 and 2018 within Guaranteed Time Observations. It further belongs to one of the 17 CARMENES planet discoveries that were detected in 13 planetary systems (<https://carmenes.caha.es/ext/science/index.html>, accessed: Oct 2019).



## 4 Telluric contamination

The treatment of telluric lines is a critical element of precise radial velocity analyses. Telluric contamination is almost negligible in the blue wavelength range, where most of the state of the art instruments operate (e.g. HARPS). However, at redder wavelengths as well as in the near-infrared range, telluric contamination becomes severe. Figure 4.1 shows the telluric bands within the wavelength range of CARMENES. The major contributing molecular species are H<sub>2</sub>O, O<sub>2</sub>, CO<sub>2</sub>, and CH<sub>4</sub>. In order to increase the scientific value of the CARMENES outcome, a thorough investigation of the contaminated regions is required.

In this section, I outline current telluric corrections techniques, and discuss the studies that investigate the impact of telluric features on precise radial velocity measurements.

### 4.1 Telluric correction techniques

The presence of molecular absorption features due to the Earth's atmosphere in ground-based observations often affects spectroscopic analyses. In order to recover the original telluric-free science spectrum, astronomers have developed sophisticated correction techniques.

A frequently used and effective method is to observe a telluric standard star close in time and similar airmass to the science target (e.g., Vacca et al. 2003). Usually, the choice falls on bright hot O-, B-, or A-type stars as such telluric standards. Because of the high temperatures, their spectra show a clean continuum with only few and weak metal lines. By choosing rapidly rotating standard stars, these intrinsic features can be further smeared out due to rotational broadening, resulting in a spectrum that adequately fits the atmospheric transmission. The division of the target spectrum by the telluric standard spectrum then reveals the telluric corrected spectrum. However, telluric standard stars exhibit strong photospheric hydrogen absorption lines affecting in particular the near-infrared wavelength range, where the Paschen and Brackett lines lie. The telluric correction with such stars makes precise studies in the *I*, *z*, *Y*, or *H* bands or of the hydrogen lines in the target spectrum very challenging (Vacca et al. 2003).

A possible workaround was presented by Maiolino et al. (1996), who focussed on solar-like G-type stars as telluric standards. To account for the star's intrinsic features, they used a high-resolution solar FTS spectrum provided by Livingston & Wallace (1991), which was corrected for telluric absorption using a differential airmass interpolation method. Maiolino et al. (1996) first modified the solar spectrum to match the characteristics of their telluric standard by applying a wavelength shift according to the radial velocity of their standard, correcting for the barycentric Earth radial velocity, applying rotational broadening, and convolving it to the resolution of the observation. With such a stellar template, the target observation was then corrected for telluric contamination as well as for intrinsic features of the standard star. However, the accuracy of the telluric correction strongly depends on the match of a large number of spectral lines between the standard star spectrum and the solar

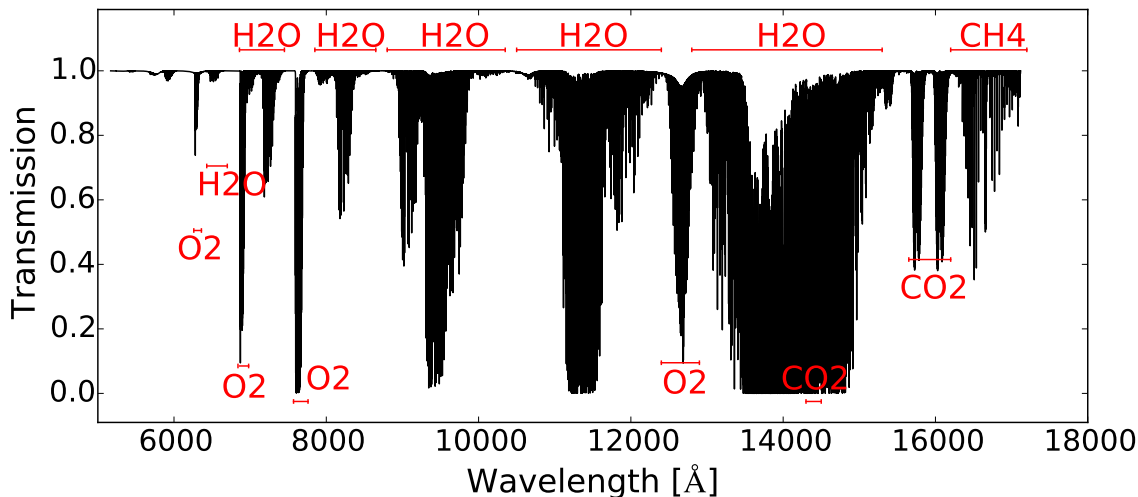


Figure 4.1: Synthetic transmission model of the Earth’s atmosphere computed over the entire wavelength range of CARMENES. The main absorbers are H<sub>2</sub>O, O<sub>2</sub>, CO<sub>2</sub>, and CH<sub>4</sub>.

spectrum. Deviations in the stellar parameters, e.g. in effective temperature and metallicity, introduce artifacts in the corrected spectrum.

The correction with the standard star method is limited. It might be problematic to find suitable standard stars at similar airmass and time as the target observation, in particular reasonably bright G stars. Starlight originating from unequal pointing directions than the science target penetrates through different paths of the atmosphere, so that the atmospheric imprint is different. Another disadvantage is that standard star observations are costly in terms of telescope time, especially for 8 m class telescopes, where observation time is valuable. In the infrared spectral range the integration time of standard stars can be comparable to or even larger than those of the science target.

An alternative approach to standard star observations is the use of synthetic transmission models calculated with radiative transfer codes. Lallement et al. (1993) firstly built a synthetic H<sub>2</sub>O transmission spectrum in the wavelength range of the sodium doublet at 589.5 nm using a molecular data base and a forward-model. Only one year later, Widemann et al. (1994) extended this approach to the near-infrared by using a synthetic atmospheric H<sub>2</sub>O absorption spectrum around 931-948 nm to separate the stellar lines of cool K and M stars from telluric lines in order to identify absorption lines in the star’s spectrum. Although Bailey et al. (2007) demonstrated that residuals of synthetic transmission model fits are on a  $\sim 1\%$  level, such models were not used as a standard method because of poorly accessible radiative transfer codes and incomplete molecular databases. However, the situation changed in the last few years after much effort has been put into the development of the telluric correction with synthetic transmission spectra. Seifahrt et al. (2010) used a line-by-line radiative transfer model (LBLRTM; Clough et al. 2005) incorporating a standard atmosphere and the HITRAN<sup>1</sup> database (Gordon et al. 2011; Rothman et al. 2009) to simulate the transmission and emission of light in the Earth’s atmosphere. In a case study using the CRIRES<sup>2</sup> spectrograph the authors generated theoretical transmission spectra for a wide wavelength range covering H<sub>2</sub>O, CO<sub>2</sub>, CH<sub>4</sub>, N<sub>2</sub>O, O<sub>3</sub>, and CO absorption bands,

<sup>1</sup>High-resolution TRANsmission molecular absorption database

<sup>2</sup>CRyogenic high-resolution InfraRed Echelle Spectrograph

and fitted them to a series of B- and A-type stars observed at various airmasses. With their approach, they reproduced telluric absorption features to  $\sim 2\%$ . This was the beginning of the development of several publicly available codes such as TelFit (Gullikson et al. 2014), TAPAS<sup>3</sup> (Bertaux et al. 2014), tellrem (Rudolf et al. 2016), and molecfit (Kausch et al. 2015; Smette et al. 2015).

A novel empirical approach to telluric absorption was presented by Artigau et al. (2014). They compiled a library of archival telluric standard star spectra observed at a large variety of airmasses and atmospheric conditions and carried out a principal component analysis to identify independently varying absorbers. A linear combination of these absorption patterns was then used to create a synthetic transmission spectrum that was subtracted from HARPS observations.

A pure data-driven analysis approach was recently proposed by (Bedell et al. 2019). Based on machine-learning algorithms they developed the freely available wobble code, which incorporates a linear model to simultaneously infer the stellar spectra, the telluric spectra, and precise radial velocities of a time series of high-resolution, high S/N spectra. Without the need of external information about the stellar source or the atmospheric conditions during the time of the observations, their method is intended to be a post-processing procedure rather than a real-time reduction pipeline.

## 4.2 Impact on Radial velocity

The state of the art Doppler precision reached by current instruments is on the order of  $1\text{ m s}^{-1}$  and only falls below that level when selecting very stable stars and adopting an observational strategy that minimizes stellar noise (see for instance Pepe et al. 2011). To achieve higher precision, the proper treatment of telluric contamination is one of the key data analysis challenges (Fischer et al. 2016). The vast majority of exoplanets detected with the radial velocity method are based on measurements made with spectrographs that operate in the visible wavelength range. For those instruments telluric contamination was not considered problematic because regions containing telluric lines are mostly avoided. For instance, Cunha et al. (2014) reported that 3 of the 72 spectral orders that include deep telluric absorption lines are neglected when computing the radial velocity. When a spectrum with imprinted telluric features is cross-correlated with a binary mask a spurious signal is produced by the apparent correlation between the line in the mask and the telluric line Pepe et al. (2002). This spurious signal creates an asymmetry in the CCF and may introduces an additional uncertainty in the radial velocity measurement. Therefore, cross-correlation masks are usually cleaned from telluric features by removing all stellar lines that lie close to telluric lines. However, very shallow and barely visible telluric lines with a depth of  $< 1\%$  still affect wavelength ranges in the visible and almost the entire near-infrared range. As the S/N of the spectra increases and the calibration improves, these micro-tellurics increase the noise and cause a spurious periodic signal of one year.

The CARMENES radial velocity pipeline incorporates the masking strategy. At the red end of the visual spectral range three telluric contaminated orders and six of the 28 orders in the near-infrared channel are excluded from the radial velocity determination. For orders that are partly affected by telluric contamination, the radial velocity algorithm SERVAL uses a telluric mask that flags telluric features that are deeper than  $5\%$  (Zechmeister et al.

<sup>3</sup> Transmissions Atmosphériques Personnalisées pour l'ASTronomie

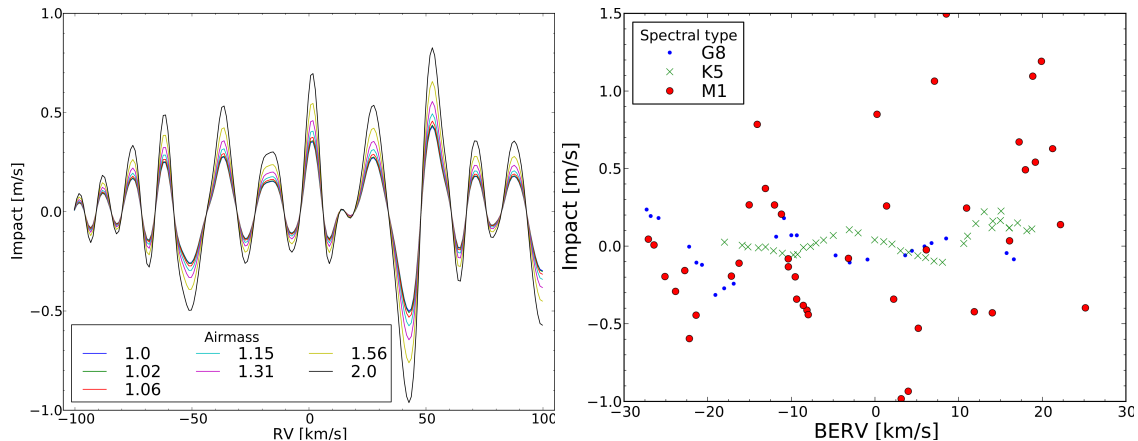


Figure 4.2: *Left panel:* Atmospheric impact on radial velocity determination for a set of solar spectra shifted from  $+100\text{ km s}^{-1}$  to  $-100\text{ km s}^{-1}$  and superimposed by synthetic transmission spectra with airmasses between 1 and 2. *Right panel:* Atmospheric impact on radial velocities for stars of different spectral type as a function of barycentric Earth radial velocity. From: Cunha et al. (2014).

2018), which means that telluric features with depths of less than 5% remain in the stellar spectrum. All features that appear in a spectrum and do not belong to the star can introduce spurious radial velocity variations.

The impact of micro-telluric lines on precise radial velocities was first investigated by Cunha et al. (2014), who focussed on micro-tellurics with depths  $< 1 - 3\%$ . They used a set of synthetic solar spectra with radial velocity shifts in the range of  $\pm 100\text{ km s}^{-1}$  in  $1\text{ km s}^{-1}$  steps and superimposed them with synthetic transmission spectra with different airmasses. The radial velocities of the simulated spectra were then derived with the cross-correlation method. The impact of the atmosphere was calculated as the difference between the radial velocity of the original spectra without the atmosphere and the modified spectra with the atmosphere. Their results are shown in the left panel of Fig 4.2. Not surprisingly, the impact depends on the airmass and the radial velocity of the star. Micro-tellurics that were not captured by the cross-correlation mask can introduce radial velocity variations of almost  $1\text{ m s}^{-1}$ . Even for observations at the zenith the maximum impact can still reach a value of  $0.5\text{ m s}^{-1}$ . Cunha et al. (2014) further corrected HARPS spectral series of stars with spectral types G, K, and M from telluric lines using synthetic transmission spectra and calculated the impact of the atmosphere on the radial velocity. The impact is shown as a function of the barycentric Earth radial velocity in the right panel of Fig. 4.2. Very similar to the simulations, the impact on the radial velocity measurements depends on the radial velocity shift of the star. However, in this case the stellar radial velocity shift is caused by the movement of the Earth around the Sun. Although the impact is on a level of  $10 - 20\text{ cm s}^{-1}$  for G-type stars, it increases to more than  $1\text{ m s}^{-1}$  for M dwarfs.

The impact of telluric subtraction on radial velocity measurements was also verified by Artigau et al. (2014). In their study, they applied their telluric subtraction method based on a principal component analysis (PCA) to archival HARPS spectra of  $\tau$  Ceti (G8 V) and GJ 436 (M3.5 V) and corrected the wavelength range at around 630 nm affected by telluric absorption. With a combination of PCA-based telluric correction and masking they reduced the overall radial velocity rms by  $\sim 0.2\text{ m s}^{-1}$ .

## 4.3 Telluric correction in CARMENES

When the CARMENES survey began, me and my collaborators within the CARMENES consortium discussed different approaches on how to mitigate telluric contamination and how to improve the radial velocity precision of CARMENES. We decided that modeling the Earth's transmission with current software packages might be a promising approach. However, fitting synthetic transmission models to star types like M dwarfs, that exhibit numerous intrinsic features, is challenging or even impossible. Therefore, I developed the template division telluric modeling (TDTM) technique that is presented in Sect. 5 in great detail.





# 5 Publications

## 5.1 Overview

In this chapter I reproduce two publications that are the main part of this cumulative thesis. Both works primarily deal with the analysis of high-resolution visible and near-infrared CARMENES spectra and the radial velocities that were derived from these spectra. The spectroscopic data were taken as part of the CARMENES GTO surveys by members of the CARMENES collaboration. According to the regulations of the University of Hamburg, I will give an overview of my contributions in the next section.

### 5.1.1 My contributions

I am the leading author on both publications. According to the “CARMENES Rules for Science Exploitation” each scientific publication presenting results from the CARMENES survey has to be jointly published by members of the consortium. The author list must include CARMENES team members who significantly contributed to the publication as well as members who contribute to project preparation, implementation, and exploitation. Each CARMENES institute must also be represented by at least one member. The author list consist of three groups of authors:

- Group 1: Lead author and those who carried out significant work.
- Group 2:  
Names of the principal investigators (PIs): A. Quirrenbach, P. J. Amado.  
Names of the project scientists (PSs): I. Ribas, A. Reiners.  
Name of the instrument astronomer (IA): J. A. Caballero.
- Group 3: Less significant contributors as well as representatives, if not listed in group 1 and 2, given in alphabetical order.

Prior to submission, the publications were circulated between the co-authors. At this stage, all co-authors had the chance to proofread the publication and to send comments that were mostly implemented.

#### Publication #1

The implementation of the TDTM technique, the analysis, and writing was performed by myself. Stefan Czesla helped with proofread and extensive discussions. Adrian Kaminski contributed to the analysis of the line profile (Appendix A). The SERVAL pipeline that is used to create the template and to compute radial velocities was developed and implemented by Mathias Zechmeister (Zechmeister et al. 2018).

### **Publication #2**

As in the previous publication, the analysis and writing was done by myself. The photometric data sets obtained with the facilities from the Sierra Nevada Observatory and the Las Cumbres Observatory were provided by members of the CARMENES consortium. The software that was used to fit the Keplerian models to the radial velocities was written by Stefan Czesla. He also contributed to proofreading and discussions. Stefan Dreizler contributed with the orbital evolution of the eccentric single-planet solution.

#### **5.1.2 Publication status**

The first paper has been submitted to *Astronomy & Astrophysics* on 16th September 2019. The second paper has been published in *Astronomy & Astrophysics* (Nagel et al. 2019).

## **5.2 The template division telluric modeling technique and its application to optical and near-infrared radial velocities**

**Authors:** E. Nagel, S. Czesla, A. Kaminski, M. Zechmeister, L. Tal-Or, J. H. M. M. Schmitt, I. Ribas, A. Reiners, A. Quirrenbach, P. J. Amado, J. A. Caballero, J. M. Alacid, F. F. Bauer, V. J. S. Béjar, M. Cortés-Contreras, S. Dreizler, A. Hatzes, S. V. Jeffers, M. Kürster, M. Lafarga, D. Montes, J. C. Morales, and S. Pedraz

**Submitted to Astronomy & Astrophysics**

# The CARMENES search for exoplanets around M dwarfs

## The template division telluric modeling technique and its application to optical and near-infrared radial velocities

E. Nagel<sup>1</sup>, S. Czesla<sup>1</sup>, A. Kaminski<sup>2</sup>, M. Zechmeister<sup>3</sup>, L. Tal-Or<sup>3,4</sup>, J. H. M. M. Schmitt<sup>1</sup>, I. Ribas<sup>5,6</sup>, A. Reiners<sup>3</sup>, A. Quirrenbach<sup>2</sup>, P. J. Amado<sup>7</sup>, J. A. Caballero<sup>8</sup>, J. M. Alacid<sup>8</sup>, F. F. Bauer<sup>7</sup>, V. J. S. Béjar<sup>9</sup>, M. Cortés-Contreras<sup>8</sup>, S. Dreizler<sup>3</sup>, A. Hatzes<sup>10</sup>, S. V. Jeffers<sup>3</sup>, M. Kürster<sup>11</sup>, M. Lafarga<sup>5,6</sup>, D. Montes<sup>12</sup>, J. C. Morales<sup>5,6</sup>, and S. Pedraz<sup>13</sup>

<sup>1</sup> Hamburger Sternwarte, Gojenbergsweg 112, 21029 Hamburg, Germany  
e-mail: [evangelos.nagel@hs.uni-hamburg.de](mailto:evangelos.nagel@hs.uni-hamburg.de)

<sup>2</sup> Landessternwarte, Zentrum für Astronomie der Universität Heidelberg, Königstuhl 12, 69117 Heidelberg, Germany

<sup>3</sup> Universität Göttingen, Institut für Astrophysik, Friedrich-Hund-Platz 1, 37077 Göttingen, Germany

<sup>4</sup> Department of Geophysics, Raymond and Beverly Sackler Faculty of Exact Sciences, Tel Aviv University, Tel Aviv 6997801, Israel

<sup>5</sup> Institut de Ciències de l'Espai (ICE, CSIC), Campus UAB, C/ de Can Magrans s/n, 08193 Cerdanyola del Vallès, Spain

<sup>6</sup> Institut d'Estudis Espacials de Catalunya (IEEC), C/ Gran Capità 2-4, 08034 Barcelona, Spain

<sup>7</sup> Instituto de Astrofísica de Andalucía (IAA-CSIC), Glorieta de la Astronomía s/n, 18008 Granada, Spain

<sup>8</sup> Centro de Astrobiología (CSIC-INTA), ESAC, Camino Bajo del Castillo s/n, 28692 Villanueva de la Cañada, Madrid, Spain

<sup>9</sup> Instituto de Astrofísica de Canarias, Vía Láctea s/n, 38205 La Laguna, Tenerife, Spain

<sup>10</sup> Thüringer Landessternwarte Tautenburg, Sternwarte 5, 07778 Tautenburg, Germany

<sup>11</sup> Max-Planck-Institut für Astronomie, Königstuhl 17, 69117 Heidelberg, Germany

<sup>12</sup> Departamento de Física de la Tierra y Astrofísica and IPARCOS-UCM (Intituto de Física de Partículas y del Cosmos de la UCM), Facultad de Ciencias Físicas, Universidad Complutense de Madrid, E-28040, Madrid, Spain

<sup>13</sup> Centro Astronómico Hispano-Alemán (CSIC-MPG), Observatorio Astronómico de Calar Alto, Sierra de los Filabres, 04550 Górgal, Almería, Spain

Received date / Accepted date

### ABSTRACT

Telluric contamination in ground-based optical and infrared spectroscopy is an important limiting factor in achieving maximum radial velocity (RV) precision with the aim of detecting Earth-like planets orbiting low-mass stars. Here we present the template division telluric modeling (TDTM) technique, a method to accurately remove telluric absorption lines in stars that exhibit numerous intrinsic features. Based on the Earth's barycentric motion through the year, our approach is suited to disentangle telluric and stellar spectral components. By fitting a synthetic transmission model, telluric-free spectra are subsequently derived. We demonstrate the performance of the TDTM technique in correcting telluric contamination using high-resolution optical and near-infrared spectral time series of the rapidly rotating A0-type star 109 Vir and the feature-rich M dwarfs GJ 273 (Luyten's star, M3.5 V) and GJ 1012 (M4.0 V) obtained with the CARMENES spectrograph. As GJ 1012 has been shown to show particularly low RV variability, we used its spectral time series to study the impact of our TDTM correction on the achievable RV precision. While the RV precision obtained in the optical arm is comparable to that produced by conservative masking of telluric features, we achieve a highly significant improvement in the near-infrared range. For GJ 1012 we find that the RV scatter decreases from  $9.5 \text{ m s}^{-1}$  to  $5.7 \text{ m s}^{-1}$  after applying the TDTM approach. Although the decrease in RV scatter is expectedly driven by the most heavily contaminated echelle orders close to strong telluric water bands, improvement is demonstrated over the entire wavelength range covered by the near-infrared channel of CARMENES. Our study emphasizes that the proper treatment of telluric lines in infrared high-precision RV studies is pivotal to push the capacity of near-infrared spectrographs to measure low-amplitude RV signals, and we demonstrate the power of our TDTM technique to achieve that.

**Key words.** atmospheric effects – instrumentation: spectrographs – methods: data analysis, observational – stars: low-mass – techniques: spectroscopic

## 1. Introduction

Ground-based spectroscopic observations at optical and near-infrared wavelengths are affected by absorption and emission features produced by the Earth's atmosphere. Rotational-vibrational transitions of molecules such as water (H<sub>2</sub>O), oxygen (O<sub>2</sub>), carbon dioxide (CO<sub>2</sub>), and methane (CH<sub>4</sub>) produce numerous absorption lines and broad absorption bands. Individual lines

vary in strength from shallow so-called micro-tellurics to strong lines with completely opaque line cores. These telluric lines are a common nuisance in ground-based spectroscopy.

The atmospheric conditions at the time of observation determine the telluric contribution to a stellar spectrum observed from the ground. The observed strength of the telluric lines depends on the location, in particular the elevation, of the observatory and the airmass of the target. Furthermore, telluric absorption lines

are Doppler shifted and broadened due to turbulent wind motions along the line of sight (e.g. Caccin et al. 1985). The atmospheric temperature and partial-pressure structure have a direct impact on the line profiles. The situation is further complicated by the temporal variability in temperature, pressure, and chemical composition of the Earth’s atmosphere on seasonal, daily, and hourly time scales, which is particularly pronounced for the atmospheric water vapor content (Smette et al. 2015).

The detection of Earth-like rocky planets orbiting in the habitable zones of their host stars, requires very precise radial velocity (RV) measurements. In this context, the correction of telluric features has come into focus as one of the main contributors to the RV error budget (Halverson et al. 2016). Cool, low-mass M dwarfs are particularly promising targets for detecting rocky habitable-zone planets because of their relatively short orbital periods of around 20 d and the favorable planet-to-star mass ratios. As M dwarfs are intrinsically faint in the visible wavelength range and emit the bulk of their energy at  $\sim 1 \mu\text{m}$ , a new generation of high-resolution spectrographs, such as CARMENES (Quirrenbach et al. 2018), NIRPS (Wildi et al. 2017), SPIRou (Donati et al. 2018), HPF (Mahadevan et al. 2014), and IRD (Kotani et al. 2018), have been designed and built to exploit the near-infrared wavelength range for RV planet searches. In this range, however, also telluric contamination is particularly severe. Reiners et al. (2018) showed that the highest RV precision for early and mid- M dwarfs can be reached in the wavelength range 700–900 nm. Wavelength ranges contaminated by telluric absorption were neglected in their analysis. Correction of this and other spectral regions that are heavily contaminated by O<sub>2</sub> and H<sub>2</sub>O could significantly increase the RV precision in M dwarf observations.

A simplified approach to alleviate the impact of telluric lines on the RV measurement is to mask all telluric lines above a certain strength threshold prior to the RV computation. Indeed, this technique has been applied in many data-analysis pipelines devoted to extracting RVs from optical spectra, with satisfactory results (e.g., Anglada-Escudé & Butler 2012; Zechmeister et al. 2018). In the infrared, however, the ubiquity of telluric lines leads to extended masks. As a result, neglecting masked chunks of the stellar spectrum significantly limits our ability to study the infrared spectra and lowers the RV precision. Therefore, alternative techniques with better performance are called for.

To date, several elaborated approaches have been developed to correct for telluric lines, which can roughly be subdivided into empirical, data-driven, and forward-modeling approaches. A widely-used empirical technique is telluric division. Here telluric standard stars (TSSs) – usually rapidly rotating B- to A-type stars – are observed along with the science target observation, preferably similar in time, airmass, and direction as the science target. However, some compromises have to be made regarding these parameters. The drawbacks of the telluric division method have been extensively discussed, e.g., by Vacca et al. (2003), Bailey et al. (2007), Seifahrt et al. (2010), Gullikson et al. (2014), and Smette et al. (2015). Large RV surveys as those conducted by the HARPS and CARMENES collaborations refrain from frequent TSS observations because of the tremendous amount of additional observing time needed.

An empirical approach, avoiding frequent and repeated TSS observations, was presented by Artigau et al. (2014). These authors created a library of TSS spectra, observed on a dense grid of airmasses and water columns. By carrying out a principal component analysis, they identified independently varying spectral absorption patterns. Thus, telluric spectra were synthesized by using linear combinations of individual absorbances, which

Artigau et al. (2014) subsequently removed from HARPS measurements.

A data-driven technique involving machine-learning algorithms was presented by Bedell et al. (2019). Their wobble algorithm incorporates a model to simultaneously derive the stellar spectra, telluric spectra, and RVs from spectral time series without relying on external information on either the stellar or the telluric transmission spectrum.

While purely data-driven techniques are highly flexible, copious information on the atmosphere of the Earth and its spectrum is of course available. Synthetic transmission models of the spectrum of the Earth’s atmosphere take advantage of this. They can be generated by radiative transfer codes (for an overview see Seifahrt et al. 2010) in combination with precise molecular line databases, and have become widely used (e.g., Bailey et al. 2007; Seifahrt et al. 2010; Lockwood et al. 2014; Husser & Ulbrich 2014; Gullikson et al. 2014; Rudolf et al. 2016).

The software package *molecfit*<sup>1</sup>, developed by Smette et al. (2015) and Kausch et al. (2015), implements a synthetic telluric transmission model and allows to correct observed spectra for telluric contamination. To that end, *molecfit* incorporates the line-by-line radiative transfer code LBLRTM (Clough et al. 2005) and the HITRAN molecular line list (Rothman et al. 2009). To synthesize a telluric spectrum, *molecfit* requires a number of parameters such as a model of the instrumental line spread function, an atmospheric profile describing the meteorological conditions during the observation, and the column density of the molecular species. In turn, the observed spectrum, which contains the telluric transmission spectrum, can be used to find best-fit values for these parameters. *molecfit* does not consider the actual stellar spectrum, which occurs as a contaminant of the telluric spectrum in this context. Therefore, usually only a suitable subrange of the observed spectrum is used in the fit, which ideally contains moderately saturated telluric lines with a well-defined continuum. Based on the resulting atmospheric parameters, the telluric spectrum in the remaining range can then be inferred. While this approach works well in many cases, it becomes problematic in objects with ubiquitous intrinsic features such as M dwarfs, where the fitting becomes inaccurate because of numerous blends between stellar and telluric lines.

To address this problem, we present the template division telluric modeling (TDTM) technique. The heart of TDTM is the disentanglement of sections of the telluric and stellar spectrum by taking advantage of the relative shift between stellar and telluric lines caused by the Earth’s barycentric motion. We then use *molecfit* to fit a synthetic transmission model to the extracted telluric spectrum and apply these results to correct for telluric absorption in the entire science spectrum. While the TDTM technique works independently of stellar spectral type, it is only applicable when spectroscopic time series sampling a range of barycentric velocity shifts are available.

Our paper is structured as follows. In Sect. 2 we describe the spectroscopic observations. The TDTM technique and the data preparation are presented in Sect. 3, and our findings are discussed in Sect. 4. Finally, we summarize our results in Sect. 5.

**Table 1.** Equatorial coordinates (J2000),  $G$  and  $J$  magnitudes, and number of used VIS and NIR spectra.

| Name    | $\alpha$    | $\delta$     | $G^a$ [mag]          | $J^b$ [mag]       | $N_{\text{VIS}}$ | $N_{\text{NIR}}$ |
|---------|-------------|--------------|----------------------|-------------------|------------------|------------------|
| 109 Vir | 14 46 14.93 | +01 53 34.39 | $3.6103 \pm 0.0043$  | $3.683 \pm 0.244$ | 163              | 154              |
| GJ 273  | 07 27 24.50 | +05 13 32.83 | $8.5945 \pm 0.0003$  | $5.714 \pm 0.032$ | 191              | 180              |
| GJ 1012 | 00 28 39.47 | -06 39 49.18 | $10.8947 \pm 0.0007$ | $8.038 \pm 0.020$ | 22               | 13               |

Notes. <sup>(a)</sup> Gaia Collaboration et al. (2018); <sup>(b)</sup> Cutri et al. (2003)

## 2. Observations and data reduction

The spectra used in this work were taken within the context of the CARMENES<sup>2</sup> survey. Constructed by eleven German and Spanish institutions, CARMENES consists of a pair of cross-dispersed fiber-fed échelle spectrographs, mounted on the 3.5 m telescope of the Calar Alto Observatory in Spain (Quirrenbach et al. 2018). CARMENES monitors the RVs of more than 300 M dwarfs to detect low-mass planets in their habitable zones (Reiners et al. 2018).

The instrument has two channels. The visual channel (VIS) provides wavelength coverage between 5 200 Å and 9 600 Å with a resolution of  $R = 94\,600$ , and the near-infrared channel (NIR) has a resolving power of  $R = 80\,400$  and covers the spectral range from 9 600 Å to 17 100 Å. Both instruments are enclosed in vacuum vessels in the coudé room to ensure long-term stability. The data reduction was carried out using the standard CARMENES reduction pipeline CARACAL<sup>3</sup> (Zechmeister et al. 2014; Caballero et al. 2016).

To demonstrate the performance and to evaluate the accuracy of the TDTM technique, we use observations of 109 Vir (HD 130109), an A0 V dwarf with  $v \sin i = 285 \text{ km s}^{-1}$  (Royer et al. 2007), which is a regularly observed TSS in the CARMENES survey. In total, the time series consists of 163 VIS and 154 NIR observations taken between January 2017 and March 2019. In addition, we selected 191 VIS and 180 NIR observations of the bright M3.5 V dwarf GJ 273 (Luyten’s star) obtained between January 2016 and March 2019. GJ 273 serves as a typical representative of an object with a feature-rich spectrum. We demonstrate the improvement on the root-mean-square (rms) velocity dispersion achieved by the TDTM technique in the optical and near-infrared wavelength range using a sample of 22 VIS and 13 NIR spectra of the M4.0 V dwarf GJ 1012. This star was selected because it is a so-called RV-quiet star, characterized by weak RV variability with a standard deviation of only  $2.2 \text{ m s}^{-1}$  in the optical spectral range (Trifonov et al. 2018; Tal-Or et al. 2019). In Table 1 we provide information on the coordinates,  $G$  and  $J$  magnitudes, and on the number of used VIS and NIR spectra.

A typical signal-to-noise ratio (S/N) for CARMENES survey observations is 150 in the  $J$  band (Reiners et al. 2018), which translates into a median exposure time of 380 s for GJ 273 and 1800 s for GJ 1012. Since 109 Vir is a bright target ( $J = 3.70$  mag), the typical exposure time of one minute already provides higher S/N.

<sup>1</sup> <http://www.eso.org/sci/software/pipelines/skytools/molecfit>

<sup>2</sup> Calar Alto high-Resolution search for M dwarfs with Exoearths with Near-infrared and optical Echelle Spectrographs.

<sup>3</sup> CARMENES Reduction And CALibration

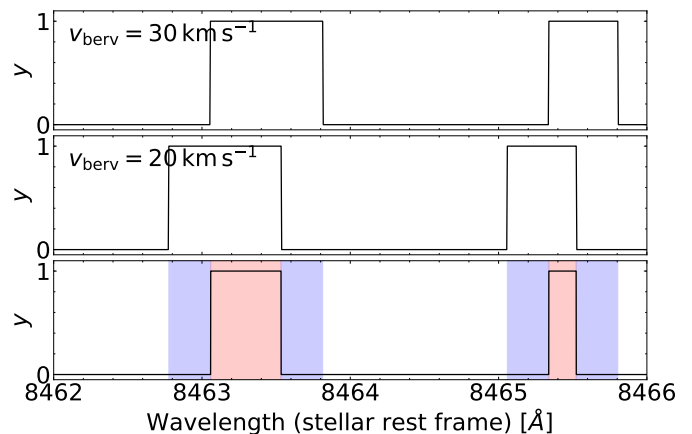


**Fig. 1.** Upper and middle panels: Small section of the telluric binary mask for two observations after the correction of the Earth’s barycentric motion. Wavelength ranges with  $y = 1$  are masked as tellurics. Lower panel: Resulting mask of the template. Red shaded wavelength ranges correspond to template knots with  $m_k = 0$  and contribute to the total masked template fraction  $\gamma$ . The blue shaded wavelength ranges are used for telluric modeling and contribute to  $\gamma'$ .

## 3. Correction method

Fitting telluric transmission models to observed M dwarf spectra is challenging because the stellar spectrum consists of numerous atomic and molecular lines without a true continuum. The fundamental idea behind the TDTM approach is to construct a high signal-to-noise template of the stellar spectrum from a spectral time series, which can be used subsequently to eliminate the stellar contribution and to model the residual telluric spectrum.

### 3.1. Template construction

We use the SERVAL<sup>4</sup> code (Zechmeister et al. 2018) to compute the stellar template spectrum based on a time series of input spectra. Following the nomenclature of Zechmeister et al. (2018), we index the set of spectra by  $n = 1, \dots, N$ , and each spectrum is composed of flux density measurements  $f_{n,i}$  at pixel  $i$  with uncertainties  $\epsilon_{n,i}$  and calibrated wavelengths  $\lambda_{n,i}$ . We further write the observed spectrum in the form

$$f(\lambda_{n,i}) = [s(\lambda_{n,i}) \cdot t(\lambda_{n,i})] \otimes L(\lambda_i), \quad (1)$$

where  $s(\lambda_{n,i})$  denotes the intrinsic stellar spectrum,  $t(\lambda_{n,i})$  the telluric absorption spectrum at the time of observation,  $L(\lambda_i)$  the line spread function, and  $\otimes$  the convolution operator.

In each observation, a stellar spectrum with a priori unknown RV shift and a telluric spectrum with variable properties, but

<sup>4</sup> SpEctrum Radial Velocity AnaLyser, <https://github.com/mzechmeister/serval>

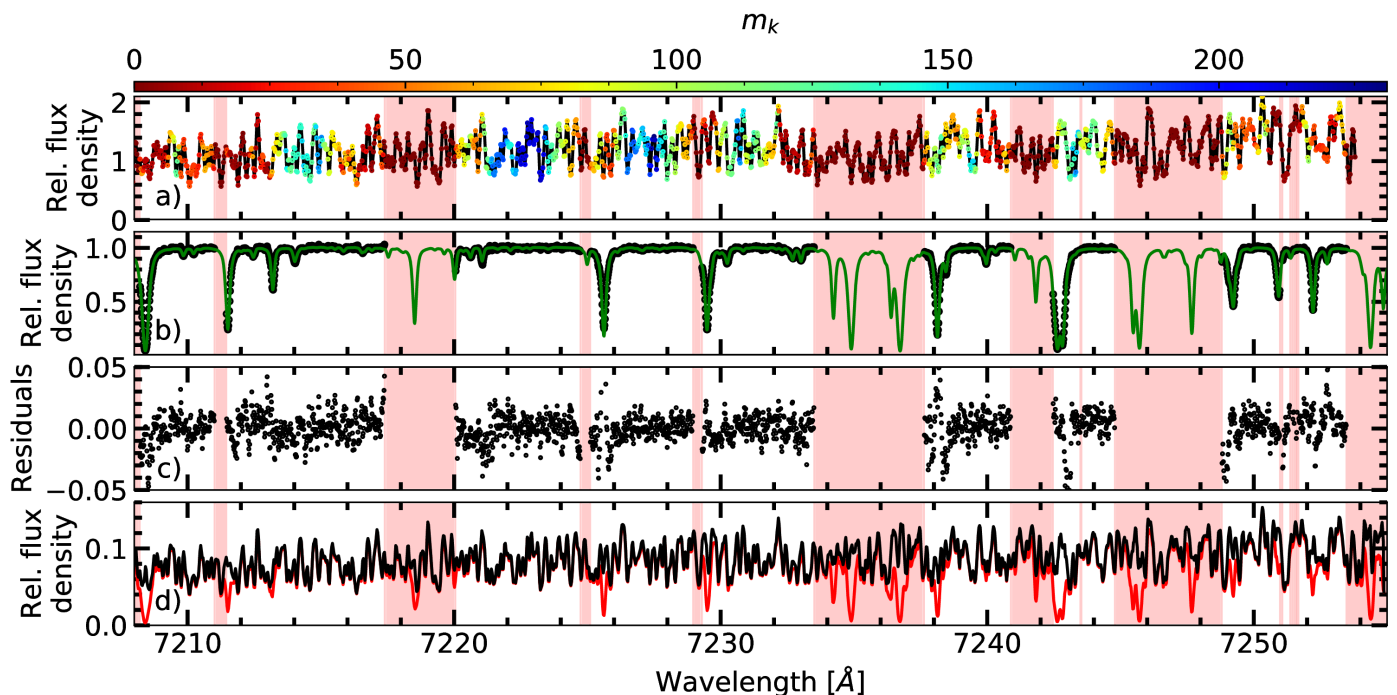


**Fig. 2.** *Panel a:* Segment of the optical template spectrum of GJ 273. Color-coded is the number  $m_k$  of exposure pixels that contribute to each template knot. The red shaded wavelength ranges mark knots with  $m_k = 0$ . *Panel b:* One residual telluric spectrum  $f_{n,i}/s'(\lambda_i)$  (black dots) after the division of the science spectrum by the template, and best-fit telluric model ( $T(\lambda_{n,i})$ , green line) derived with `molectfit`. Red shaded wavelength ranges are excluded from the transmission model fit. *Panel c:* Absolute residuals  $f_{n,i}/s'(\lambda_{n,i}) - T(\lambda_{n,i})$  of the fit. *Panel d:* CARMENES spectrum before ( $f_{n,i}$ , red line) and after ( $f_{n,i}/T(\lambda_{n,i})$ ) correction with the transmission model derived with `molectfit` (black line).

fixed in the rest frame of the Earth, are superimposed. The ultimate goal of SERVAL is to derive precise measurements of the stellar RV. To that end, a preferably accurate and complete template of the stellar spectrum is required. This template is constructed by SERVAL from the spectral time series, following an iterative and sequential forward modeling approach.

Template completeness is improved by taking advantage of the relative RV shift of the stellar and telluric spectra induced by the Earth’s barycentric motion, which can uncover sections of the stellar spectrum in some observations that may be affected by telluric lines in others with less favorable relative RV shift. To identify such sections, SERVAL uses a binary mask  $m(\lambda_{n,i})$ , flagging spectral pixels affected by known atmospheric absorption features that are typically deeper than 1% (see Sect. 3.2). Additionally, SERVAL employs a bad-pixel map, which flags saturated pixels, outliers, pixels providing unphysical (negative) flux densities, and pixels affected by sky emission. Template S/N is improved by coadding the individual spectra after an appropriate RV shift. During this process, the spectra are transformed to the stellar rest frame, i.e. corrected for barycentric and stellar RVs. SERVAL also accounts for secular acceleration, a change in the stellar radial velocity due to the high proper motion of close-by stars (Kürster et al. 2003; Zechmeister et al. 2009).

As a starting point for RV and template calculation, SERVAL calculates preliminary RVs using the highest S/N spectrum of the CARMENES spectral time series as a template. These are subsequently used to improve the stellar template spectrum by coadding the individual spectra and obtain higher precision RVs. This process is repeated until convergence is achieved. All masked pixels are excluded and telluric affected heavily down-weighted in the process of coadding to isolate the stellar spectrum in the template.

The process of improving the template completeness by taking advantage of the relative shift of the mask is demonstrated in Fig. 1. The upper and middle panels show a segment of the telluric mask position of two observations after the correction for the Earth’s barycentric motion. The lower panel shows the resulting mask of the template, assuming that the intrinsic RV shift of the stellar spectrum remained small. In the blue shaded regions, the stellar spectrum is seen in one of the observations, and only the red shaded ranges remain hidden. This results in an improvement of the template wavelength coverage.

Shifting the spectra to the same reference wavelength results in a wavelength sampling that differs for data taken at different nights. SERVAL avoids interpolating the spectra on a new discrete wavelength grid. Instead, a uniform cubic B-spline regression with knots  $k$  on a regular logarithmic wavelength  $\ln \lambda_k$  grid is carried out. In essence, the template knots specify the wavelength grid of the template. Typically, the number of template knots is comparable to the number of pixels per spectral order. In the following,  $s'_k(\lambda_k)$  refers to the stellar template flux density. As an example, a section of the template of GJ 273 is shown in Fig. 2a.

As a crucial quantity for the TDTM approach, we define  $m_k$  as the number of unflagged pixels that contribute to a knot.  $m_k$  is stored for each template knot. The link between  $m_k$  and the mask can be inferred from the lower panel of Fig. 1. In this specific example with only two observations,  $m_k = 0$  for template knots falling into the red marked wavelength range,  $m_k = 1$  for knots within the blue wavelength range, and  $m_k = 2$  for the remaining part of the of the spectrum.

Therefore, given one particular template knot  $k$ , three situations are possible: (1) all pixels contributing to this knot contain spectral information (i.e., are not masked), (2) all pixels are

masked, (3) some pixels contain spectral information, while the remaining pixels are masked. The quantity  $m_k$  is maximized in case (1), decreases for knots partly affected by tellurics in case (3), and takes a value of  $m_k = 0$  for pixels subject to case (2). For sampling reasons, spectra can contribute more than one pixel to a template knot, so that  $m_k$  can exceed the number  $N$  of observations. This is demonstrated in Fig. 2a, where a few template knots have  $m_k \gtrsim 200$ , although the number of observations is  $N_{\text{VIS}} = 191$ . The red shaded areas show wavelength ranges for which  $m_k$  is zero, i.e., the stellar spectrum could not be recovered.

As the total masked template fraction  $\gamma$  we define the fraction of masked ranges ( $m_k = 0$ ) compared to the entire wavelength range of the spectrum. As a result, the template completeness corresponds to  $1 - \gamma$  and will depend on barycentric RV of the observer. The wavelength ranges of the stellar spectrum characterized by overlapping masked and non-masked regions, indicated by the blue shaded areas in Fig. 1 and recovered in the process, are now additionally available for RV calculation and telluric modeling. We denote the total fraction of these ranges compared to the entire wavelength range of the spectrum by  $\gamma'$ .

### 3.2. Mask construction

The telluric mask is an essential ingredient of the TDTM technique. As telluric features are ubiquitous, mask construction needs to balance strictness and achievable template completeness. While a restrictive mask, covering all relevant telluric features, is crucial to create a useful stellar template, an overly strict mask, declaring extended chunks of the spectrum unusable, jeopardizes the derivation of a template with any practical value.

To construct masks, we computed a synthetic telluric transmission model including H<sub>2</sub>O, O<sub>2</sub>, CO<sub>2</sub>, and CH<sub>4</sub> using `molecfit`. As input parameters we used the median observational and atmospheric parameters of the GJ 273 data set, and adopted the values from the standard atmosphere profile for the column densities of the atmospheric constituents. In the resulting transmission model, we normalized wavelength ranges affected by molecular continuum absorption. Finally, we computed a binary mask by flagging all model features deeper than a specified threshold. In our analysis, we found that a threshold of 1% provides a reasonable compromise between capturing the vast majority of telluric features and removing critical amounts of usable spectrum.

### 3.3. Telluric spectrum extraction

To extract the telluric transmission spectrum, we need to remove the stellar contribution from the individual observations. Therefore, we appropriately shifted the template spectrum and followed Vacca et al. (2003) in approximating Eq. (1)<sup>5</sup> by

$$f(\lambda_{n,i}) \approx [s(\lambda_{n,i}) \otimes L(\lambda_i)] \cdot [t(\lambda_{n,i}) \otimes L(\lambda_i)]. \quad (2)$$

Substituting the convolved intrinsic stellar flux density  $s(\lambda_{n,i}) \otimes L(\lambda_i)$  by the template  $s'(\lambda_i)$  we obtain

$$f(\lambda_{n,i}) \approx s'(\lambda_i) \cdot [t(\lambda_{n,i}) \otimes L(\lambda_i)]. \quad (3)$$

Dividing the observed spectra by the appropriately shifted template, we derive a residual spectrum that is essentially free of

**Table 2.** Molecfit fitting ranges used to calibrate the model for CARMENES VIS and NIR spectra.

| Channel | $\Delta\lambda$ [Å] | Main absorber                      |
|---------|---------------------|------------------------------------|
| VIS     | 6270 – 6324         | O <sub>2</sub>                     |
| VIS     | 6913 – 7070         | O <sub>2</sub> , H <sub>2</sub> O  |
| VIS     | 7148 – 7415         | H <sub>2</sub> O                   |
| VIS     | 7676 – 7714         | O <sub>2</sub>                     |
| VIS     | 7850 – 8425         | H <sub>2</sub> O                   |
| VIS     | 8890 – 9270         | H <sub>2</sub> O                   |
| NIR     | 9750 – 10 350       | H <sub>2</sub> O                   |
| NIR     | 10 600 – 11 000     | H <sub>2</sub> O                   |
| NIR     | 11 600 – 12 400     | H <sub>2</sub> O                   |
| NIR     | 12 400 – 13 100     | O <sub>2</sub>                     |
| NIR     | 15 110 – 15 400     | H <sub>2</sub> O                   |
| NIR     | 15 600 – 15 800     | CO <sub>2</sub>                    |
| NIR     | 15 900 – 16 200     | CO <sub>2</sub>                    |
| NIR     | 16 350 – 16 660     | CH <sub>4</sub>                    |
| NIR     | 16 850 – 17 100     | CH <sub>4</sub> , H <sub>2</sub> O |

stellar features

$$\frac{f(\lambda_{n,i})}{s'(\lambda_i)} \approx t(\lambda_{n,i}) \otimes L(\lambda_i). \quad (4)$$

As the uncertainty of the template is typically negligible compared to that of the individual observations as  $m_k \gg 1$ , we do not propagate the template uncertainty and use the uncertainty of the observed spectra in the modeling of the individual residual spectra.

The residual telluric transmission spectrum of GJ 273 is shown in Fig. 2b. Again, the red bands represent template knots for which the residual spectrum could not be constrained. Consequently, these sections are not used to model the telluric lines.

### 3.4. Telluric line modeling

The modeling of the residual telluric spectrum was performed using the `molecfit` package in version 1.5.9 (Smette et al. 2015; Kausch et al. 2015) and the molecular line list `aer`<sup>6</sup> in version 3.6. The altitude stratification of temperature, pressure, and molecular abundances serves as input for LBLRTM. To create this profile, `molecfit` merges information from three sources: (1) a reference atmospheric profile, (2) Global Data Assimilation System (GDAS) profiles<sup>7</sup>, and (3) measurements of the ambient conditions obtained during the time of observations. In this study, we used a nightly mid-latitude (45°) reference model atmosphere<sup>8</sup> as reference profile. Beside the pressure and temperature distribution up to an altitude of 120 km as function of height on a 1 km grid, the profile also provides the abundances of 30 molecules. The GDAS profiles describe the pressure, temperature, and relative humidity as a function of 23 altitude levels up to roughly 26 km.

In the spectral modeling with `molecfit`, we let the abundances of O<sub>2</sub>, CO<sub>2</sub>, CH<sub>4</sub>, and the atmospheric water vapor content vary freely. We carried out the model fitting over broad wavelength ranges that cover large portions of the molecular bands taking full advantage of numerous unsaturated telluric lines contained in the CARMENES optical and near-infrared

<sup>6</sup> <http://rtweb.aer.com/>

<sup>7</sup> <https://www.ready.noaa.gov/gdas1.php>

<sup>8</sup> <http://eodg.atm.ox.ac.uk/RFM/atm/>

<sup>5</sup> We discuss the validity of this approximation in Appendix B.



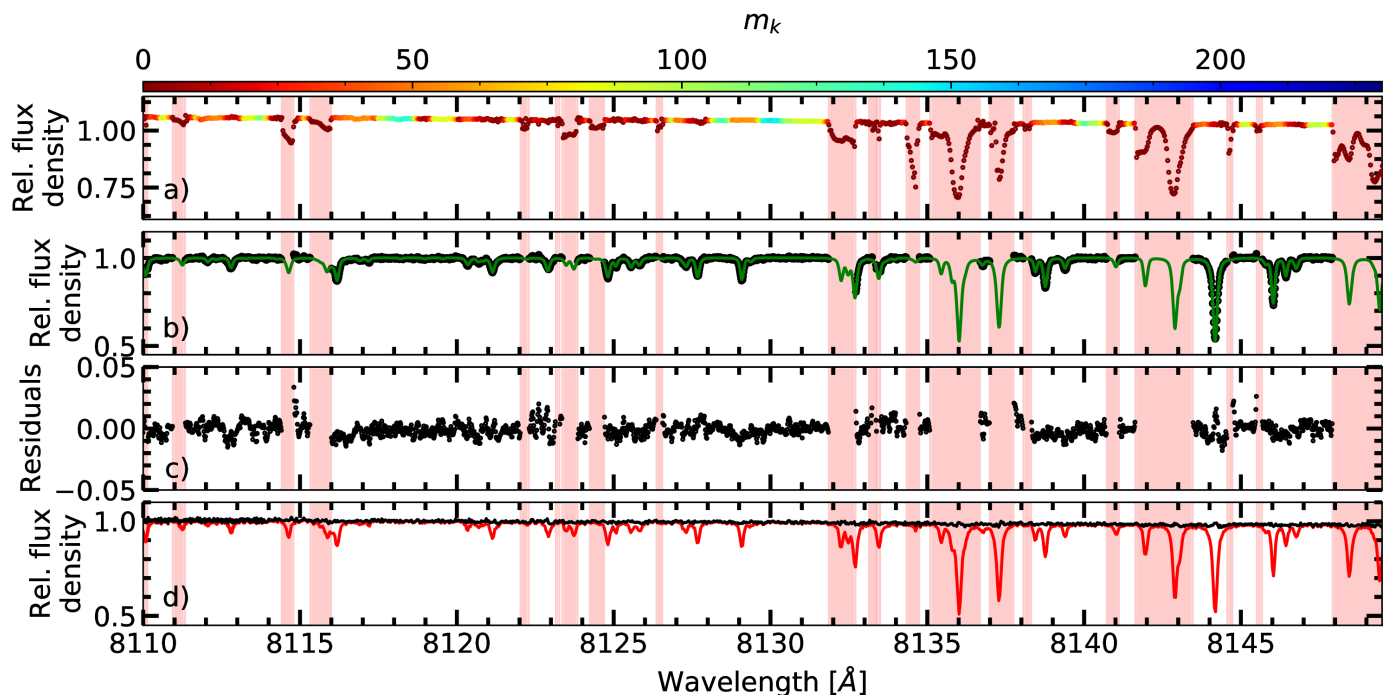


Fig. 3. Same as Fig. 2 but for the telluric standard star 109 Vir.

channel; the selected fitting intervals are given in Table 2. In the modeling, the continuum level within the fitting ranges was approximated with a low order polynomial. Since small errors in the wavelength calibration result in large residuals in the corrected spectra, we also allowed a Doppler shift of the transmission model to match the observed spectrum. In this way, instrumental drifts can be accounted for in the modeling. Wavelength ranges for which no stellar template was available ( $m_k = 0$ ) were excluded from the fit along with sections affected by sky emission features.

*Molecfit* requires the instrumental line spread function in the modeling. In the case of CARMENES, this can be represented by a combination of two profiles, one Gaussian and one Lorentzian profile. We performed an extensive analysis to derive appropriate parameters for the line spread functions in both CARMENES channels based on calibration data (see Appendix A). Therefore, the parameters of the line spread function are not free in the modeling.

### 3.5. Telluric line removal

Having fitted a transmission model to the residual telluric spectrum with *molecfit*, we used the best-fit parameters as input to compute a synthetic transmission model over the entire wavelength range of the observation with the *calctrans* module of *molecfit*. To derive the spectrum corrected for telluric lines  $F_{n,i}$ , we finally divide the CARMENES observation by the transmission model  $T(\lambda_{n,i})$

$$F_{n,i} = \frac{f_{n,i}}{T(\lambda_{n,i})}. \quad (5)$$

As an example, we show the observed and the telluric corrected spectrum of GJ 273 in Fig. 2d.

## 4. Results and discussion

### 4.1. Correction accuracy

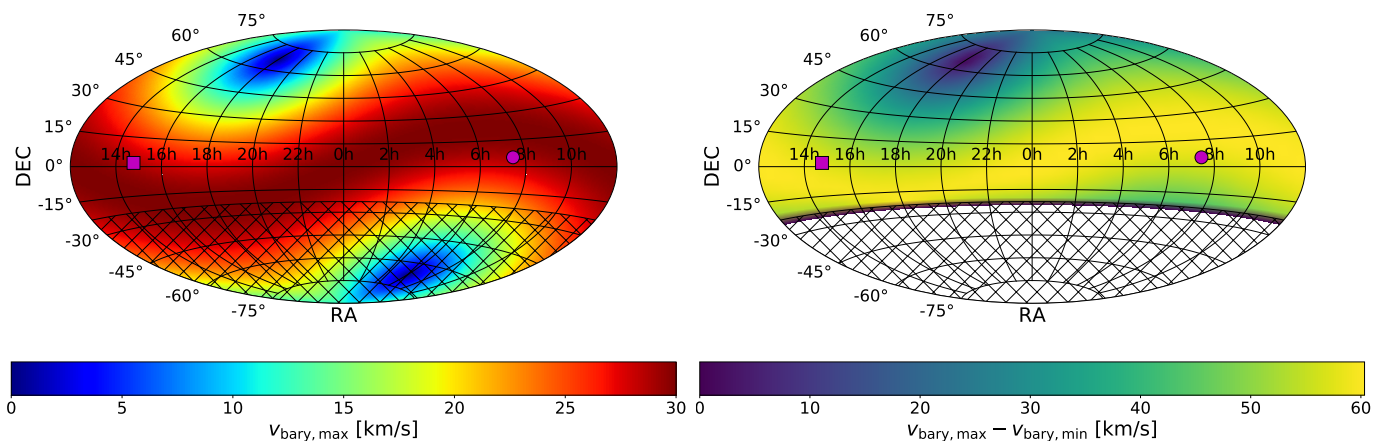
To demonstrate the use and evaluate the performance of the TDTM approach, we applied it to optical and near-infrared CARMENES observations of the TSS 109 Vir and the M dwarf GJ 273. We present an example of the correction procedure for 109 Vir in Fig. 3. Panel *a*) shows the template spectrum, which is free of stellar lines. Wavelength ranges where  $m_k$  is zero are heavily affected by tellurics. The template is noisier in wavelength ranges where  $m_k$  small (e.g. at 8121 Å). To obtain a more robust template, the  $m_k$  limit can be increased.

The correction accuracy strongly depends on the S/N of the data and the depth of the telluric features. As shown in Fig. 3d, micro-tellurics and lines with up to  $\sim 50\%$  depth can be corrected basically to within the noise level. Deeper lines are problematic for two reasons. First, the S/N decreases in their cores and, second, lines deeper than 50% leave comparatively large systematic residuals in the corrected spectra especially in the line cores. These residuals may be attributed to the fact that small discrepancies between model and observation can result in large residuals, especially in deep lines. These discrepancies may result from uncertainties of the line strengths listed in the HITRAN database, leading to inaccurate column density fits (Seifahrt et al. 2010; Gordon et al. 2011). Potential uncertainties in the line positions affect the wavelength calibration causing P Cygni-like residuals in the worst cases. Incomplete corrections may also arise from the instrumental line profile model. In fact, the Gaussian and Lorentzian profile parameters from different lines show some scatter and are approximated by a constant value (see Appendix A). Another source of uncertainty is the approximation of Eq. (1) by Eq. (2), which becomes particularly relevant in the case of blends between telluric and stellar lines (Sameshima et al. 2018, Appendix B).

To evaluate the accuracy of the telluric removal we identified wavelength ranges in the spectrum of 109 Vir that do not contain

**Table 3.** Individual wavelength ranges of O<sub>2</sub>, H<sub>2</sub>O, and CO<sub>2</sub> bands used to assess the quality of the telluric correction in spectra of 109 Vir.

| Species          | Telluric corrected   |                      |                    | Reference            |                      |                    |
|------------------|----------------------|----------------------|--------------------|----------------------|----------------------|--------------------|
|                  | $\lambda_{\min}$ [Å] | $\lambda_{\max}$ [Å] | $\bar{\sigma}$ [%] | $\lambda_{\min}$ [Å] | $\lambda_{\max}$ [Å] | $\bar{\sigma}$ [%] |
| O <sub>2</sub>   | 6277                 | 6323                 | 1.1                | 6265                 | 6275                 | 0.6                |
| O <sub>2</sub>   | 6924                 | 6964                 | 0.5                | 6850                 | 6865                 | 0.7                |
| H <sub>2</sub> O | 7258                 | 7325                 | 0.6                | 7440                 | 7480                 | 0.5                |
| O <sub>2</sub>   | 7676                 | 7715                 | 0.8                | 7720                 | 7755                 | 0.5                |
| H <sub>2</sub> O | 8219                 | 8247                 | 1.1                | 8247                 | 8254                 | 0.5                |
| H <sub>2</sub> O | 9810                 | 9856                 | 0.9                | 9880                 | 9910                 | 0.6                |
| O <sub>2</sub>   | 12490                | 12576                | 1.0                | 12440                | 12460                | 0.6                |
| CO <sub>2</sub>  | 15990                | 16023                | 1.1                | 15930                | 15970                | 1.0                |


**Fig. 4.** Sky maps in Aitoff projection of the maximum absolute barycentric RV  $v_{\text{bary,max}}$  as derived from Eq.(8) (left panel) and full amplitude of the barycentric RV  $v_{\text{bary,max}} - v_{\text{bary,min}}$  (right panel) for nights when the star is observable above 30° over the horizon for the location of the Calar Alto Observatory. Marked are the positions of 109 Vir (purple square) and GJ 273 (purple circle). The hatching pattern indicates the visibility cut-off at  $\delta < -23^\circ$  of the CARMENES GTO survey.

stellar features but are contaminated with telluric lines of different strengths attributable to one molecular species. For each of these ranges, we defined a nearby wavelength region with similar S/N, which is basically free of telluric lines to serve as a reference. After we applied our correction, we continuum-normalized those wavelength intervals and computed the standard deviation of the spectral bins  $\sigma$ . The results for several telluric bands are presented in Table 3. Our analysis confirms that unsaturated telluric absorption features are corrected to within 2% or better of the continuum standard deviation as reported by Smette et al. (2015). For objects with numerous intrinsic features, the authors proposed to apply *molecfit* to TSSs observations taken with the same instrumental setup as the science object, to solve for the polynomial continuum coefficients, and use the results as fixed input to subsequently apply *molecfit* to the science observation and to carry out the telluric correction. Our approach, however, is able to accurately and directly extract telluric features of various strengths for wavelength ranges with  $m_k > 0$ , even for feature-rich objects like M dwarfs, whose spectra are dominated by numerous molecular features in the optical and near-infrared bands.

For GJ 273 we show further examples of telluric contaminated wavelength ranges containing molecular bands of O<sub>2</sub>, H<sub>2</sub>O, and CO<sub>2</sub> in the Appendix (Figs. C.1 and C.2). Notably, molecular bands with an evenly spaced line structure such as the CO<sub>2</sub> band at  $\sim 1.6 \mu\text{m}$  can be almost fully restored (Fig. C.2).

#### 4.2. Visibility constraints

For the TDTM technique to work properly, a good template is essential. While a lack of S/N may be addressed by taking more observations, which may pose a practical but not a fundamental problem, the relative shift between telluric and stellar lines is also crucial for the template construction. In the case of planet-induced reflex motion, the barycentric motion of the Earth and its rotation dominate the sum of relative shifts. The maximum absolute barycentric velocity  $v_{\text{bary,max}}$  depends on the ecliptic latitude  $\beta$  of a target

$$v_{\text{bary,max}} \approx 30 \text{ km s}^{-1} |\cos \beta|. \quad (6)$$

The transformation from the equatorial ( $\lambda, \beta$ ) to the ecliptic system ( $\alpha, \delta$ ) with the inclination of the Earth  $\varepsilon \approx 23^\circ$  yields

$$\sin \beta = \sin \delta \cos \varepsilon - \cos \delta \sin \alpha \sin \varepsilon. \quad (7)$$

Thus  $v_{\text{bary,max}}$  as a function of  $\alpha$  and  $\delta$  reads

$$v_{\text{bary,max}}(\alpha, \delta) \approx 30 \text{ km s}^{-1} \sqrt{1 - \sin^2 \beta(\alpha, \delta)}, \quad (8)$$

which provides a sky map as in the left panel of Fig. 4 showing the maximum offset between telluric lines and stellar lines. Except for objects situated near the ecliptic poles,  $v_{\text{bary,max}}$  is larger than the natural line width of the tellurics and the instrumental resolution ( $\sim 3 \text{ km s}^{-1}$ ), which is required to disentangle the stellar and telluric spectra.

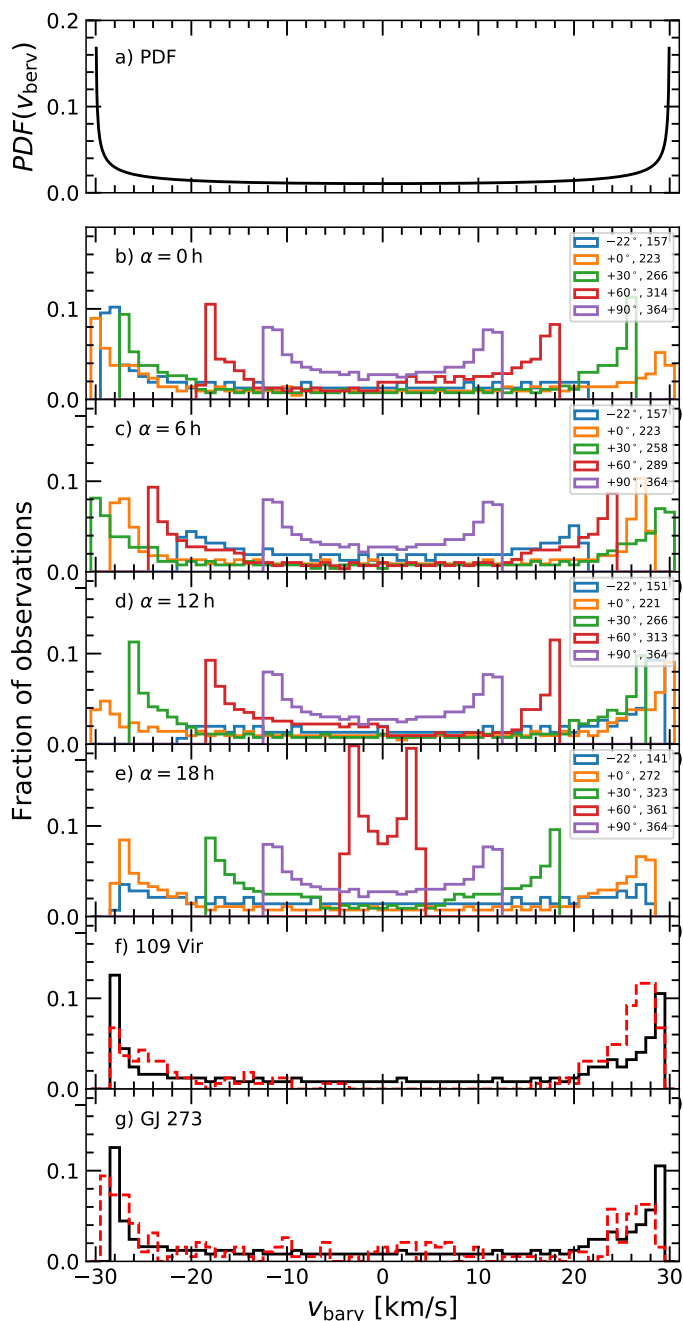


**Fig. 5.** *Panel a:* Probability density function  $PDF(v_{\text{bary}})$  as computed with Eq.(11). *Panels b-e:* Simulated barycentric velocity distributions for targets with  $\alpha = 0$  h, 6 h, 12 h, and 18 h, and  $\delta = -22^\circ, 0^\circ, +30^\circ, +60^\circ, +90^\circ$ , assuming one daily measurement over a time span of one year and considering the target visibility. The second entry in the legend is the number of total observing nights. *Panels f-g:* Simulated barycentric velocity distribution of 109 Vir and GJ 273 (black lines). Overplotted are the barycentric velocity distributions for the datasets of 109 Vir and GJ 273 (red dashed lines).

To examine the largest possible improvement on the template completeness, we carried out a simulation of the full amplitude of the barycentric velocity range  $v_{\text{bary,max}} - v_{\text{bary,min}}$  as a function of ecliptic coordinates down to the visibility cut-off for stars with  $\delta < 23^\circ$ , which is also the CARMENES GTO survey limit (Garcia-Piquer et al. 2017). In particular, we computed the dates

on which a target is  $30^\circ$  above the horizon between the astronomical dusk and dawn for the location of the Calar Alto Observatory and calculated the barycentric RV at midnight for those dates. In the right panel of Fig. 4 we show the difference between the maximum and minimum barycentric RV  $v_{\text{bary,max}} - v_{\text{bary,min}}$  for each pair of coordinates.

The observed barycentric velocity range is further constrained by the visibility. The main contribution to the barycentric velocity is a yearly sinusoid. We consider an object with a half-year visibility period, during which the barycentric Earth RV changes from a maximum to a minimum. In particular, we can consider the first half of a cosine

$$v_{\text{bary}}(t) = v_{\text{bary,max}} \cdot \cos\left(\frac{2\pi t}{T_{\oplus}}\right), \quad (9)$$

where  $T_{\oplus}$  is the orbital period of the Earth. When the target is observed at a random time, the probability to observe a barycentric RV shift equal or smaller than  $v_{\text{obs}}$  is

$$P(v_{\text{bary}} \leq v_{\text{obs}}) = 1 - \frac{1}{\pi} \arccos\left(\frac{v_{\text{obs}}}{v_{\text{bary,max}}}\right). \quad (10)$$

The probability density function ( $PDF(v_{\text{bary}})$ ) to observe the target in some interval of barycentric velocity is given by

$$PDF(v_{\text{bary}}) = \frac{1}{\pi v_{\text{bary,max}} \sqrt{1 - \left(\frac{v_{\text{bary}}}{v_{\text{bary,max}}}\right)^2}}, \quad (11)$$

which is shown in Fig. 5a.

To study the barycentric velocity distribution as a function of right ascension and declination over one year for the location of the Calar Alto Observatory, we carried out simulations for a set of coordinates with  $\alpha = 0$  h, 6 h, 12 h, and 18 h, and  $\delta = 0^\circ, +30^\circ, +60^\circ, +90^\circ$ . In addition, we included a southern coordinate sample with  $\delta = -22^\circ$ , which is near the visibility limit of the CARMENES survey. Assuming that objects can generally only be observed down to an elevation of  $30^\circ$ , we determined the nights when the target is observable and computed the barycentric velocity at the time between evening and morning astronomical twilight. Our results are presented in Fig. 5b-e. The simulated distributions show a flat plateau around  $v_{\text{bary}} = 0$  and increase at both ends where  $v_{\text{bary}} \rightarrow \pm v_{\text{bary,max}}$ . This shape is a consequence of the regular sampling of the yearly sinusoidal barycentric velocity contribution. However, the simulations show that all barycentric velocities between  $-v_{\text{berv,max}}$  and  $+v_{\text{berv,max}}$  are covered. We finally present the predicted and observed barycentric velocity distributions of 109 Vir (Fig. 5f) and GJ 273 (Fig. 5g) of our spectroscopic data sets.

#### 4.3. Total masking fraction

A mask that flags telluric features deeper than 1% results in a total masking fraction  $\gamma_{\text{max,VIS}} = 33.6\%$  for the optical spectral range ( $0.52\text{--}0.96\ \mu\text{m}$ ) and  $\gamma_{\text{max,NIR}} = 59.1\%$  for the near-infrared ( $0.96\text{--}1.71\ \mu\text{m}$ ). For the default 5% mask provided by SERVAL we derive total masking fractions of  $\gamma_{\text{max,VIS}} = 14.6\%$  and  $\gamma_{\text{max,NIR}} = 37.1\%$ . As the number of observations with different barycentric velocities is increased, the total masked fraction decreases and converges to a limit of  $\gamma_{\text{min,VIS}} = 17.1\%$  and  $\gamma_{\text{min,NIR}} = 39.1\%$  for the 1% mask, and  $\gamma_{\text{min,VIS}} = 5.2\%$  and  $\gamma_{\text{min,NIR}} = 19.8\%$  for the 5% default mask from SERVAL. These limits are mainly defined by broad telluric features, e.g.

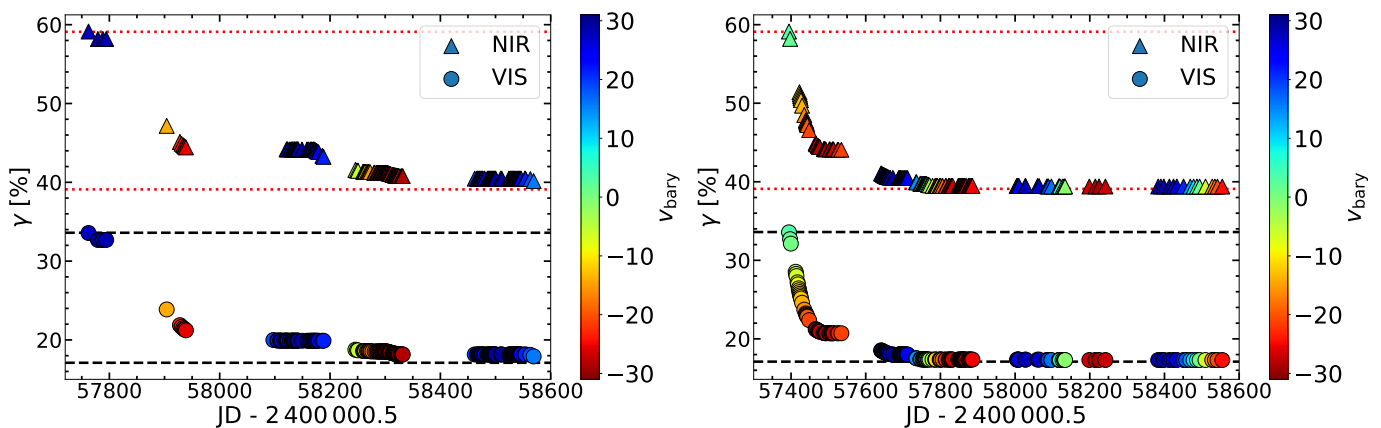


**Fig. 6.** Evolution of the total masked wavelength fraction color-coded with the barycentric velocity for 109 Vir (left) and GJ 273 (right). The circles represent the VIS channel and the triangles the NIR channel. The upper and lower dashed black lines mark the maximum and minimum limits of the total masked fraction in the optical wavelength range. The dotted red lines mark the same limits for the near-infrared wavelength range.

the strong water bands centered around  $1.15\ \mu\text{m}$  and  $1.4\ \mu\text{m}$ , which prevent further reduction of masked regions.

The difference between the maximum and minimum masking fraction is the total fraction that is gained for the modeling of the telluric spectrum, which is  $\gamma'_{\text{max,VIS}} = 16.5\%$  in the optical and  $\gamma'_{\text{max,NIR}} = 20.0\%$  in the near-infrared employing the 1% mask, and  $\gamma'_{\text{max,VIS}} = 9.4\%$  and  $\gamma'_{\text{max,NIR}} = 17.3\%$  for the default 5% mask. In the VIS, the useable amount of the stellar spectrum was increased from 66.4% to 82.9%, which corresponds to a growth of 24.9% for the 1% mask. The increment is even larger in the NIR, where we find that the useable range was increased from 40.9% to 60.9%, which corresponds to a growth of 48.9%. For the 5% mask we extend the useable range from 85.4% to 94.8% by 11.0% in the VIS and from 62.9% to 80.2% by 27.5% in the NIR.

We show the evolution of the total masked fraction using the 1% mask for 109 Vir and GJ 273 in Fig. 6. To reach the lower limit of the total masked fraction it is necessary to cover the full range of barycentric velocities. As shown in Fig. 6, this requirement was fulfilled for GJ 273 after the first observing season. In the case of 109 Vir, the lack of observations with barycentric velocities between  $-3\ \text{km s}^{-1} < v_{\text{berv}} < 15\ \text{km s}^{-1}$  (see Fig. 5) prevented reaching the lower limit of the total masked fraction. However, as shown in Fig. 6, only a few observations at  $\sim \pm 30\ \text{km s}^{-1}$  are required to substantially decrease the total masked fraction. Moreover, we found in our simulations that six observations equally distributed in the barycentric velocity space of  $\pm 30\ \text{km s}^{-1}$  are sufficient to reach a value of 17.9% in VIS and 40.3% in NIR.

#### 4.4. Impact on RV measurements

To study the impact of the telluric correction on the RV precision in the wavelength range covered by the VIS and NIR channel of CARMENES, we applied our method to 22 VIS and 13 NIR observations of the RV-quiet star GJ 1012. We then derived RVs using both the original spectra and those corrected for telluric absorption. Using spectra without any telluric correction, we derived RVs employing the default 5% telluric mask provided by SERVAL (Zechmeister et al. 2018). To take advantage of the more extended wavelength range accessible after telluric correction, we followed the procedure described in Sect. 3.2 to

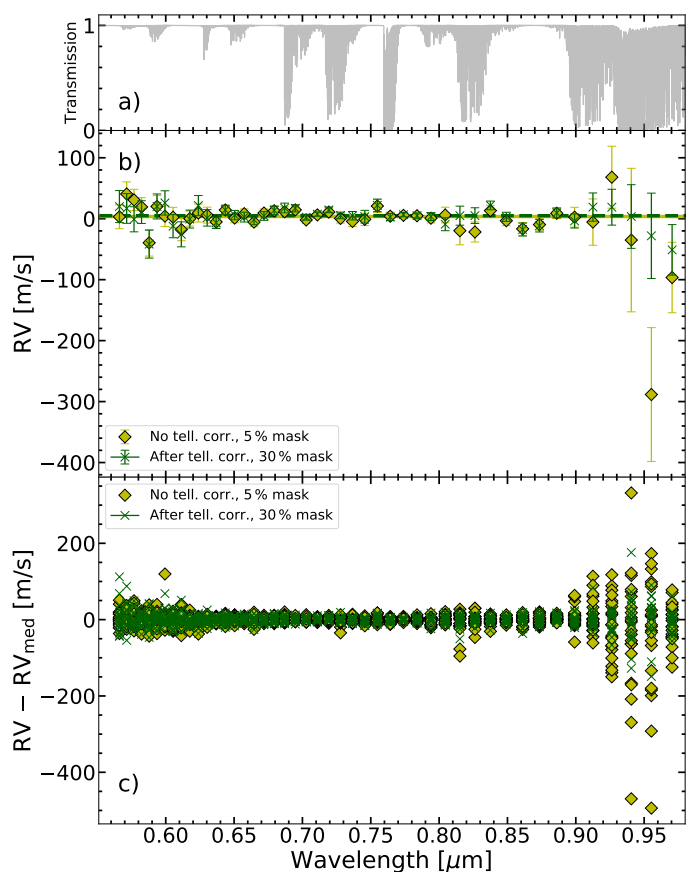


**Fig. 7.** *Panel a:* Synthetic transmission spectrum covering the wavelength range of the CARMENES VIS channel. *Panel b:* Radial velocities measured in 46 spectral orders before (yellow diamonds) and after telluric correction (green crosses) of one CARMENES VIS observation of GJ 1012. The horizontal lines indicate the median RVs before (solid yellow) and after telluric correction (dashed green). *Panel c:* Difference between measured and median RVs calculated in 46 spectral orders before (yellow diamonds) and after telluric correction (green crosses) using 22 CARMENES VIS observations of GJ 1012.

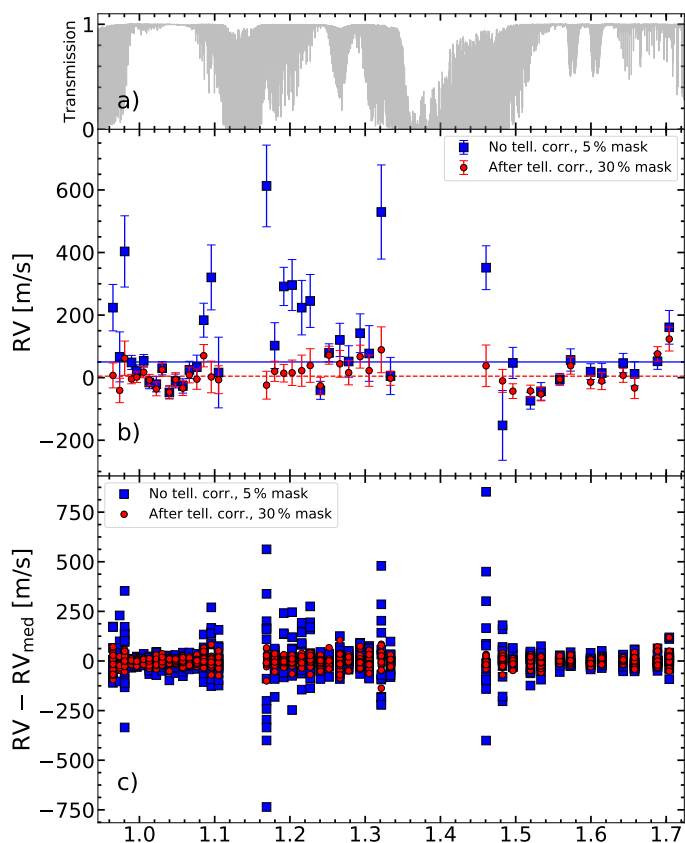


**Fig. 8.** *Panel a:* Synthetic transmission spectrum covering the wavelength range of the CARMENES NIR channel. *Panel b:* Radial velocities measured in 44 spectral orders before (blue squares) and after telluric correction (red circles) of one CARMENES NIR observation of GJ 1012. The horizontal lines indicate the median RVs before (solid blue) and after telluric correction (dashed red). *Panel c:* Difference between measured and median RVs calculated in 44 spectral orders before (blue squares) and after telluric correction (red circles) using 13 CARMENES NIR observations of GJ 1012.

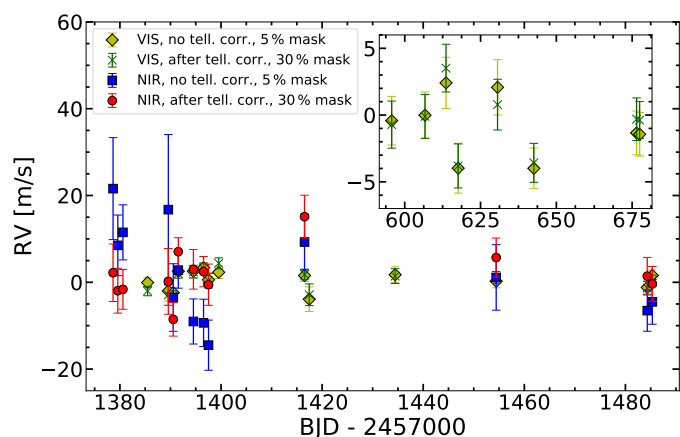


**Fig. 9.** Radial velocity measurements before (VIS: yellow diamonds; NIR: blue squares) and after (VIS: green crosses; NIR: red circles) the telluric correction as a function of barycentric Julian Date for GJ 1012 obtained with the VIS and NIR channel of CARMENES. The first eight VIS RVs are shown in the inset for the sake of clarity.

construct a less conservative telluric mask, excluding only spectral regions, which are affected by atmospheric transmission features deeper than 30%. We used this mask to determine RVs from telluric corrected observations.

We show the RV measurements before and after the telluric correction per spectral order exemplarily for one single VIS and NIR spectrum in Fig. 7b and Fig. 8b, respectively. The weighted medians over the RVs computed over all orders are indicated by the horizontal lines. In addition, a synthetic atmospheric transmission spectrum is plotted in Fig. 7a and Fig. 8a to illustrate the location of the telluric absorption bands. The largest impact of the telluric correction obviously occurs in orders that are strongly affected by telluric absorption. In the VIS range we found a lower RV dispersion in orders covering the water bands from 0.90 to 0.97  $\mu\text{m}$ . A less pronounced improvement was found for orders that are affected by the water band located between 0.80 and 0.85  $\mu\text{m}$ . The wavelength range at 0.56-0.62  $\mu\text{m}$ , however, shows a somewhat odd behavior. Although this range is covered by rather shallow telluric features, the telluric correction causes a slight increase of the RV scatter. A visual inspection of these orders did not reveal indications for an inaccurate telluric correction. Despite a thorough examination with regard to our procedure and the RV determination, the reason remains unclear. For the NIR channel we found that RVs determined in orders close to the nearly opaque water bands centered at about 0.95, 1.14, and 1.40  $\mu\text{m}$  differ by up to several hundreds of  $\text{m s}^{-1}$ . In contrast, the RVs measured in orders that are less strongly affected by telluric contamination, for instance at 0.78 and 0.82  $\mu\text{m}$  in the VIS and the wavelength region between 1.02 and 1.06  $\mu\text{m}$  in the NIR, are consistent.

We then extended our analysis to the entire VIS and NIR sample of GJ 1012 using the spectra before and after the telluric correction and investigated the impact of the correction by considering the difference between the RVs measured in the individual orders and the resulting median RV values. Our results are presented in Fig. 7c for the VIS channel and in Fig. 8c for the NIR channel. The behavior is similar to that in the case of a single observation. In particular, we found that our correction strongly affects those orders that are most heavily contaminated with telluric features. The inspection of the whole sample confirms that the telluric correction does not yield an improvement in the RV precision in the orders around 0.56-0.62  $\mu\text{m}$ .

We show the VIS and NIR RV time series derived before and after telluric correction in Fig. 9. To account for systematic instrumental drifts, we corrected the RVs for nightly zero-point offsets, which were obtained from a sample of RV-quiet stars with RV variations smaller than 10  $\text{m s}^{-1}$  observed in the same night (Trifonov et al. 2018; Tal-Or et al. 2019). In the VIS channel, we determined a weighted rms of 2.2  $\text{m s}^{-1}$  using RVs measured from uncorrected spectra and 2.3  $\text{m s}^{-1}$  for those measured from corrected spectra. The slight increase of the rms value can be mainly explained by the larger RV dispersion of the bluest VIS orders. In the heavily contaminated red orders of the VIS arm the RV scatter is decreased by several hundreds  $\text{m s}^{-1}$ , which leads to a consistent set of RVs also in these orders. Over the entire VIS arm, this gain is nearly counterbalanced by additional RV scatter in the wavelength range below 0.62  $\mu\text{m}$ , which we attribute to the telluric correction. In the case of the NIR channel, the rms was considerably reduced from 9.5  $\text{m s}^{-1}$  for the RVs derived from the uncorrected spectra to 5.7  $\text{m s}^{-1}$  for those derived after the correction. Our results are listed in Table 4.

The lower limit of achievable RV precision is defined by the internal RV precision  $\sigma_{\text{int}}$  and depends on the S/N of each observation and the spectral information content (Quirrenbach et al.

**Table 4.** Weighted rms and median internal precisions  $\tilde{\sigma}_{\text{int}}$  derived from VIS and NIR RVs of GJ 1012 before and after telluric correction.

|                                     | Before |     | After |     |
|-------------------------------------|--------|-----|-------|-----|
|                                     | VIS    | NIR | VIS   | NIR |
| rms [m/s]                           | 2.2    | 9.5 | 2.3   | 5.7 |
| $\tilde{\sigma}_{\text{int}}$ [m/s] | 1.6    | 6.3 | 1.5   | 4.6 |

2018). By including spectral ranges that were masked before the telluric correction, the usable amount of the stellar spectrum and therefore the spectral information content is increased, thus, resulting in a reduction of  $\sigma_{\text{int}}$  in both channels after the correction. The improvement in the VIS channel is rather moderate, where the median internal RV precision  $\tilde{\sigma}_{\text{int}}$  drops down from  $1.6 \text{ m s}^{-1}$  before the correction to  $1.5 \text{ m s}^{-1}$  afterwards. In the NIR channel, however, we obtain a substantial enhancement where  $\tilde{\sigma}_{\text{int}}$  falls from  $6.3 \text{ m s}^{-1}$  before the correction to  $4.6 \text{ m s}^{-1}$  after the correction. Again, we provide our findings in Table 4. Our results in the near-infrared demonstrate that telluric contaminated wavelength regions carry a significant amount of RV information, which is accessible after the correction. In fact, the rms in the NIR channel after the correction is  $5.7 \text{ m s}^{-1}$  and therefore below the internal precision limit of  $6.3 \text{ m s}^{-1}$  before the correction. The use of a less conservative mask, for instance a 40% mask, is expected to engender an even larger improvement of  $\sigma_{\text{int}}$ .

## 5. Summary and conclusions

We have presented the TDTM technique, a combination of data-driven (template construction) and forward-modeling (spectral fitting) methods to correct for telluric absorption lines in high-resolution optical and near-infrared spectra. After applying a telluric mask to a time series of spectra, we construct a high S/N stellar template, and use it to remove the stellar contribution from the observations. We then use `molecfit` to fit an atmospheric transmission model to the resulting telluric spectrum and finally correct the target spectrum at all wavelengths. While the telluric correction via spectral modeling with `molecfit` alone is especially challenging for late type stars with their high density of molecular lines, the TDTM technique is applicable to spectra of any spectral type. Although we chose the `molecfit` code to fit the transmission model to the telluric spectra in this work, other software packages that produce synthetic atmospheric transmission spectra, such as the `TelFit`<sup>9</sup> (Gullikson et al. 2014) or `TAPAS`<sup>10</sup> code (Bertaux et al. 2014), could be used.

Telluric correction with our method works best with a high number of observations and good coverage of the barycentric velocity space. To demonstrate the performance of our correction method we applied it to high-resolution optical and near-infrared CARMENES observations of 109 Vir and GJ 273. We found that `molecfit` corrects telluric lines with a depth of up to  $\sim 50\%$  close to the noise level in the residual telluric transmission spectrum obtained with the help of the template.

We investigated the impact of telluric features and our correction on high-precision RVs using real data and present the improvement in RV that can be achieved in the optical and the near-infrared wavelength range. After we applied our telluric correction approach to a time series of 22 VIS and 13 NIR spectra of

the RV-quiet M4.0 V star GJ 1012 obtained with CARMENES, we determined the RVs using a 30% telluric mask and compared them to the RVs derived with the standard RV pipeline `SERVAL`, which employs a telluric masking with a 5% mask. By exploring the RV signals in the different spectral orders, we find that the largest impact can be attributed to the most severely affected orders adjacent to the strong water bands at 0.82, 0.95, 1.14, and  $1.40 \mu\text{m}$ .

Despite improvement in the red part of the VIS arm, no significant improvement in RV precision was obtained considering the entire VIS arm of CARMENES. In fact, a slight increase of the rms from  $2.2 \text{ m s}^{-1}$  for the uncorrected spectra compared to an rms of  $2.3 \text{ m s}^{-1}$  for the corrected spectra was found. This indicates that a telluric binary mask is sufficient in the case of objects with a large RV information content at optical wavelengths. However, for observations at high airmass and objects with fewer spectral features such as Sun-like stars, a comprehensive treatment of the telluric lines may still be necessary (Luque et al. 2019).

In the near-infrared wavelength range, we find that telluric contamination is strongly alleviated by the TDTM technique and, thus, the usable fraction of the spectrum increases. An improved telluric correction in the near-infrared is relevant for spectral analysis and of course the measurement of RVs. Our telluric correction decreases the RV scatter and improves the rms from  $9.5 \text{ m s}^{-1}$  for uncorrected spectra, where features deeper than 5% are simply masked, to  $5.7 \text{ m s}^{-1}$  for telluric corrected spectra.

As a consequence of the increase of the usable stellar spectrum, the examination of the median internal RV precision revealed a moderate enhancement from  $1.6$  to  $1.5 \text{ m s}^{-1}$  in the VIS channel and a considerable improvement from  $6.3$  to  $4.7 \text{ m s}^{-1}$  in the NIR channel. With our approach, we made the stellar information content in regions with moderate telluric contamination accessible and used it to improve the RV precision. Our results highlight the importance of a proper telluric line treatment in the analysis of near-infrared spectra and the determination of RVs. The improvement in near-infrared RV precision enables us to search for Earth-like planets around M dwarfs more efficiently, in particular, the those very late-type M dwarfs, which are too faint in the VIS arm regime.

*Acknowledgements.* CARMENES is an instrument for the Centro Astronómico Hispano-Alemán de Calar Alto (CAHA, Almería, Spain). CARMENES is funded by the German Max-Planck-Gesellschaft (MPG), the Spanish Consejo Superior de Investigaciones Científicas (CSIC), the European Union through FEDER/ERF FICTS-2011-02 funds, and the members of the CARMENES Consortium (Max-Planck-Institut für Astronomie, Instituto de Astrofísica de Andalucía, Landessternwarte Königstuhl, Institut de Ciències de l’Espai, Institut für Astrophysik Göttingen, Universidad Complutense de Madrid, Thüringer Landessternwarte Tautenburg, Instituto de Astrofísica de Canarias, Hamburger Sternwarte, Centro de Astrobiología and Centro Astronómico Hispano-Alemán), with additional contributions by the Spanish Ministry of Economy, the German Science Foundation through the Major Research Instrumentation Programme and DFG Research Unit FOR2544 “Blue Planets around Red Stars”, the Klaus Tschira Stiftung, the states of Baden-Württemberg and Niedersachsen, and by the Junta de Andalucía. Based on data from the CARMENES data archive at CAB (INTA-CSIC). We acknowledge financial support from the Agencia Estatal de Investigación of the Ministerio de Ciencia, Innovación y Universidades and the European FEDER/ERF funds through projects AYA2016-79425-C3-1/2/3-P, AYA2015-69350-C3-2-P, and the Centre of Excellence “Severo Ochoa” and “María de Maeztu” awards to the Instituto de Astrofísica de Canarias (SEV-2015-0548), Instituto de Astrofísica de Andalucía (SEV-2017-0709), and Centro de Astrobiología (MDM-2017-0737), and the Generalitat de Catalunya/CERCA programme. L.T.-O. acknowledges support from the Israel Science Foundation (grant No. 848/16).

<sup>9</sup> <https://pypi.org/project/TelFit/>

<sup>10</sup> Transmissions Atmosphériques Personnalisées pour l’Astronomie, <http://cds-espi.ipl.fr/tapas/>

## References

- Anglada-Escudé, G. & Butler, R. P. 2012, *ApJS*, 200, 15
- Artigau, É., Astudillo-Defru, N., Delfosse, X., et al. 2014, in *Proc. SPIE*, Vol. 9149, *Observatory Operations: Strategies, Processes, and Systems V*, 914905
- Bailey, J., Simpson, A., & Crisp, D. 2007, *PASP*, 119, 228
- Bedell, M., Hogg, D. W., Foreman-Mackey, D., Montet, B. T., & Luger, R. 2019, arXiv e-prints [arXiv:1901.00503]
- Bertaux, J. L., Lallement, R., Ferron, S., Boonne, C., & Bodichon, R. 2014, *A&A*, 564, A46
- Caballero, J. A., Guàrdia, J., López del Fresno, M., et al. 2016, *SPIE*, 9910, 0E
- Caccin, B., Cavallini, F., Ceppatelli, G., Righini, A., & Sambuco, A. M. 1985, *A&A*, 149, 357
- Clough, S. A., Shephard, M. W., Mlawer, E. J., et al. 2005, *J. Quant. Spec. Radiat. Transf.*, 91, 233
- Cutri, R. M., Skrutskie, M. F., van Dyk, S., et al. 2003, *VizieR Online Data Catalog*, II/246
- Donati, J.-F., Kouach, D., Lacombe, M., et al. 2018, *SPIROU: A NIR Spectropolarimeter/High-Precision Velocimeter for the CFHT*, 107
- Gaia Collaboration, Brown, A. G. A., Vallenari, A., et al. 2018, *A&A*, 616, A1
- García-Piquer, A., Morales, J. C., Ribas, I., et al. 2017, *A&A*, 604, A87
- Gordon, I. E., Rothman, L. S., & Toon, G. C. 2011, *Journal of Quantitative Spectroscopy and Radiative Transfer*, 112, 2310
- Gullikson, K., Dodson-Robinson, S., & Kraus, A. 2014, *AJ*, 148, 53
- Halverson, S., Terrien, R., Mahadevan, S., et al. 2016, in *Proc. SPIE*, Vol. 9908, *Ground-based and Airborne Instrumentation for Astronomy VI*, 99086P
- Husser, T.-O. & Ulbrich, K. 2014, in *Astronomical Society of India Conference Series*, Vol. 11, *Astronomical Society of India Conference Series*
- Husser, T.-O., Wende-von Berg, S., Dreizler, S., et al. 2013, *A&A*, 553, A6
- Kausch, W., Noll, S., Smette, A., et al. 2015, *A&A*, 576, A78
- Kotani, T., Tamura, M., Nishikawa, J., et al. 2018, *SPIE*, 10702, 11
- Kürster, M., Endl, M., Rouesnel, F., et al. 2003, *A&A*, 403, 1077
- Lockwood, A. C., Johnson, J. A., Bender, C. F., et al. 2014, *ApJ*, 783, L29
- Luque, R., Nowak, G., Pallé, E., et al. 2019, *A&A*, 623, A114
- Mahadevan, S., Ramsey, L. W., Terrien, R., et al. 2014, in *Proc. SPIE*, Vol. 9147, *Ground-based and Airborne Instrumentation for Astronomy V*, 91471G
- Quirrenbach, A., Amado, P. J., Ribas, I., et al. 2018, *SPIE*, 10702, 0W
- Reiners, A., Zechmeister, M., Caballero, J. A., et al. 2018, *A&A*, 612, A49
- Rothman, L. S., Gordon, I. E., Barbe, A., et al. 2009, *J. Quant. Spec. Radiat. Transf.*, 110, 533
- Royer, F., Zorec, J., & Gómez, A. E. 2007, *A&A*, 463, 671
- Rudolf, N., Günther, H. M., Schneider, P. C., & Schmitt, J. H. M. M. 2016, *A&A*, 585, A113
- Sameshima, H., Matsunaga, N., Kobayashi, N., et al. 2018, *PASP*, 130, 074502
- Seifahrt, A., Käufel, H. U., Zängl, G., et al. 2010, *A&A*, 524, A11
- Smette, A., Sana, H., Noll, S., et al. 2015, *A&A*, 576, A77
- Tal-Or, L., Trifonov, T., Zucker, S., Mazeh, T., & Zechmeister, M. 2019, *MNRAS*, 484, L8
- Trifonov, T., Kürster, M., Zechmeister, M., et al. 2018, *A&A*, 609, A117
- Vacca, W. D., Cushing, M. C., & Rayner, J. T. 2003, *PASP*, 115, 389
- Wildi, F., Blind, N., Reshetov, V., et al. 2017, *SPIE*, 10400, 18
- Zechmeister, M., Anglada-Escudé, G., & Reiners, A. 2014, *A&A*, 561, A59
- Zechmeister, M., Kürster, M., & Endl, M. 2009, *A&A*, 505, 859
- Zechmeister, M., Reiners, A., Amado, P. J., et al. 2018, *A&A*, 609, A12

## Appendix A: Instrumental line profile

For a proper modeling of the telluric lines, the line spread function (LSF) needs to be well known. In order to characterize the LSF, we analyze hollow cathode lamp spectra taken for the purpose of calibration before and after the science observations.

An accurate estimation of the line shape is not trivial, since the lines are sparsely sampled. Within each échelle order, the coverage of the FWHM of the LSF typically increases from around 2.5 to 4 pixels when moving along the main dispersion direction from the blue to the red part of the order. Due to several instrumental effects (e.g. temperature variations), the spectra move across the detector with time. We therefore combined multiple exposures to artificially increase the sampling. In the visual channel 1455 different lamp exposures (2605 in the near-infrared) have been used for this purpose. For each line investigated in that manner (114 in the near-infrared and 218 in the visual) the frames have been aligned so that the line was centered. Before combination they were normalized.

These superimposed line profiles are well suited to model the shape of the LSF. For this purpose we tested different profiles, namely Gaussians and Lorentzians, generalized Gaussians and Lorentzians with the exponent treated as an additional free parameter, as well as Voigt profiles. The analysis of all fits showed that a Voigt profile is most appropriate for the LSF modeling. The other profiles usually were not suitable to handle both the line cores and lobes properly at the same time.

In addition, we investigated the variations in the measured line widths,  $\Delta\lambda$ , across the detector and found that aside from some secondary, although significant, features near the detector edges (particularly in the blue part of the VIS sensor), the line widths still can be described in a consistent manner. The most dominant effect becomes apparent, when the widths of the lines are expressed in terms of wavelength. In the Voigt profile the overall width can be described by its Gaussian and Lorentzian components. Both are expected to show a linear trend in wavelength if the resolution is constant. However, when the entities are expressed in a wavelength independent way choosing units of  $\Delta\lambda/\lambda_c$ , where  $\lambda_c$  represents the central vacuum wavelength of the particular line, these normalized widths are expected to remain constant, if the resolution of the spectrograph is independent of wavelength.  $\Delta\lambda/\lambda_c$  can be directly measured from the widths of unresolved lines.

In Fig. A.1 the measured Gaussian and Lorentzian FWHM components of the Voigt profile are shown for both channels. The NIR channel has a somewhat lower resolution, and therefore wider Gaussian component than the VIS channel. However, the widths of the Lorentzian component are very similar for both channels.

To obtain robust estimates of the LSF parameters, we use medians for the FWHM of each component and channel to model the instrumental line spread function of CARMENES. These parameters are summarized in Table A.1. Due to the clearly visible deviation in the blue part of the visual channel we have considered only lines with a wavelength above 6000 Å. Also, the distribution of the Lorentzian component, particularly in the NIR part of the spectrum, shows some conspicuous features. Some outliers cluster around 12 500 Å, while the scatter seems generally increased for wavelengths above 15 000 Å. The reasons for those effects could not consistently and objectively be traced back to line blends or similar effects.

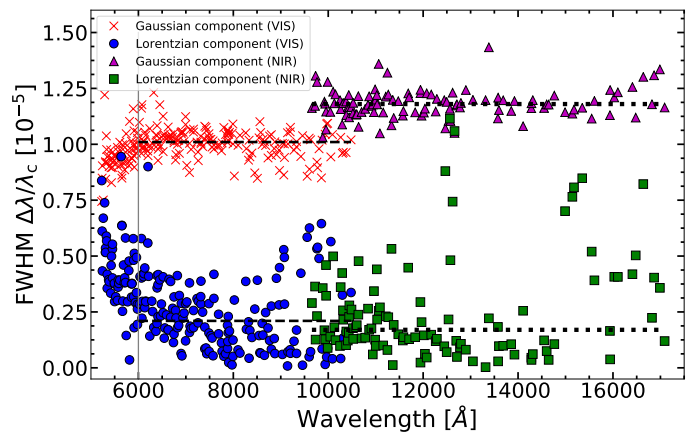


**Fig. A.1.** Measured Gaussian and Lorentzian FWHM components of Hollow cathode emission lines as a function of wavelength for the optical (VIS) and near-infrared (NIR) CARMENES spectrographs. The gray vertical line marks the cut-off wavelength at 6000 Å. The horizontal lines indicate median values of the Gaussian and Lorentzian FWHM components for the optical channel (dashed lines) and the near-infrared channel (dotted lines).

**Table A.1.** Median averaged Gaussian and Lorentzian FWHM.

| Channel        | #lines | $w_{\text{Gauss}} [\Delta\lambda/\lambda_c]$ | $w_{\text{Lorentz}} [\Delta\lambda/\lambda_c]$ |
|----------------|--------|--|--|
| VIS            | 218    | $1.00 \times 10^{-5}$                        | $2.8 \times 10^{-6}$                           |
| VIS (> 6000 Å) | 159    | $1.01 \times 10^{-5}$                        | $2.1 \times 10^{-6}$                           |
| NIR            | 114    | $1.18 \times 10^{-5}$                        | $1.7 \times 10^{-6}$                           |

## Appendix B: Approximation of the convolution equation

In an actual observation, the product of the stellar spectrum,  $s$ , and the telluric transmission spectrum,  $t$ , is received by the system of telescope and spectrograph, which we call the instrument. The effect of the instrument on the received spectrum is modeled by a convolution with the instrumental line spread function,  $L$ , so that we obtain the left hand side of the equation

$$[s(\lambda) \cdot t(\lambda)] \otimes L(\lambda) \approx [s(\lambda) \otimes L(\lambda)] \cdot [t(\lambda) \otimes L(\lambda)]. \quad (\text{B.1})$$

As the convolution cannot easily be inverted, the left hand side of Eq. (B.1) is frequently approximated as a product of two spectra separately convolved with the line spread function. As previously pointed out, e.g., by Sameshima et al. (2018), the two sides of the equation differ. In their analysis, Sameshima et al. (2018) found that a telluric-corrected spectrum based on this approximation noticeably differs from the stellar spectrum if the width of the stellar lines is comparable to or narrower than the instrumental resolution and if the stellar lines are heavily blended with telluric features.

We analytically investigate the difference between both sides of Eq. (B.1), making the simplifying assumption of normality for the stellar, telluric, and instrumental line profiles. In particular,



we adopt

$$s(\lambda) = \frac{A_s}{\sqrt{2\pi\sigma_s^2}} \exp\left(-\frac{(\lambda - \mu_s)^2}{2\sigma_s^2}\right) = A_s N(\mu_s, \sigma_s^2), \quad (\text{B.2})$$

$$t(\lambda) = A_t N(\mu_t, \sigma_t^2), \quad (\text{B.3})$$

$$L(\lambda) = N(0, \sigma_L^2). \quad (\text{B.4})$$

Substituting  $s(\lambda)$ ,  $t(\lambda)$ , and  $L(\lambda)$  into the left hand side of Eq. (B.1) leads to

$$\begin{aligned} & [s(\lambda) \times t(\lambda)] \otimes L(\lambda) \\ &= \frac{A_s A_t}{2\pi\sigma_z^2} \exp\left(-\frac{(\lambda - \mu_t)^2\sigma_s^2 + (\lambda - \mu_s)^2\sigma_t^2 + (\mu_s - \mu_t)^2\sigma_L^2}{2\sigma_z^4}\right) \quad (\text{B.5}) \\ &= a, \quad (\text{B.6}) \end{aligned}$$

where  $\sigma_z^4 = \sigma_s^2\sigma_t^2 + \sigma_s^2\sigma_L^2 + \sigma_t^2\sigma_L^2$  and  $a$  abbreviates Eq. (B.5). Using

$$s(\lambda) \otimes L(\lambda) = A_s N(\mu_s, \sigma_s^2 + \sigma_L^2) \quad (\text{B.7})$$

$$t(\lambda) \otimes L(\lambda) = A_t N(\mu_t, \sigma_t^2 + \sigma_L^2) \quad (\text{B.8})$$

we find that the substitution of  $s(\lambda)$ ,  $t(\lambda)$ , and  $L(\lambda)$  into the right hand side of Eq. (B.1) leads to

$$\begin{aligned} & [s(\lambda) \otimes L(\lambda)] \cdot [t(\lambda) \otimes L(\lambda)] = \\ & \frac{A_s A_t}{2\pi\sqrt{\sigma_s^4 + \sigma_L^4}} \exp\left(-\frac{(\lambda - \mu_s)^2}{2(\sigma_s^2 + \sigma_L^2)} - \frac{(\lambda - \mu_t)^2}{2(\sigma_t^2 + \sigma_L^2)}\right) = b, \quad (\text{B.9}) \end{aligned}$$

where  $b$  again abbreviates our findings.

### Appendix B.1: Estimating the difference

The details of the differences between the two sides of Eq. (B.1) depend on the summands represented by  $a$  and  $b$  and, therefore, the parameters  $\mu_{s,t}$ ,  $A_{s,t}$ , and  $\sigma_{s,t,L}$ . Naturally, some estimates can be obtained in special cases.

Assuming a perfectly blended stellar and telluric line  $\mu_s = \mu_t = \lambda$ , we obtain for the difference between Eq. (B.5) and Eq. (B.9)

$$\begin{aligned} a - b &= \frac{A_s A_t}{2\pi\sigma_z^2} \left(1 - \frac{1}{\sqrt{1 + \frac{\sigma_L^4}{\sigma_z^4}}}\right) \\ &= d_s d_t \frac{\sigma_s \sigma_t}{\sigma_z^2} \left(1 - \frac{1}{\sqrt{1 + \frac{\sigma_L^4}{\sigma_z^4}}}\right), \quad (\text{B.10}) \end{aligned}$$

where  $d_{s,t}$  denote the line depths

$$d_{s,t} = \frac{A_{s,t}}{\sqrt{2\pi\sigma_{s,t}^2}}. \quad (\text{B.11})$$

In general  $\sigma_z^2 \geq \sigma_s \sigma_t$ , and we find  $a - b \geq 0$  from which follows that  $a - b < d_s d_t \frac{\sigma_s \sigma_t}{\sigma_z^2}$ . Under the stated assumptions, we therefore find that the accuracy of the approximation depends on the product of the line depths, a fact that also follows from the linearity of the convolution operator in Eq. (B.1).

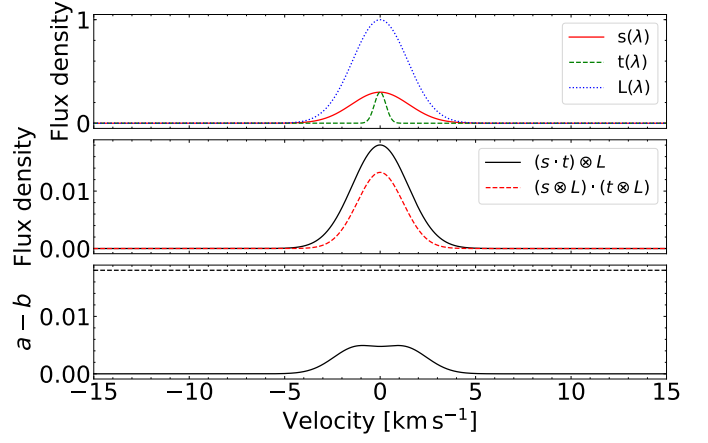


**Fig. B.1.** Approximation of the convolution function for the special case where a stellar line is blended by a telluric line ( $\mu_s = \mu_t$ ). *Upper panel:* Artificial line profiles representing a stellar line (red line), a telluric line (green dashed), and the instrumental line profile (blue dotted, normalized for the sake of clarity). *Middle panel:* Left and right side of Eq. (B.1). *Lower panel:* Difference between the left and right side of Eq. (B.1) expressed by  $a - b$ . The dashed line indicates the limit set by the product of the line depths  $d_s d_t \frac{\sigma_s \sigma_t}{\sigma_z^2}$ .

In Fig. B.1, we illustrate the differences between the two sides of Eq. (B.1) for the special case of a central blend of a stellar and a telluric line (i.e.,  $\mu_s = \mu_t$ ) for parameters appropriate for the CARMENES spectrograph. In our approximation, we consider only normal line profiles. We choose the standard deviation of the instrumental line profile,  $\sigma_L$ , such that its FWHM matches that of the true VIS channel Voigt line profile of CARMENES (Table A.1), which yields  $\sigma_L = 0.048 \text{ \AA}$ . We assumed stellar and telluric lines located at  $\mu_s = \mu_t = 10\,000 \text{ \AA}$  with line depths of  $d_s = 0.3$  and  $d_t = 0.3$ . The intrinsic stellar and telluric line widths (before convolution by the Instrumental line spread function) were estimated from a synthetic PHOENIX spectrum (Husser et al. 2013) and a telluric transmission model, which yields  $\sigma_s = 0.05 \text{ \AA}$  and  $\sigma_t = 0.01 \text{ \AA}$ . We present the resulting Gaussian profiles in the upper panel of Fig. B.1, the left and right side of Eq. (B.1) in the middle panel of Fig. B.1, and the difference  $a - b$  as well as the limit expressed by  $d_s d_t \frac{\sigma_s \sigma_t}{\sigma_z^2}$  in the lower panel of Fig. B.1. For the adopted parameters, the difference between the left and right side of Eq. (B.1) is approximately 0.5%. This is in the range of 2% cited as the correction accuracy of molecfit. For less deep lines, the effect is less pronounced. In the extreme case of very high instrument resolution represented by the limit  $\sigma_L \rightarrow 0$ , we find that  $\sigma_z^2$  approaches  $\sigma_s \sigma_t$  so that Eq. (B.10) approaches zero and the difference vanishes.

Our results allow to obtain an estimate of the accuracy of the approximation in Eq. (B.1) based on a normal approximation of the line profiles. They are also consistent with the findings of Sameshima et al. (2018).

## Appendix C: Additional plots

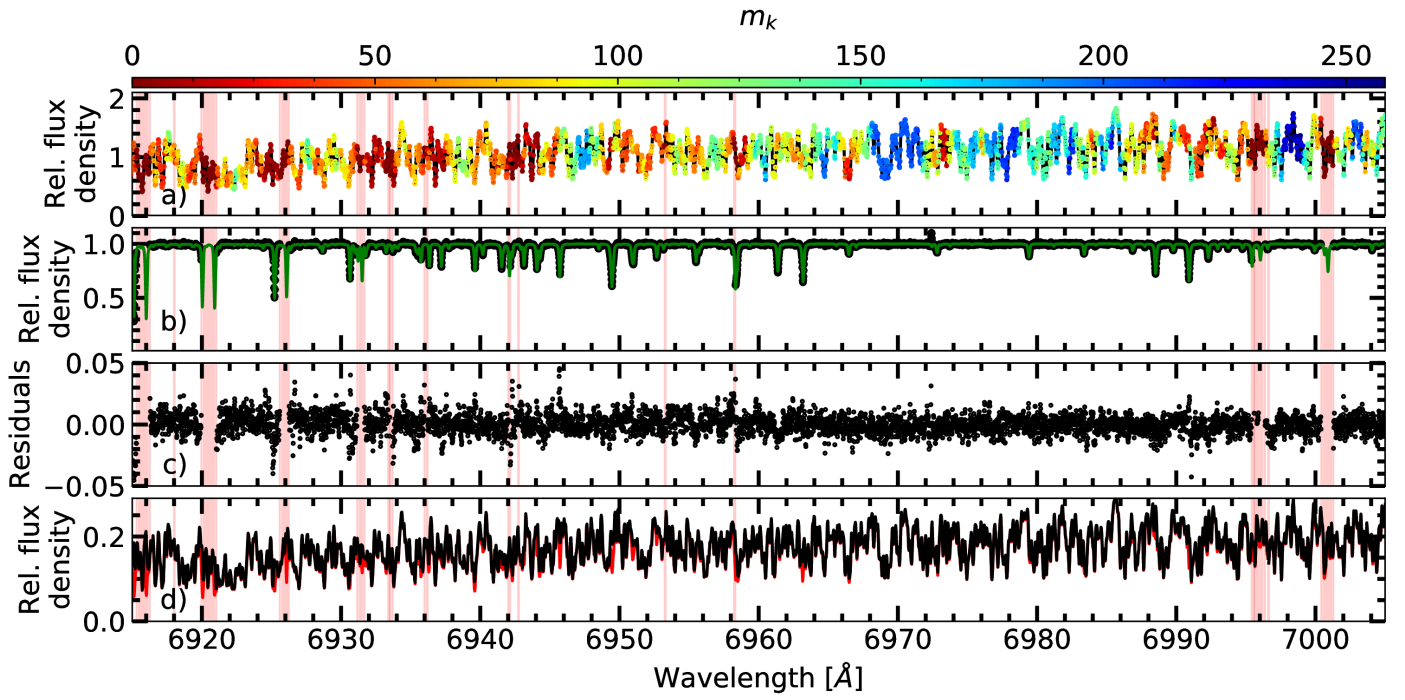


Fig. C.1. Same as Fig. 2 but for  $O_2$  and  $H_2O$  features.

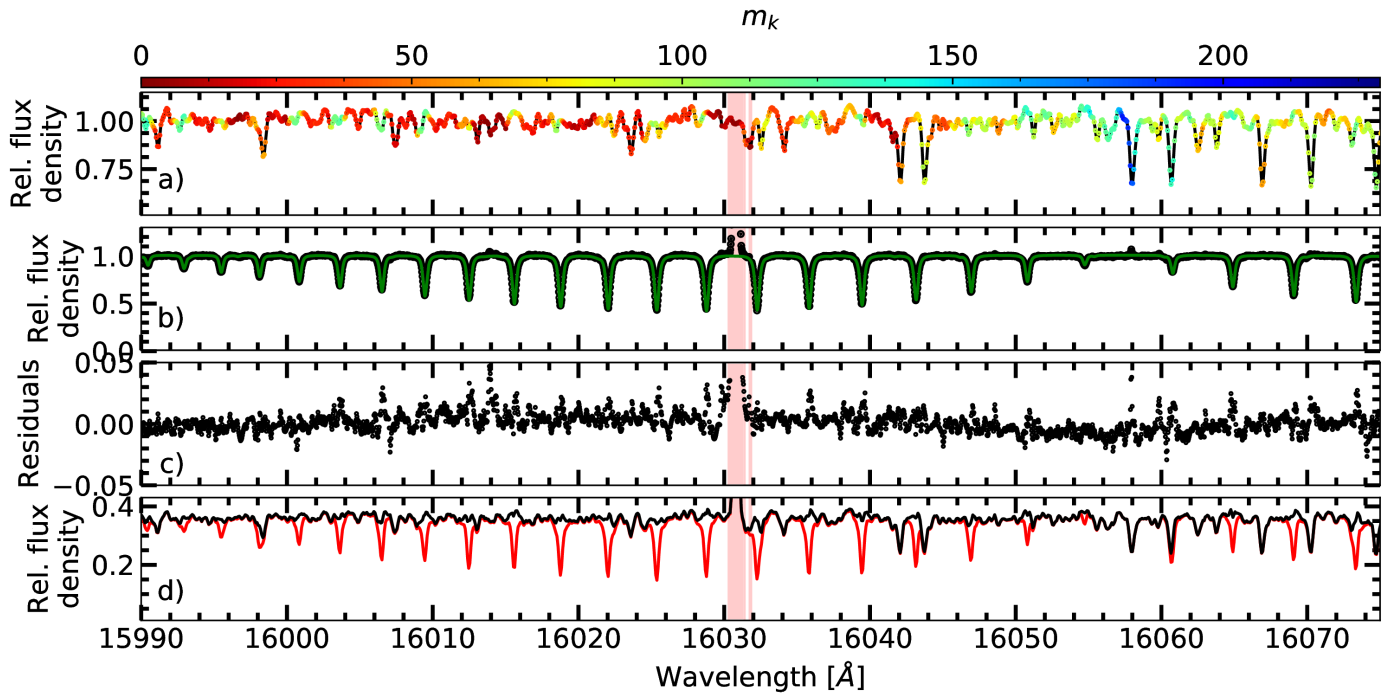


Fig. C.2. Same as Fig. 2 but for the NIR wavelength range, which contains telluric  $CO_2$  features. In addition to template pixels with  $m_k = 0$ , we also masked telluric emission features.

### **5.3 The enigmatic planetary system GJ 4276: one eccentric planet or two planets in a 2:1 resonance?**

**Authors:** E. Nagel, S. Czesla, J. H. M. M. Schmitt, S. Dreizler, G. Anglada-Escudé, E. Rodríguez, I. Ribas, A. Reiners, A. Quirrenbach, P. J. Amado, J. A. Caballero, J. Aceituno, V. J. S. Béjar, M. Cortés-Contreras, L. González-Cuesta, E. W. Guenther, T. Henning, S. V. Jeffers, A. Kaminski, M. Kürster, M. Lafarga, M. J. López-González, D. Montes, J. C. Morales, V. M. Passegger, C. Rodríguez-López, A. Schweitzer, and M. Zechmeister

**Published in *Astronomy & Astrophysics* 622, A153 (2019)**

Reproduced with permission ©ESO

# The CARMENES search for exoplanets around M dwarfs

## The enigmatic planetary system GJ 4276: one eccentric planet or two planets in a 2:1 resonance?★

E. Nagel<sup>1</sup>, S. Czesla<sup>1</sup>, J. H. M. M. Schmitt<sup>1</sup>, S. Dreizler<sup>2</sup>, G. Anglada-Escudé<sup>3,4</sup>, E. Rodríguez<sup>3</sup>,  
I. Ribas<sup>5,6</sup>, A. Reiners<sup>2</sup>, A. Quirrenbach<sup>7</sup>, P. J. Amado<sup>3</sup>, J. A. Caballero<sup>8</sup>, J. Aceituno<sup>3,9</sup>, V. J. S. Béjar<sup>10,11</sup>,  
M. Cortés-Contreras<sup>8</sup>, L. González-Cuesta<sup>10,11</sup>, E. W. Guenther<sup>12</sup>, T. Henning<sup>13</sup>, S. V. Jeffers<sup>2</sup>, A. Kaminski<sup>7</sup>,  
M. Kürster<sup>13</sup>, M. Lafarga<sup>5,6</sup>, M. J. López-González<sup>3</sup>, D. Montes<sup>14</sup>, J. C. Morales<sup>5,6</sup>, V. M. Passegger<sup>1</sup>,  
C. Rodríguez-López<sup>3</sup>, A. Schweitzer<sup>1</sup>, and M. Zechmeister<sup>2</sup>

<sup>1</sup> Hamburger Sternwarte, Gojenbergsweg 112, 21029 Hamburg, Germany  
e-mail: [evangelos.nagel@hs.uni-hamburg.de](mailto:evangelos.nagel@hs.uni-hamburg.de)

<sup>2</sup> Universität Göttingen, Institut für Astrophysik, Friedrich-Hund-Platz 1, 37077 Göttingen, Germany

<sup>3</sup> Instituto de Astrofísica de Andalucía (IAA-CSIC), Glorieta de la Astronomía s/n, 18008 Granada, Spain

<sup>4</sup> School of Physics and Astronomy, Queen Mary, University of London, 327 Mile End Road, London E1 4NS, UK

<sup>5</sup> Institut de Ciències de l'Espai (ICE, CSIC), Campus UAB, C/ de Can Magrans s/n, 08193 Cerdanyola del Vallès, Spain

<sup>6</sup> Institut d'Estudis Espacials de Catalunya (IEEC), C/ Gran Capità 2-4, 08034 Barcelona, Spain

<sup>7</sup> Landessternwarte, Zentrum für Astronomie der Universität Heidelberg, Königstuhl 12, 69117 Heidelberg, Germany

<sup>8</sup> Centro de Astrobiología (CSIC-INTA), ESAC, Camino Bajo del Castillo s/n, 28692 Villanueva de la Cañada, Madrid, Spain

<sup>9</sup> Centro Astronómico Hispano-Alemán (CSIC-MPG), Observatorio Astronómico de Calar Alto, Sierra de los Filabres, 04550 Gérgal, Almería, Spain

<sup>10</sup> Instituto de Astrofísica de Canarias, Vía Láctea s/n, 38205 La Laguna, Tenerife, Spain

<sup>11</sup> Departamento de Astrofísica, Universidad de La Laguna, 38206 La Laguna, Tenerife, Spain

<sup>12</sup> Thüringer Landessternwarte Tautenburg, Sternwarte 5, 07778 Tautenburg, Germany

<sup>13</sup> Max-Planck-Institut für Astronomie, Königstuhl 17, 69117 Heidelberg, Germany

<sup>14</sup> Departamento de Astrofísica y Ciencias de la Atmósfera, Facultad de Ciencias Físicas, Universidad Complutense de Madrid, 28040 Madrid, Spain

Received 3 November 2018 / Accepted 13 December 2018

### ABSTRACT

We report the detection of a Neptune-mass exoplanet around the M4.0 dwarf GJ 4276 (G 232-070) based on radial velocity (RV) observations obtained with the CARMENES spectrograph. The RV variations of GJ 4276 are best explained by the presence of a planetary companion that has a minimum mass of  $m_b \sin i \approx 16 M_\oplus$  on a  $P_b = 13.35$  day orbit. The analysis of the activity indicators and spectral diagnostics exclude stellar induced RV perturbations and prove the planetary interpretation of the RV signal. We show that a circular single-planet solution can be excluded by means of a likelihood ratio test. Instead, we find that the RV variations can be explained either by an eccentric orbit or interpreted as a pair of planets on circular orbits near a period ratio of 2:1. Although the eccentric single-planet solution is slightly preferred, our statistical analysis indicates that none of these two scenarios can be rejected with high confidence using the RV time series obtained so far. Based on the eccentric interpretation, we find that GJ 4276 b is the most eccentric ( $e_b = 0.37$ ) exoplanet around an M dwarf with such a short orbital period known today.

**Key words.** planetary systems – stars: individual: GJ 4276 – stars: low-mass – methods: data analysis – methods: observational – techniques: radial velocities

## 1. Introduction

M dwarfs constitute roughly 75% of the stellar population in the solar neighborhood (Henry et al. 2006). Compared to solar-like stars, they are smaller in mass, radius, and luminosity. These properties shift the focus of ongoing and future transit and radial velocity (RV) surveys toward M dwarfs for many reasons. Since the semi-amplitude of the reflex motion scales with stellar mass as  $M_\star^{-2/3}$  (e.g., Cumming et al. 1999) and the transit depth with

the stellar radius as  $R_\star^{-2}$  (e.g., Seager & Mallén-Ornelas 2003), they are most promising targets for exoplanet searches and, in particular, for finding Earth-like rocky planets. Of special interest are planets located in the habitable zone, in which water can exist on the planetary surface in a liquid phase. Due to the intrinsic faintness of M dwarfs, the distance of the habitable zone is much smaller for those stars. This leads to shorter orbital periods and larger transit probabilities. Early M dwarfs show a high planet occurrence rate of  $2.5 \pm 0.2$  planets with 1–4 Earth radii and orbital periods shorter than 200 days per star (Dressing & Charbonneau 2015), implying that these objects are numerous planet hosts in the Milky Way.

\* Photometric measurements and Table C.1 are available at the CDS via anonymous ftp to [cdsarc.u-strasbg.fr](http://cdsarc.u-strasbg.fr) (130.79.128.5) or via <http://cdsarc.u-strasbg.fr/viz-bin/qcat?J/A+A/622/A153>

The search for low-mass planets around a sample of about 300 M dwarfs (Reiners et al. 2018a) is the main scientific objective of the RV survey conducted by the CARMENES consortium (Quirrenbach et al. 2018). The CARMENES instrument has already proved its ability to reach an RV accuracy of  $\sim 1 \text{ m s}^{-1}$  and has enabled the discovery and characterization of several planetary systems (Trifonov et al. 2018; Reiners et al. 2018b; Sarkis et al. 2018; Kaminski et al. 2018; Luque et al. 2018; Ribas et al. 2018).

In this paper, we report the detection of a Neptune-mass object orbiting GJ 4276. In Sect. 2, we present the stellar characteristics of GJ 4276. The photometric data sets and the determination of the rotation period are described in Sect. 3. We performed a detailed analysis of the RV measurements and the stellar activity, and fit Keplerian models to the RV data, as described in Sect. 4. Finally, we summarize and discuss our findings in Sect. 5.

## 2. Host star properties

We summarize the main characteristics of our star in Table 1. GJ 4276 (G 232-070, Karm J22252+594) is an M4.0 dwarf (Reid et al. 1995; Lépine et al. 2013) at a distance of  $21.35 \pm 0.02 \text{ pc}$  (Gaia Collaboration 2018). Together with the parallax, we used the proper motion in right ascension and declination to calculate the secular acceleration ( $\dot{v}_{\text{rad}} = 0.048 \pm 0.002 \text{ m s}^{-1} \text{ yr}^{-1}$ ). The UVW Galactic space velocities imply that GJ 4276 belongs to the thin-disk stellar population (Cortés-Contreras 2016).

The basic photospheric parameters  $T_{\text{eff}}$ ,  $\log g$ , and [Fe/H] were measured as in Passegger et al. (2018), who fit the latest version of the PHOENIX-ACES models (Husser et al. 2013) to CARMENES spectra. We computed the luminosity from the Gaia DR2 parallax and multiwavelength photometry from *B* to *W4* as described in Kaminski et al. (2018) and Luque et al. (2018). Based on our  $T_{\text{eff}}$  and  $L$  determinations, we computed the stellar radius  $R$  by means of the Stefan-Boltzmann law, and finally derived the stellar mass  $M$  using a linear mass-radius relation. The details of the luminosity, radius, and mass determinations of the CARMENES targets will be presented by Cifuentes et al. (in prep.) and Schweitzer et al. (in prep.).

The star GJ 4276 is not a ROSAT All-Sky Survey (RASS) source and we estimated an upper limit for the X-ray luminosity of  $L_X \approx 8 \times 10^{27} \text{ erg s}^{-1}$  using the typical RASS detection limit of  $f_X \approx 2 \times 10^{-13} \text{ erg cm}^{-2} \text{ s}^{-1}$  (Schmitt et al. 1995) and, from it, an upper limit of  $L_X/L_{\text{bol}} < 10^{-4}$ . According to Reiners et al. (2018a), GJ 4276 is not an  $H\alpha$  emitter and has an  $2 \text{ km s}^{-1}$  upper limit on the projected rotational velocity  $v \sin i$ .

## 3. Photometry

To search for photometric modulation caused by rotating surface inhomogeneities such as dark spots and bright plages, we used archival time-series photometry from the MEarth-North project (Berta et al. 2012) and the ‘‘All-Sky Automated Survey for Supernovae’’ (ASAS-SN; Shappee et al. 2014). In addition, we obtained custom *V* band photometry with the T150 telescope located at the Sierra Nevada Observatory (SNO) in Spain and with two 40 cm telescopes of the Las Cumbres Observatory (LCO) located at the Haleakala Observatory on Hawai‘i and the Teide Observatory on the Canary Islands.

The MEarth-North telescope array is located at the Fred Lawrence Whipple Observatory, Arizona, and consists of eight 40 cm robotic telescopes. Each is equipped with a  $2048 \times 2048$

**Table 1.** Stellar parameters of GJ 4276.

| Parameter  | GJ 4276              | Ref. <sup>a</sup> |
|--|----------------------|-------------------|
| $\alpha$   | 22 25 17.32          | Gaia DR2          |
| $\delta$   | +59 24 45.01         | Gaia DR2          |
| SpT  | M4.0                 | Rei95, Lépin13    |
| $G$ (mag)  | $11.6605 \pm 0.0006$ | Gaia DR2          |
| $J$ (mag)  | $8.75 \pm 0.03$      | 2MASS             |
| $\pi$ (mas)                                      | $46.84 \pm 0.04$     | Gaia DR2          |
| $\mu_\alpha \cos \delta$ (mas yr <sup>-1</sup> ) | $122.37 \pm 0.07$    | Gaia DR2          |
| $\mu_\delta$ (mas yr <sup>-1</sup> )             | $-310.10 \pm 0.06$   | Gaia DR2          |
| $v_{\text{rad}}$ (km s <sup>-1</sup> )           | 4.034                | Rei18             |
| $U$ (km s <sup>-1</sup> )                        | $4.4 \pm 0.45$       | Cor16             |
| $V$ (km s <sup>-1</sup> )                        | $5.96 \pm 0.16$      | Cor16             |
| $W$ (km s <sup>-1</sup> )                        | $-28.46 \pm 1.17$    | Cor16             |
| $T_{\text{eff}}$ (K)                             | $3387 \pm 51$        | Sch18             |
| $\log g$ (dex)                                   | $4.97 \pm 0.07$      | Sch18             |
| [Fe/H] (dex)                                     | $0.12 \pm 0.16$      | Sch18             |
| $M$ ( $M_\odot$ )                                | $0.406 \pm 0.030$    | Sch18             |
| $L$ ( $L_\odot$ )                                | $0.0197 \pm 0.0003$  | Sch18             |
| $R$ ( $R_\odot$ )                                | $0.407 \pm 0.015$    | Sch18             |
| $v \sin i$ (km s <sup>-1</sup> )                 | <2                   | Rei18             |
| $P_{\text{rot}}$ (d)                             | $64.3 \pm 1.2$       | This work         |
| Age (Gyr)  | $6.9 \pm 1.1$        | This work         |

**References.** <sup>(a)</sup> Gaia DR2: Gaia Collaboration (2018); Rei95: Reid et al. (1995); Lépin13: Lépine et al. (2013); 2MASS: Skrutskie et al. (2006); Roe10: Roeser et al. (2010); Rei18: Reiners et al. (2018a); Cor16: Cortés-Contreras (2016); Sch18: Schweitzer et al. (in prep.).

CCD with a pixel scale of  $0.76''$  and a custom 715 nm long-pass filter. While the main objective of the MEarth project is the search for low-mass rocky exoplanets around M dwarfs in the habitable zone with the transit method, ASAS-SN is dedicated to the discovery of nearby supernovae by monitoring the entire visible sky down to  $\sim 17 \text{ mag}$  in the *V* band. It comprises five units with a total of 20 telescopes situated in Chile, Hawai‘i, South Africa, and Texas. Each of the 14 cm telephoto lenses has a  $2\text{k} \times 2\text{k}$  CCD with a field of view of  $4.5 \times 4.5 \text{ deg}$  and a pixel scale of  $7.8''$ . The T150 telescope at the SNO is a 150 cm Ritchie-Chétien telescope. It is equipped with a  $2\text{k} \times 2\text{k}$  VersArray CCD camera with a field of view of  $7.9 \times 7.9 \text{ arcmin}$  (Rodríguez et al. 2010). The LCO telescopes are equipped with a  $3\text{k} \times 2\text{k}$  SBIG CCD camera with a pixel scale of  $0.571''$  providing a field of view of  $29.2 \times 19.5 \text{ arcmin}$ .

The photometric measurements used in this study cover a time span of four years of MEarth data (October 2011–November 2015), three years of ASAS-SN data (December 2014–December 2017), four months of SNO data (May–September 2018), and three months of LCO data (June–September 2018). Exposure times of ten minutes for MEarth and ASAS-SN, 50 seconds for SNO, and 150 seconds for LCO result in median uncertainties of  $\bar{\sigma}_{\text{MEarth}} = 4 \text{ mmag}$ ,  $\bar{\sigma}_{\text{ASAS-SN}} = 15 \text{ mmag}$ ,  $\bar{\sigma}_{\text{SNO}} = 2.9 \text{ mmag}$ , and  $\bar{\sigma}_{\text{LCO}} = 3.2 \text{ mmag}$ .

To identify potentially spot induced periodic variability, we applied the generalized Lomb-Scargle (GLS) periodogram (Zechmeister & Kürster 2009) to the MEarth, ASAS-SN, and SNO data sets of GJ 4276. The periodograms show evidence for periodicity at  $P_{\text{MEarth}} = 63.9^{+1.7}_{-1.6} \text{ d}$ ,  $P_{\text{ASAS-SN}} = 64.7^{+1.6}_{-1.5} \text{ d}$ , and  $P_{\text{SNO}} = 32.3^{+4.3}_{-3.4} \text{ d}$ . To estimate the uncertainties of our period determination, we fit a Gaussian profile to the peak with the largest power and computed its full-width-half-maximum (FWHM).

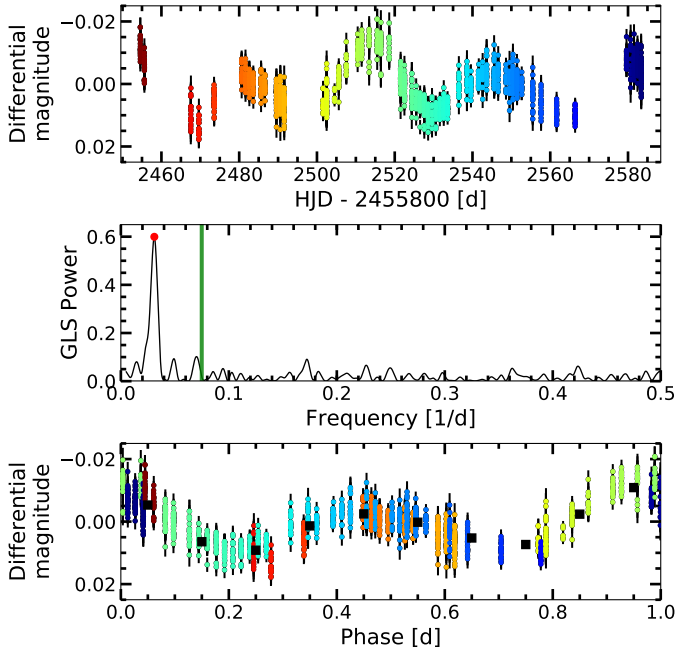


**Fig. 1.** Rotation period analysis using SNO photometric data. *Top panel:* V band light curve. The color of the datapoints indicates the observation epoch. *Middle panel:* GLS periodogram. The vertical green line represents the orbital period of the planet at 13.35 days and the red dot the peak with the highest power at 32.3 days. *Bottom panel:* phased light curve using twice the period derived from the GLS. The black squares indicate the mean magnitude in ten equidistant bins in phase.

We present the light curve, the periodogram, and the phase folded light curve derived from the SNO data in Fig. 1. The light curves and periodograms of the M<sub>Earth</sub> and ASAS-SN data sets are shown in Fig. A.1. Visual inspection of the SNO light curve (top panel of Fig. 1) shows a clear variability pattern, which remained rather stable during the observation run. The pattern is well resolved and consists of two bumps with alternating amplitude, which we interpret as the photometric manifestation of two starspots located on opposing hemispheres. Therefore, we conclude that the GLS peak at 32.3 days is the semi-period of the stellar rotation period of  $\approx 64.6$  d, which also resolves the apparent conflict with the M<sub>Earth</sub> and ASAS-SN data. The phase-folded light curves of the latter show a less pronounced signal, which may be related to the longer span covered. We find consistent results with the LCO data.

The rotation period obtained here is consistent with the findings of Díez Alonso et al. (2019), who reported a value of  $64.6 \pm 2.1$  d with a FAP level of  $<10^{-4}\%$  for GJ 4276 based on their analysis of the ASAS-SN light curve alone. Also, a rotation period of roughly 64 days is consistent with the low activity level observed in GJ 4276 and the absence of H $\alpha$  emission. Based on gyrochronological models by Barnes (2007), we calculated an age of  $6.9 \pm 1.1$  Gyr using the intrinsic  $B-V$  color and the derived rotation period as input parameters.

## 4. Spectroscopy

We gathered exactly 100 CARMENES RV measurements of GJ 4276 over a time span of 774 days. The observations were carried out as part of the CARMENES GTO survey (Reiners et al. 2018a) between July 2016 and August 2018 with the CARMENES echelle spectrograph (Quirrenbach et al. 2018), mounted on the 3.5 m telescope of the Calar Alto Observatory in

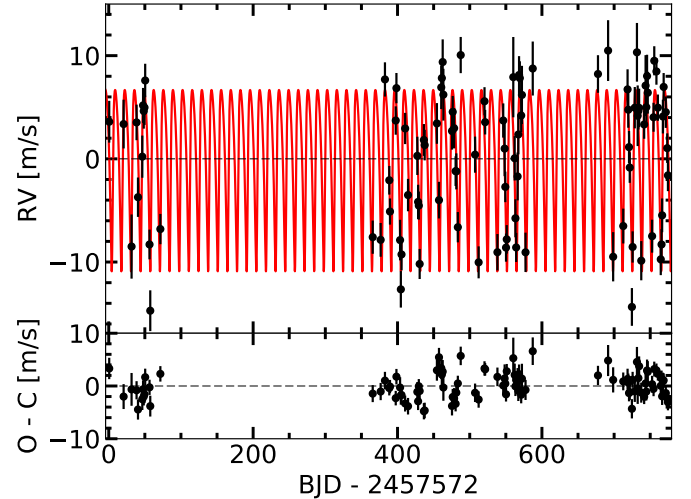


**Fig. 2.** *Top panel:* radial velocity measurements of GJ 4276 obtained with CARMENES as a function of barycentric Julian Date. The best-fit eccentric single-planet Keplerian model is overlotted in red (see Sect. 4.2). *Bottom panel:* O–C residuals.

Spain. CARMENES consists of a pair of high resolution spectrographs, which cover the optical wavelength range from 5200 Å to 9600 Å with a resolution power of  $R = 94\,600$ , and the near-infrared range from 9600 Å to 17 100 Å with  $R = 80\,400$ . Both channels are enclosed in temperature- and pressure-stabilized vacuum vessels to reduce instrumental drifts and to provide a RV precision on a  $\text{m s}^{-1}$  level.

The CARMENES survey observation strategy aims at reaching a signal-to-noise ratio of 150 in the  $J$  band. The typical exposure time of our spectra of GJ 4276 is 1800 s. The raw frames were extracted using the CARACAL reduction pipeline (Caballero et al. 2016), which is based on flat-relative optimal extraction (Zechmeister et al. 2014). The wavelength calibration is based on three hollow cathode lamps (U-Ne, U-Ar, and Th-Ne) combined with a Fabry-Pérot etalon (Bauer et al. 2015; Schäfer et al. 2018). The reference frames were taken at the beginning of each observing night. In addition, Fabry-Pérot etalon spectra were taken simultaneously with the target to track and correct the nightly instrument drift.

To precisely measure the Doppler shifts on a  $\text{m s}^{-1}$  level, we used the SERVAL<sup>1</sup> code (Zechmeister et al. 2018), which constructs a high signal-to-noise template spectrum by coadding all spectra of GJ 4276 after correcting for barycentric motion (Wright & Eastman 2014) and secular acceleration (Zechmeister et al. 2009). To consider systematic instrumental effects, we further corrected the RVs for nightly zero-point variations using RV measurements of stars with low RV variability observed in the same night; we refer to Trifonov et al. (2018) for a detailed description.

In this study, we employed RVs only from the VIS channel, which have an internal median uncertainty of  $1.7 \text{ m s}^{-1}$ . We present the RV measurements used in this paper in Fig. 2 and list them along with their formal uncertainties in Table C.1.

### 4.1. Periodogram analysis

To study the RV variability of GJ 4276, we applied the GLS periodogram to the measurements obtained with CARMENES. The resulting periodogram is shown in Fig. 3. Following Eq. (24)

<sup>1</sup> SpEctrum Radial Velocity AnaLyser, <https://github.com/mzechmeister/serval>

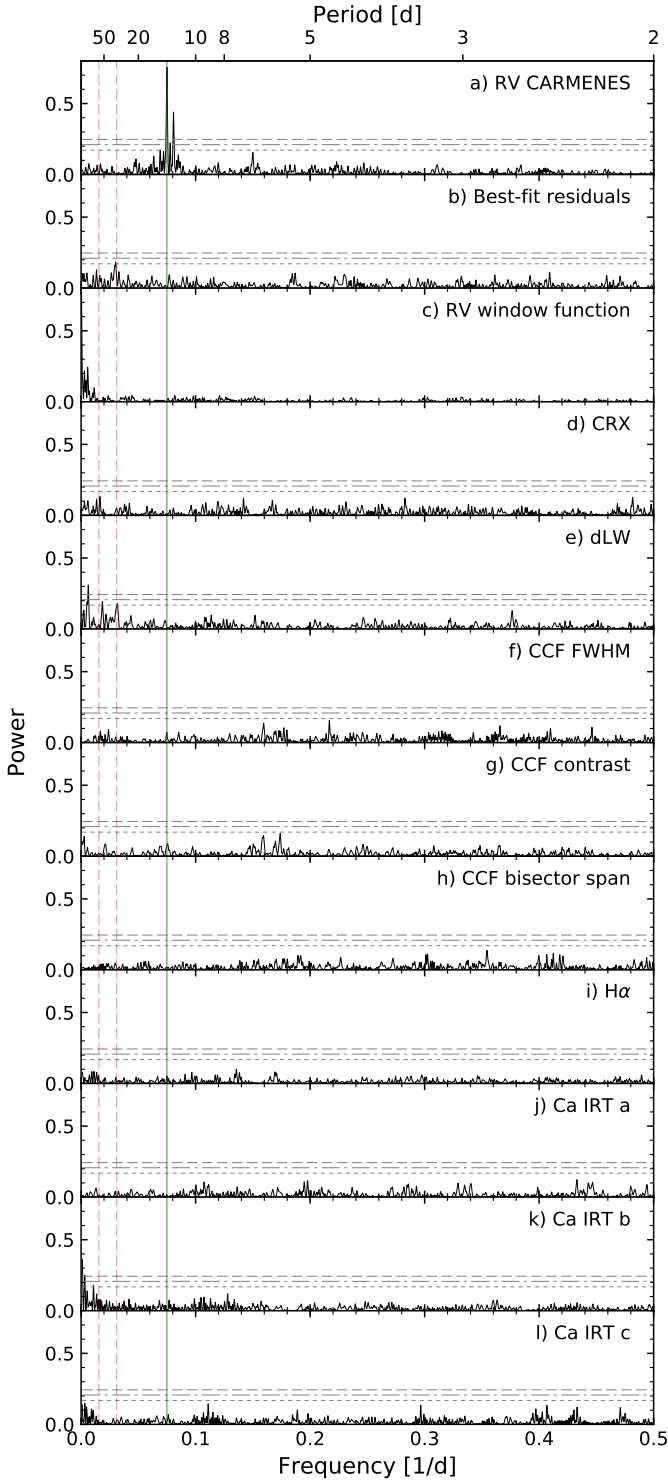


**Fig. 3.** GLS periodograms of GJ 4276. *Panel a:* periodogram of the CARMENES RVs. The horizontal lines (dotted, dash-dotted, dashed) indicate FAP levels of 10%, 1%, and 0.1%. The vertical green line marks the orbital period with the highest power at 13.347 d. The left red dashed line at  $P_{\text{rot}} = 64.3$  d ( $f_{\text{rot}} = 0.0156$  d $^{-1}$ ) shows the weighted mean of the photometrically derived stellar rotation period and the right red dashed line its first harmonic ( $2f_{\text{rot}} = 0.0311$  d $^{-1}$ ). *Panel b:* periodogram of the residuals after removing the best-fit single-planet Keplerian with eccentricity (see Sect. 4.2.2) signal; *panel c:* window function of the RV data. *Panels d–h:* periodograms of the chromatic RV index (CRX), differential line width (dLW), as well as FWHM, contrast, and bisector span from the CCF analysis. *Panels i–l:* periodograms of the chromospheric line indices of  $H\alpha$  and Ca II IRT.

from Zechmeister & Kürster (2009), we computed the false alarm probabilities (FAPs) to evaluate the significance of the peaks in the power spectra.

The largest power excess with a FAP well below 0.1% appears at a frequency of  $f = 0.07493$  d $^{-1}$  (13.347 days, Fig. 3a). To check the persistence of this signal, we divided the entire data set into three RV subsamples and separately analyzed their periodograms. In all cases we find similar peaks, corresponding to frequencies of  $f_1 = 0.07480$  d $^{-1}$  (13.370 days),  $f_2 = 0.07438$  d $^{-1}$  (13.444 days), and  $f_3 = 0.07581$  d $^{-1}$  (13.192 days), indicating that the signal is, indeed, persistent. Furthermore, a power peak of the first harmonic of the dominant signal at  $f = 0.14986$  d $^{-1}$  (6.673 days) is visible in the periodogram.

We identify further strong signals with FAPs < 0.1% at frequencies of  $0.92784$  d $^{-1}$  and  $1.07766$  d $^{-1}$  with powers of 0.51 and 0.58, respectively (outside the frequency range shown in Fig. 3 for the sake of clarity). Both peaks are plausible one-day aliases of the primary period ( $\sim 1.000 \pm 0.075$  d $^{-1}$ ) which disappear after we subtract the best-fit eccentric single-planet Keplerian model (see Sect. 4.2.2) from the RV measurements.

To ensure that the RV variation is not caused by stellar activity, we made use of several spectral diagnostics provided by SERVAL, viz., chromospheric indices, the differential line width, the chromatic index, and the cross-correlation function. The chromatic index (CRX), as introduced by Zechmeister et al. (2018), describes the color-dependence of the RV signal, which must vanish for a planetary signal but not for a spot-induced signal. Rotating spots induce periodic line profile variations, which were scrutinized using the differential line width (dLW) indicator. We also analyzed the cross-correlation function (CCF) of each spectrum. Specifically, we checked for periodic modulation of the FWHM, contrast, and bisector span as described in Reiners et al. (2018b). Any such detection would, again, be a red flag indicating activity-induced modulation. Finally, the  $H\alpha$  and Ca II IRT line indices were analyzed, which directly trace chromospheric activity.

We present GLS periodograms of all these spectral diagnostic time series in Fig. 3. Beside the periodogram of the dLW and Ca II IRT b line indices at  $8542$  Å, none of the investigated indicators exhibit significant peaks above the 10% FAP level. The periodogram of the dLW shows a marginally significant power peak at the first harmonic of the stellar rotation period around 32 days, which is most likely caused by rotational modulation of active regions. In addition, the dLW shows two peaks at 54 and 161 days with formal FAP levels above 10% and 0.1%, respectively. Also, some long-term periodic pattern can be seen in the periodogram of the Ca II IRT b line index but no peaks were found in the periodograms of the Ca II IRT a and c line indices at  $8498$  Å and  $8662$  Å at similar frequencies. Importantly, however, the RV signal at 13.347 days correlates neither with the spurious signals produced by the dLW and the Ca II IRT b line indices nor with any signal produced by other spectral activity indicators. Thus, we are confident that this persistent signal is not related to activity, but is most probably of planetary origin.

#### 4.2. Orbital solutions

Having established the planetary origin of the RV signal, we now determine the orbital elements of the planet. To that end, we implemented a Keplerian RV curve model and carry out parameter optimization using a Nelder-Mead simplex algorithm (Nelder & Mead 1965). Following the approach of Baluè (2009), our model incorporates an RV jitter variance term to

**Table 2.** Best-fit orbital parameters for the GJ 4276 system.

| Orbital parameters                            | GJ 4276 b <sup>a</sup>                     | GJ 4276 b <sup>b</sup>                     | GJ 4276 b <sup>c</sup>                     | GJ 4276 c <sup>c</sup>                    |
|---|--|--|--|---|
| $K$ (m s <sup>-1</sup> )                      | 7.93 <sup>+0.32</sup> <sub>-0.32</sub>     | 8.79 <sup>+0.27</sup> <sub>-0.27</sub>     | 7.67 <sup>+0.25</sup> <sub>-0.25</sub>     | 2.73 <sup>+0.23</sup> <sub>-0.24</sub>    |
| $P$ (d)                                       | 13.348 <sup>+0.005</sup> <sub>-0.005</sub> | 13.352 <sup>+0.003</sup> <sub>-0.003</sub> | 13.350 <sup>+0.004</sup> <sub>-0.004</sub> | 6.675 <sup>+0.002</sup> <sub>-0.002</sub> |
| $e$   | 0 (fixed)                                  | 0.37 <sup>+0.03</sup> <sub>-0.03</sub>     | 0 (fixed)                                  | 0 (fixed)                                 |
| $\omega$ (deg)                                | 90 (fixed)                                 | 216.83 <sup>+4.74</sup> <sub>-4.56</sub>   | 90 (fixed)                                 | 90 (fixed)                                |
| $\tau$ (BJD -2457572)                         | 0.28 <sup>+0.23</sup> <sub>-0.22</sub>     | 4.72 <sup>+0.19</sup> <sub>-0.17</sub>     | 0.10 <sup>+0.17</sup> <sub>-0.17</sub>     | 2.35 <sup>+0.18</sup> <sub>-0.18</sub>    |
| $\gamma$ (m s <sup>-1</sup> )                 | 0.31 <sup>+0.24</sup> <sub>-0.23</sub>     | 0.52 <sup>+0.18</sup> <sub>-0.18</sub>     | 0.39 <sup>+0.18</sup> <sub>-0.17</sub>     |   |
| $\sigma_{\text{jitter}}$ (m s <sup>-1</sup> ) | 2.83 <sup>+0.22</sup> <sub>-0.20</sub>     | 1.74 <sup>+0.18</sup> <sub>-0.17</sub>     | 1.89 <sup>+0.18</sup> <sub>-0.17</sub>     |   |
| $a$ (au)                                      | 0.082 <sup>+0.002</sup> <sub>-0.002</sub>  | 0.082 <sup>+0.002</sup> <sub>-0.002</sub>  | 0.082 <sup>+0.002</sup> <sub>-0.002</sub>  | 0.051 <sup>+0.001</sup> <sub>-0.001</sub> |
| $m_{\text{p}} \sin i$ ( $M_{\oplus}$ )        | 16.11 <sup>+1.03</sup> <sub>-1.01</sub>    | 16.57 <sup>+0.94</sup> <sub>-0.95</sub>    | 15.58 <sup>+0.93</sup> <sub>-0.90</sub>    | 4.40 <sup>+0.44</sup> <sub>-0.44</sub>    |
| $\sigma_{\text{O-C}}$ (m s <sup>-1</sup> )    | 3.29                                       | 2.46                                       | 2.57                                       |   |
| $-2 \ln \mathcal{L}$                          | 229.71                                     | 170.48                                     | 179.77                                     |   |

**Notes.** <sup>(a)</sup>Circular single-planet Keplerian model, <sup>(b)</sup>eccentric single-planet Keplerian model, <sup>(c)</sup>two-planet Keplerian model on circular orbits with period ratio of 2:1.

account for additional stochastic scatter; the jitter parameter is fit simultaneously during the parameter optimization.

In the following, we juxtapose three Keplerian models and their performance in describing the observations, in particular, a single planet with a circular orbit, a single planet with an eccentric orbit, and two planets with circular orbits with a period ratio of 2:1. In addition to the periodic planetary signal, we allow for an RV offset to account for entire system's velocity. In a first run, we further fit a linear time evolution parameter to derive potential systematic acceleration and gauged with a likelihood ratio test whether the improvement is sufficient to include a slope. Although this additional fitting parameter resulted in a higher likelihood, we find that the improvement is non-significant.

The entire set of the derived best-fit Keplerian orbital elements is displayed in Table 2. The  $1\sigma$  uncertainties of the orbital parameters are estimated from the posterior distributions using the Markov Chain Monte Carlo sampler emcee (Foreman-Mackey et al. 2013) along with our Keplerian models (Figs. B.1–B.3). For the fit parameters we assumed uniform priors, except for the stellar mass, for which we imposed a Gaussian prior with mean and variance equal to  $0.406 \pm 0.030 M_{\odot}$  based on the mass determination of GJ 4276 (Sect. 2).

#### 4.2.1. Single planet on circular orbit

In the first model, we fit the RV measurements with a single planet on a circular orbit. We left the semi-amplitude  $K_{\text{b}}$ , the orbital period  $P_{\text{b}}$ , the RV jitter  $\sigma_{\text{jitter}}$ , as well as the RV offset  $\gamma$  as free parameters. The eccentricity remained fixed to  $e_{\text{b}} = 0$ . Further, we also fixed the argument of the periapsis to  $\omega_{\text{b}} = 90$  deg and fit the time of the periastron passage  $\tau_{\text{b}}$ .

This model converges on a period of  $P_{\text{b}} = 13.348$  days, matching the frequency of the power peak found in the periodogram. Following a Keplerian interpretation of the RV variations, GJ 4276 b is a Neptune-like planet with a minimum mass of  $m_{\text{b}} \sin i = 16.11 M_{\oplus}$ . Orbiting at a distance of 0.082 au from its host star, it is placed closer than the inner edge of the conservative and optimistic habitable zones, which range from 0.146 to 0.284 au and 0.115 to 0.299 au, respectively (Kopparapu et al. 2013, 2014). The solution further yields a semi-amplitude of  $K_{\text{b}} = 7.93 \text{ m s}^{-1}$  and a jitter term of  $\sigma_{\text{jitter}} = 2.83 \text{ m s}^{-1}$ . With respect to the model, the data yield a root mean square (rms) value of  $\sigma_{\text{O-C}} = 3.29 \text{ m s}^{-1}$ .

#### 4.2.2. Single planet with eccentric orbit

In addition to the parameters from the circular solution, we here let the eccentricity  $e$  and the argument of the periapsis  $\omega_{\text{b}}$  vary freely. While the best-fit minimum mass, the orbital period, semi-amplitude, and semi-major axis are comparable to that of the single-planet circular solution ( $m_{\text{b}} \sin i = 16.57 M_{\oplus}$ ,  $P_{\text{b}} = 13.352$  d,  $K_{\text{b}} = 8.79 \text{ m s}^{-1}$ ,  $a_{\text{b}} = 0.082$  au), the jitter term of  $\sigma_{\text{jitter}} = 1.74 \text{ m s}^{-1}$  found here is  $1.09 \text{ m s}^{-1}$  smaller than that previously obtained. The introduction of the eccentricity  $e_{\text{b}} = 0.37$  significantly improves the fit and results in an rms of  $\sigma_{\text{O-C}} = 2.46 \text{ m s}^{-1}$ . We show the phased RV data and the best-fit Keplerian one-planet solution in Fig. 4.

#### 4.2.3. Two planets on circular orbits with period ratio of 2:1

The single-planet model with an eccentric orbit results in a remarkably eccentric orbit with  $e = 0.37$ . Since the Doppler signal of a two-planet system on circular orbits near a 2:1 mean motion resonance can be misinterpreted as an eccentric single-planet (Anglada-Escudé et al. 2010; Wittenmyer et al. 2013; Kürster et al. 2015; Boisvert et al. 2018), we further tried to fit a two-planet model with circular orbits and fixed period ratio of 2:1, i.e.,  $P_{\text{b}} = 2P_{\text{c}}$ . In the modeling, we leave  $K_{\text{b}}$ ,  $K_{\text{c}}$ ,  $P_{\text{b}}$ ,  $\tau_{\text{b}}$ ,  $\tau_{\text{c}}$ ,  $\gamma$ , and  $\sigma_{\text{jitter}}$  free to vary (whereas  $\omega_{\text{b}} = \omega_{\text{c}} = 90$  deg).

Based on this double Keplerian model, we obtained orbital parameters for GJ 4276 b:  $K_{\text{b}} = 7.67 \text{ m s}^{-1}$ ,  $P_{\text{b}} = 13.350$  days, and for GJ 4276 c:  $K_{\text{c}} = 2.73 \text{ m s}^{-1}$ ,  $P_{\text{c}} = 6.675$  days, which translates into minimum planetary masses of  $m_{\text{b}} \sin i = 15.58 M_{\oplus}$  and  $m_{\text{c}} \sin i = 4.40 M_{\oplus}$  and semi-major axes of  $a_{\text{b}} = 0.082$  au and  $a_{\text{c}} = 0.051$  au.

#### 4.3. Likelihood analysis

To compare the fit qualities between the eccentric single-planet model and the two-planet model compared to the circular single-planet model, we carried out likelihood ratio tests (e.g., Wilks 1938; Protassov et al. 2002). In our circular single-planet model we have five free parameters, while there are seven in both the single-planet model with elliptical orbit and our two-planet model. The test statistic is  $-2\Delta \ln \mathcal{L}$ . According to Wilk's theorem (Wilks 1938), the probability distribution of the test statistic can be approximated by a  $\chi^2$  distribution with  $df$  degrees of freedom for large data samples. However, as discussed by



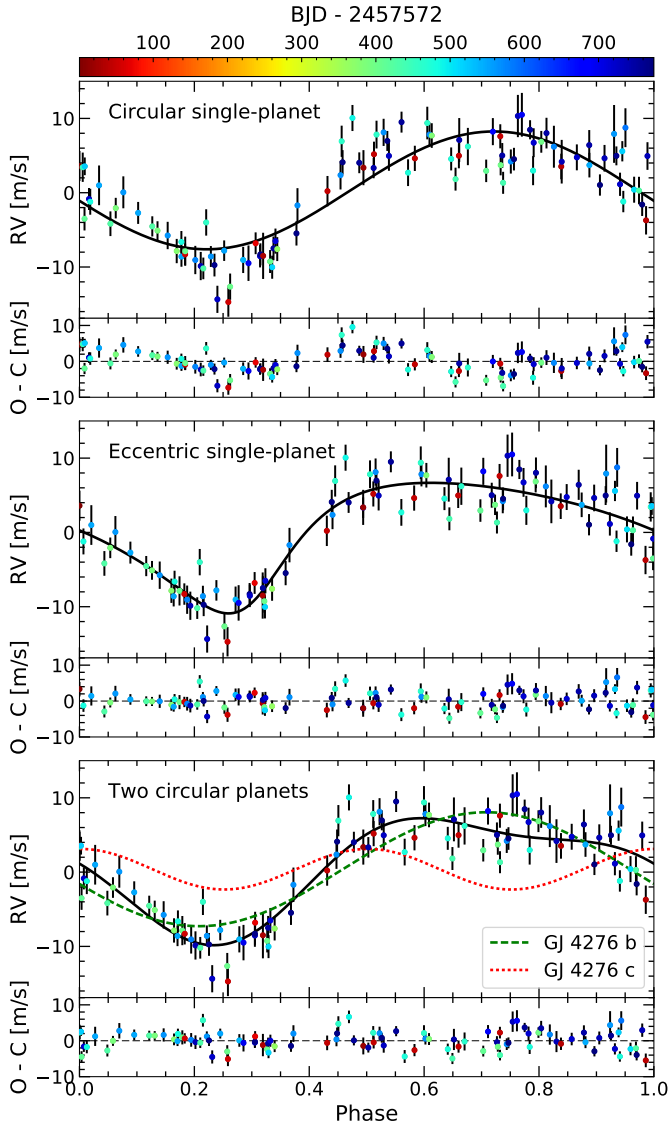


**Fig. 4.** Phase-folded radial velocity measurements of GJ 4276, together with the best-fit Keplerian model (black line) overplotted. In the bottom of each panel we show the O–C residuals. *Top panel:* circular single-planet Keplerian model. *Middle panel:* eccentric single-planet Keplerian model. *Bottom panel:* two-planet Keplerian model on circular orbits with a period ratio of 2:1. In addition, we show the best-fit Keplerian model of GJ 4276 b (green dashed line) and GJ 4276 c (red dotted line).

Protassov et al. (2002), Baluev (2009), and Czesla & Schmitt (2010), the formal criteria for this approximation are not fulfilled in the current case. While the models are nested as required, the circular single-planet model is only obtained from our elliptical or two-planet models by choosing parameters at the edge of the parameter space such as zero eccentricity.

Therefore, we verified that the probability distribution of the test statistic can, indeed, be approximated by a  $\chi^2$  distribution with two degrees of freedom:

$$df = df_{\text{alternative}} - df_{\text{null}} = 8 - 6 = 2. \quad (1)$$

Based on the best-fit circular single-planet solution, we generated 1000 synthetic data sets with random normally distributed errors that include the measurement error and the maximum-likelihood estimate of the stellar jitter so that  $\sigma_i^2 = \sigma_{\text{meas},i}^2 + \sigma_{\text{jitter}}^2$ . We fit these mock data sets using the circular single-planet model, as well as the eccentric single-planet and two-planet

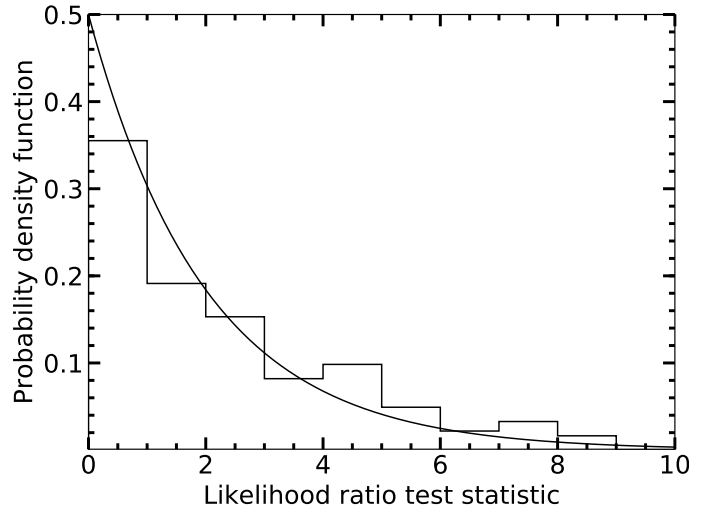


**Fig. 5.** Empirical distribution of the  $-2\Delta \ln \mathcal{L}$  statistic (histogram) along with the probability density of the  $\chi^2$  distribution with two degrees of freedom (black curve).

models. Based on the maxima of the respective likelihood functions, we calculated the test statistic  $-2\Delta \ln \mathcal{L}$ . As an example, we show the simulated distribution of the likelihood ratio test statistic, as well as the  $\chi^2$  distribution, for the comparison of the circular single-planet model and the eccentric single-planet model in Fig. 5. Based on our simulations, we conclude that the  $\chi^2$  distribution yields an acceptable approximation to the distribution of the test statistic in our case.

To assess the fit quality of the eccentric single-planet model compared to the circular single-planet model, we computed the ratio of the best-fit likelihoods for the circular model  $\ln \mathcal{L}_{1\text{cp}}$  and eccentric model  $\ln \mathcal{L}_{1\text{ep}}$  and found a value of  $\ln \mathcal{L}_{1\text{ep}} - \ln \mathcal{L}_{1\text{cp}} = 29.62$ . The probability to obtain such an improvement by chance if the true orbit were circular is only  $1.4 \times 10^{-13}$ . The comparison between the circular single-planet scenario and the two-planet model results in a likelihood ratio of  $\ln \mathcal{L}_{2\text{cp}} - \ln \mathcal{L}_{1\text{cp}} = 24.97$ , where  $\ln \mathcal{L}_{2\text{cp}}$  is the best-fit likelihood of the circular two-planet model. Again, we find a probability of only  $1.4 \times 10^{-11}$  that such an improvement in fit quality can be achieved by chance. We therefore conclude that the circular single-planet solution can be rejected with high confidence.

To study whether the eccentric single-planet model or the circular two-planet model is statistically preferred, we carried out another simulation. In particular, we generated 1000 artificial data sets by adding normally distributed random noise to the maximum-likelihood eccentric single-planet model on the one hand and the two-planet model on the other hand. To determine what differences in likelihood can be expected, we fit all of these artificial RV curves using both the eccentric single-planet and the two-planet model and calculated the likelihood ratios  $\ln \mathcal{L}_{2\text{cp}} - \ln \mathcal{L}_{1\text{ep}}$  and  $\ln \mathcal{L}_{1\text{ep}} - \ln \mathcal{L}_{2\text{cp}}$ , respectively. In Fig. 6 we show the resulting histograms of the likelihood ratios. We find a median value of  $-5.02$  assuming that the eccentric model is true and  $-3.54$  for the two-planet case. In addition, we indicate the measured likelihood ratio of  $\ln \mathcal{L}_{2\text{cp}} - \ln \mathcal{L}_{1\text{ep}} = -4.65$ . Based on the higher likelihood achieved in the fit, we find a slight preference for the eccentric single-planet solution. However, our findings show that the measured difference in likelihood does not allow to reject one or the other solution with reasonable confidence.

One possible strategy to discriminate between the two degenerated models is to increase the number of RV measurements, as

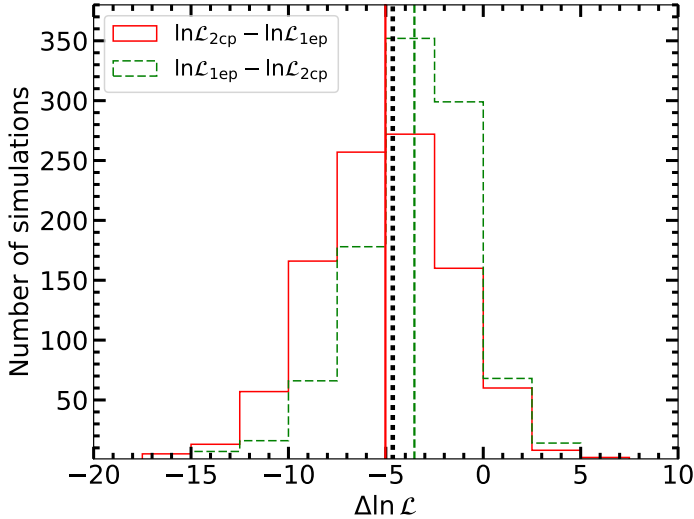


**Fig. 6.** Histograms of the likelihood ratio using simulated data sets based on the best-fit eccentric single-planet model (solid red) and the circular two-planet model (dashed green). The vertical solid red line and the dashed green line represent the median values of the histograms. The black dotted vertical line represents the measured likelihood ratio  $\ln \mathcal{L}_{2cp} - \ln \mathcal{L}_{1ep} = -4.65$ .

suggested by [Anglada-Escudé et al. \(2010\)](#), [Kürster et al. \(2015\)](#), and [Boisvert et al. \(2018\)](#). Ideally, the observations should be carried out at phases of maximal differences between the models. In the case of GJ 4276 b, we find a maximal difference of  $2.10 \text{ m s}^{-1}$ , which lies above the internal median error of  $1.7 \text{ m s}^{-1}$ . However, even for a quiet star like GJ 4276, we found an activity-induced RV jitter level in the range of  $1.5\text{--}3 \text{ m s}^{-1}$  limiting the achievable RV accuracy. To provide a rough estimate on the amount of additional RV observations that are necessary to distinguish between the two solutions, we generated synthetic RV measurements based on the best-fit eccentric model and fit them with the eccentric and the two-planet Keplerian model. Our results imply that  $\sim 100$  additional measurements randomly distributed in phase would be sufficient to push the likelihood ratio to  $\ln \mathcal{L}_{2cp} - \ln \mathcal{L}_{1ep} \approx -15$ .

#### 4.4. Orbital evolution of the eccentric single-planet solution

We employed an estimate of the tidal circularization timescale for the eccentric one-planet solution in order to assess its plausibility compared to the two-planet solution. Following [Jackson et al. \(2008\)](#), we solved the coupled differential equation for the evolution of the semi major axis and eccentricity due to tidal interaction. The two parameters determining this evolution are the modified tidal dissipation values  $Q$ . Here we adopted  $Q_{\star} = 10^5$  for the star. For the planet we used  $Q_p = 100$  for a possible rocky planet and  $Q_p = 10^5$  for a Neptune-like planet. Due to the significantly higher dissipation, a rocky planet's orbit would completely circularize within  $10^8 \text{ yr}$ , while a Neptune-like planet would maintain a high eccentricity over more than 10 Gyr. The unknown planetary interior therefore does not allow to provide an additional constraint to distinguish between the two configurations.

#### 4.5. Search for additional planetary companions

To check whether the RV data yield evidence for additional planets, we removed the best-fit single-planet eccentric model and the circular two-planet model from the RV data and investigated

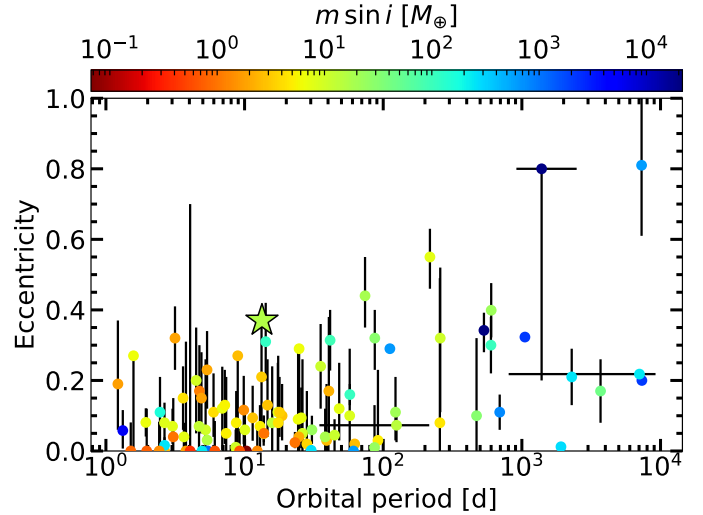


**Fig. 7.** Eccentricity plotted against orbital period of known exoplanets around M dwarfs (dots). The colors indicate the minimum mass and the star marks the position of GJ 4276 b with the eccentric single-planet solution.

the GLS periodograms of the RV residuals. Both periodograms show power excess at 32 days on a 10% FAP level, reflecting half of the stellar rotation period (see Fig. 3b). In addition to that, the periodograms of the RV residuals did not reveal any further significant power peaks attributable to planetary companions.

## 5. Summary and discussion

In this study, we analyzed 100 RV measurements of the M4.0V star GJ 4276, taken with the visible channel of the high-resolution CARMENES echelle spectrograph. The rotation period of 64 days determined from long-term photometry (MEarth, ASAS-SN) and the photometric campaign carried out during the present work (SNO, LCO), together with the lack of H $\alpha$  emission, implies that GJ 4276 is a weakly active and slowly rotating star. The examination of the spectral diagnostics and the activity indicators revealed no link between stellar activity and the supposed planetary signal supporting the fact that the RV variation at this period arises from Keplerian motion of a planetary companion.

The orbital analysis is based on three distinct models: a circular single Keplerian, an eccentric single Keplerian, and two circular Keplerians in a likely 2:1 mean motion resonance. To compare the fit quality of the circular single-planet model with that of the more complex models, we carried out a likelihood ratio test. Both, the eccentric single-planet, as well as the circular two-planet solution, provide a significantly better solution than the circular single-planet solution, which we therefore rejected as a plausible explanation for the data. The eccentric single-planet model and the two-planet model are described by the same number of free parameters. As a matter of fact, the eccentric single planet model yields a higher likelihood and also a smaller jitter term on the grounds of which it might be preferred. To further quantify this statement, we generated synthetic data sets based on the eccentric and the two-planet solution, and inspected the likelihood ratio distributions. Our investigations show that none of the models can be rejected on statistical grounds. As both models are also physically plausible, we discuss their implications below.

Based on the eccentric model, GJ 4276 b has a minimum mass of  $\sim 16.6 M_{\oplus}$ , an orbital period of 13.4 days, and is located closer than the inner edge of the habitable zone at 0.08 au. At this orbital distance the tidal circularization timescale for a gaseous planet is more than 10 Gyr, which is consistent with an eccentric orbit. Analyzing the periodogram of the residual RVs, we find no immediate evidence for further planetary companions around GJ 4276. We shown in Fig. 7 the eccentricity of the known exoplanets around M dwarfs as a function of orbital period. There are 13 planetary systems with published eccentricities of  $e \geq 0.3$ . With a relatively high eccentricity of  $0.37 \pm 0.03$ , GJ 4276 b would be among the most eccentric exoplanets around M dwarfs known to date and comparable with the recently published exoplanet GJ 96 b with  $e = 0.44^{+0.09}_{-0.11}$  (Hobson et al. 2018). However, while both planets have similar masses, they differ significantly in the orbital period ( $m \sin i = 19.66^{+2.42}_{-2.30} M_{\oplus}$  and  $P = 73.94^{+0.33}_{-0.38}$  d for GJ 96 b).

A 2:1 mean motion resonance is found in many planetary systems such as HD 82943, HD 128311, HD 73526, HD 90043, and HD 27894 (Mayor et al. 2004; Vogt et al. 2005; Tinney et al. 2006; Johnson et al. 2011; Trifonov et al. 2017). So far, two systems with M dwarf host stars and planets near the 2:1 resonance are known, viz., GJ 876 (Marcy et al. 2001; Rivera et al. 2010) and TRAPPIST-1 (Gillon et al. 2017). Both of these systems harbor more than two known planets with orbital periods in a 4:2:1 resonance chain for GJ 876 and 8:5:3:2:1 for TRAPPIST-1. Given these examples, we consider a resonant two-planet system also a plausible model for GJ 4276. While we here focus on a strict 2:1 period ratio, we note that a slightly larger period ratio around 2.2 is often realized (Steffen & Hwang 2015). Also, strictly zero eccentricity, as assumed in our modeling, discards the dynamical mutual gravitational interaction between the planets, which is expected to lead to small, periodically changing eccentricities in the system. However, we consider this idealization of the two-planet model justified, to study the data set at hand. According to our two-planet model with a period ratio of 2:1, the planets GJ 4276 b and c have minimum masses of  $m_b \sin i = 15.6 M_{\oplus}$  and  $m_c \sin i = 4.4 M_{\oplus}$ . The two planets orbit their parent star at separations of  $a_b = 0.08$  au and  $a_c = 0.05$  au and have orbital periods of  $P_b = 2P_c = 13.35$  days. Still, both planets would be inward of the habitable zone.

Based on our statistical analysis, we express some preference for the single-planet eccentric solution. However, also the two-planet mean motion resonance is physically plausible, albeit formally less strongly backed by the data at hand. Conclusive evidence for one or the other alternative requires the number of RV measurements to be increased with follow-up observations. Nevertheless, the GJ 4276 planetary system shows a special configuration, making it a highly interesting object for follow-up studies.

*Acknowledgements.* CARMENES is an instrument for the Centro Astronómico Hispano-Alemán de Calar Alto (CAHA, Almería, Spain). CARMENES is funded by the German Max-Planck-Gesellschaft (MPG), the Spanish Consejo Superior de Investigaciones Científicas (CSIC), the European Union through FEDER/ERF FICTS-2011-02 funds, and the members of the CARMENES Consortium (Max-Planck-Institut für Astronomie, Instituto de Astrofísica de Andalucía, Landessternwarte Königstuhl, Institut de Ciències de l’Espai, Institut für Astrophysik Göttingen, Universidad Complutense de Madrid, Thüringer Landessternwarte Tautenburg, Instituto de Astrofísica de Canarias, Hamburger Sternwarte, Centro de Astrobiología and Centro Astronómico Hispano-Alemán), with additional contributions by the Spanish Ministry of Science through projects AYA2016-79425-C3-1/2/3-P, AYA2015-69350-C3-2-P, ESP2017-87676-C05-02-R, ESP2014-54362P, and ESP2017-87143R, the German Science Foundation through the Major Research Instrumentation Programme and DFG Research Unit FOR2544 “Blue Planets around Red Stars”, the Klaus Tschira Stiftung, the states of Baden-Württemberg and Niedersachsen,

and by the Junta de Andalucía. This work made use of observations collected at Sierra Nevada Observatory (SNO) supported by the Instituto de Astrofísica de Andalucía, CSIC, and from the LCOGT network. EN acknowledges support through DFG project CZ 222/1-1. S.C. acknowledges support from DFG project SCH 1382/2-1 and SCHM 1032/66-1. G.A.-E. research is funded via the STFC Consolidated Grants ST/P000592/1, and a Perren foundation grant. This work was prepared using PyAstronomy. This research has also made use of the corner.py package (Foreman-Mackey 2016).

## References

- Anglada-Escudé, G., López-Morales, M., & Chambers, J. E. 2010, *ApJ*, 709, 168  
 Baluev, R. V. 2009, *MNRAS*, 393, 969  
 Barnes, S. A. 2007, *ApJ*, 669, 1167  
 Bauer, F. F., Zechmeister, M., & Reiners, A. 2015, *A&A*, 581, A117  
 Berta, Z. K., Irwin, J., Charbonneau, D., Burke, C. J., & Falco, E. E. 2012, *AJ*, 144, 145  
 Boisvert, J. H., Nelson, B. E., & Steffen, J. H. 2018, *MNRAS*, 480, 2846  
 Caballero, J. A., Guàrdia, J., López del Fresno, M., et al. 2016, *Proc. SPIE*, 9910, 99100E  
 Cortés-Contreras, M. 2016, PhD thesis, Universidad Complutense de Madrid, Spain  
 Cumming, A., Marcy, G. W., & Butler, R. P. 1999, *ApJ*, 526, 890  
 Czesla, S., & Schmitt, J. H. M. M. 2010, *A&A*, 520, A38  
 Díez Alonso, E., Caballero, J. A., Montes, D., et al. 2019, *A&A*, 621, A126  
 Dressing, C. D., & Charbonneau, D. 2015, *ApJ*, 807, 45  
 Foreman-Mackey, D. 2016, *J. Open Source Software*, 24  
 Foreman-Mackey, D., Hogg, D. W., Lang, D., & Goodman, J. 2013, *PASP*, 125, 306  
 Gaia Collaboration (Brown, A. G. A., et al.) 2018, *A&A*, 616, A1  
 Gillon, M., Triaud, A. H. M. J., Demory, B.-O., et al. 2017, *Nature*, 542, 456  
 Henry, T. J., Jao, W.-C., Subasavage, J. P., et al. 2006, *AJ*, 132, 2360  
 Hobson, M. J., Díaz, R. F., Delfosse, X., et al. 2018, *A&A*, 618, A103  
 Husser, T.-O., Wende-von Berg, S., Dreizler, S., et al. 2013, *A&A*, 553, A6  
 Jackson, B., Greenberg, R., & Barnes, R. 2008, *ApJ*, 678, 1396  
 Johnson, J. A., Payne, M., Howard, A. W., et al. 2011, *AJ*, 141, 16  
 Kaminski, A., Trifonov, T., Caballero, J. A., et al. 2018, *A&A*, 618, A115  
 Kopparapu, R. K., Ramirez, R., Kasting, J. F., et al. 2013, *ApJ*, 765, 131  
 Kopparapu, R. K., Ramirez, R. M., Schottelkotte, J., et al. 2014, *ApJ*, 787, L29  
 Kürster, M., Trifonov, T., Reffert, S., Kostogryz, N. M., & Rodler, F. 2015, *A&A*, 577, A103  
 Lépine, S., Hilton, E. J., Mann, A. W., et al. 2013, *AJ*, 145, 102  
 Luque, R., Nowak, G., Pallé, E., et al. 2018, *A&A*, 620, A171  
 Marcy, G. W., Butler, R. P., Fischer, D., et al. 2001, *ApJ*, 556, 296  
 Mayor, M., Udry, S., Naef, D., et al. 2004, *A&A*, 415, 391  
 Nelder, J. A., & Mead, R. 1965, *Comput. J.*, 7, 308  
 Passegger, V. M., Reiners, A., Jeffers, S. V., et al. 2018, *A&A*, 615, A6  
 Protassov, R., van Dyk, D. A., Connors, A., Kashyap, V. L., & Siemiginowska, A. 2002, *ApJ*, 571, 545  
 Quirrenbach, A., Amado, P. J., Ribas, I., et al. 2018, *Proc. SPIE*, 10702, 107020W  
 Reid, I. N., Hawley, S. L., & Gizis, J. E. 1995, *AJ*, 110, 1838  
 Reiners, A., Zechmeister, M., Caballero, J. A., et al. 2018a, *A&A*, 612, A49  
 Reiners, A., Ribas, I., Zechmeister, M., et al. 2018b, *A&A*, 609, L5  
 Ribas, I., Tuomi, M., Reiners, A., et al. 2018, *Nature*, 563, 365  
 Rivera, E. J., Laughlin, G., Butler, R. P., et al. 2010, *ApJ*, 719, 890  
 Rodríguez, E., García, J. M., Costa, V., et al. 2010, *MNRAS*, 408, 2149  
 Roeser, S., Demleitner, M., & Schilbach, E. 2010, *AJ*, 139, 2440  
 Sarkis, P., Henning, T., Kürster, M., et al. 2018, *AJ*, 155, 257  
 Schäfer, S., Guenther, E. W., Reiners, A., et al. 2018, *Proc. SPIE*, 10702, 1070276  
 Schmitt, J. H. M. M., Fleming, T. A., & Giampapa, M. S. 1995, *ApJ*, 450, 392  
 Seager, S., & Mallén-Ornelas, G. 2003, *ApJ*, 585, 1038  
 Shapsee, B. J., Prieto, J. L., Grupe, D., et al. 2014, *ApJ*, 788, 48  
 Skrutskie, M. F., Cutri, R. M., Stiening, R., et al. 2006, *AJ*, 131, 1163  
 Steffen, J. H., & Hwang, J. A. 2015, *MNRAS*, 448, 1956  
 Tinney, C. G., Butler, R. P., Marcy, G. W., et al. 2006, *ApJ*, 647, 594  
 Trifonov, T., Kürster, M., Zechmeister, M., et al. 2017, *A&A*, 602, L8  
 Trifonov, T., Kürster, M., Zechmeister, M., et al. 2018, *A&A*, 609, A117  
 Vogt, S. S., Butler, R. P., Marcy, G. W., et al. 2005, *ApJ*, 632, 638  
 Wilks, S. S. 1938, *Ann. Math. Statist.*, 9, 60  
 Wittenmyer, R. A., Wang, S., Horner, J., et al. 2013, *ApJS*, 208, 2  
 Wright, J. T., & Eastman, J. D. 2014, *PASP*, 126, 838  
 Zechmeister, M., & Kürster, M. 2009, *A&A*, 496, 577  
 Zechmeister, M., Kürster, M., & Endl, M. 2009, *A&A*, 505, 859  
 Zechmeister, M., Anglada-Escudé, G., & Reiners, A. 2014, *A&A*, 561, A59  
 Zechmeister, M., Reiners, A., Amado, P. J., et al. 2018, *A&A*, 609, A12

## Appendix A: Rotation period analysis

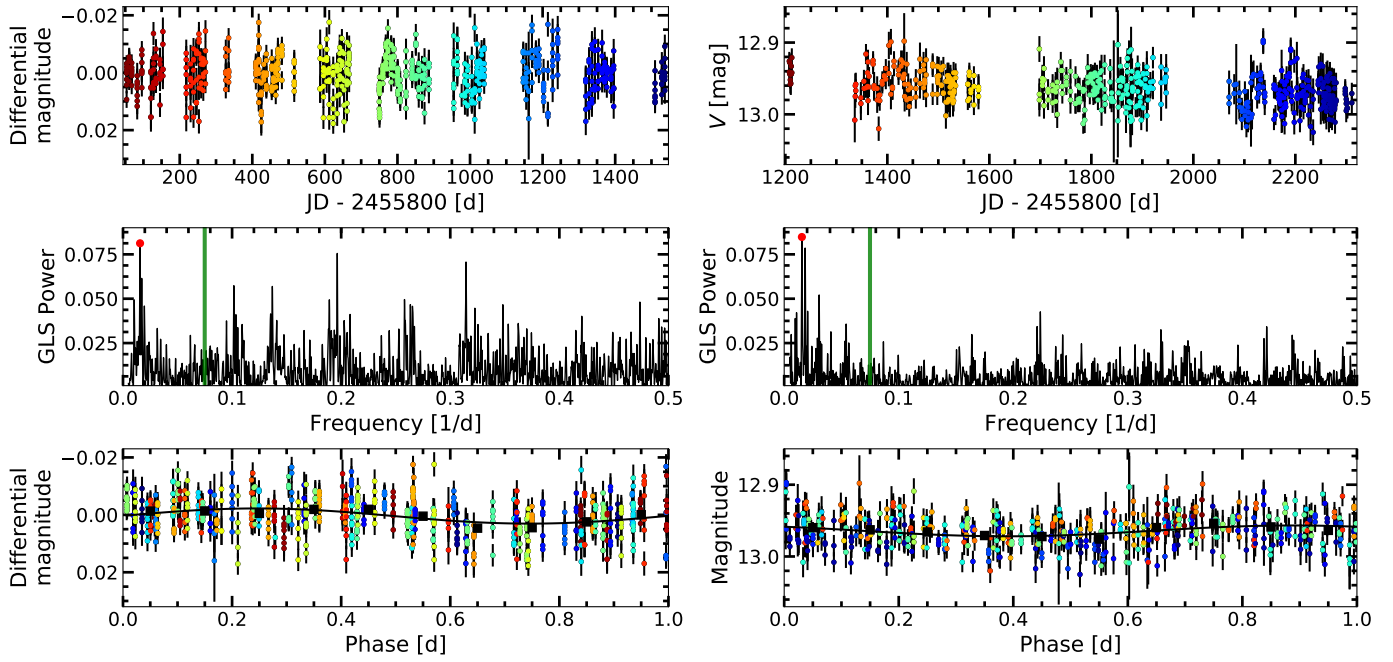


**Fig. A.1.** Rotation period analysis using MEarth (*left panel*) and ASAS-SN (*right panel*) photometric data. *Top panel:* RG715 broadband light curve (*left panel*) and V band light curve (*right panel*). The color of the datapoints indicates the observation epoch. *Middle panel:* GLS periodograms. The vertical green lines represent the orbital period of the planet at 13.35 days and the red dots the peak with the highest power at 63.9 days (*left panel*) and 64.7 days (*right panel*). *Bottom panel:* phased light curves using the rotation period derived from the GLS. The black curves show the best-fit sinusoidal models with an amplitude of 2.64 mmag (*left panel*) and 7.53 mmag (*right panel*). The black squares indicate the mean magnitude in ten equidistant bins in phase.

## Appendix B: MCMC cornerplots

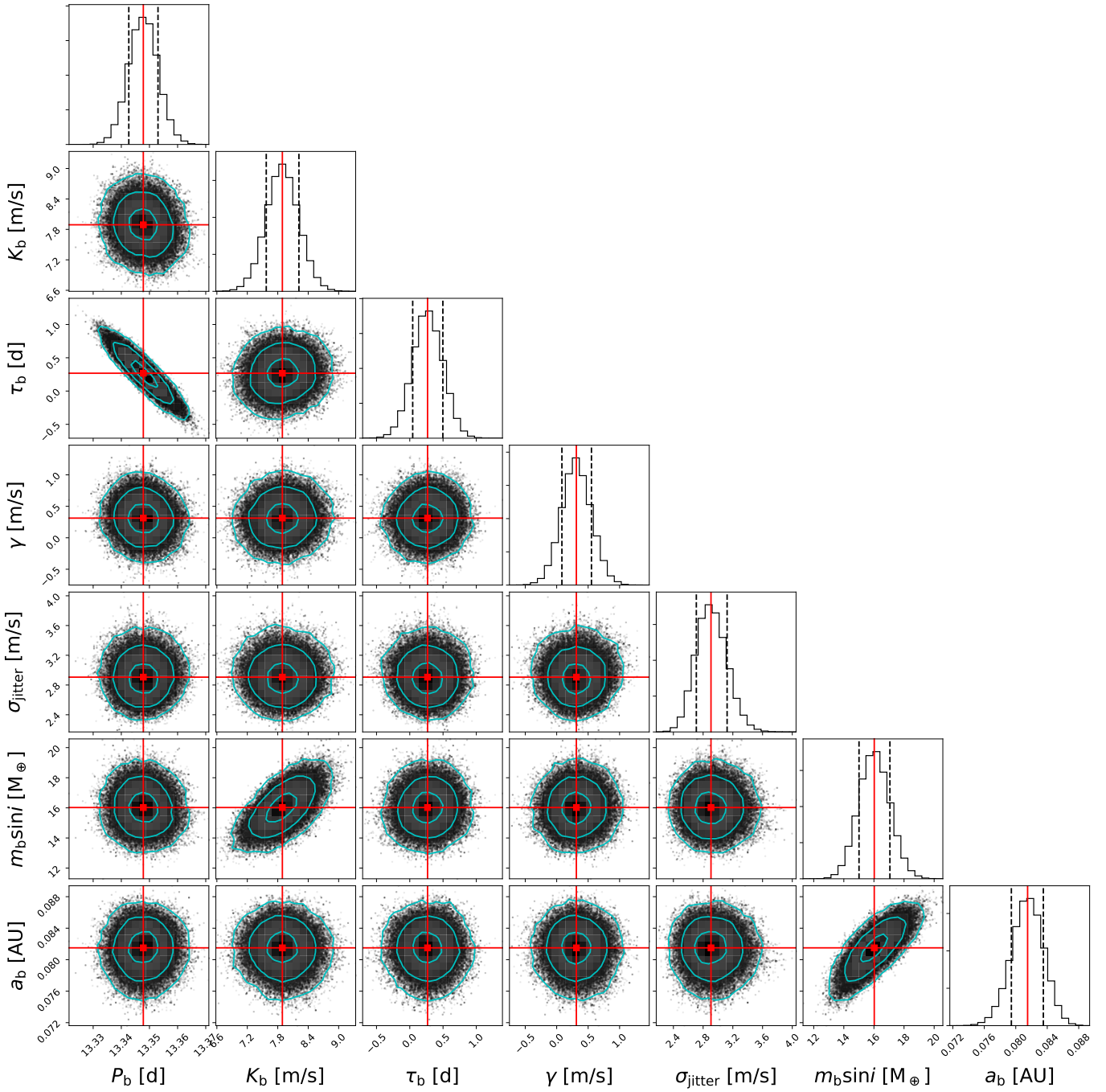


**Fig. B.1.** Two-dimensional projections of the posterior probability distributions of the circular single-planet Keplerian model. The contours represent the 1, 2, and 3 $\sigma$  uncertainty levels.

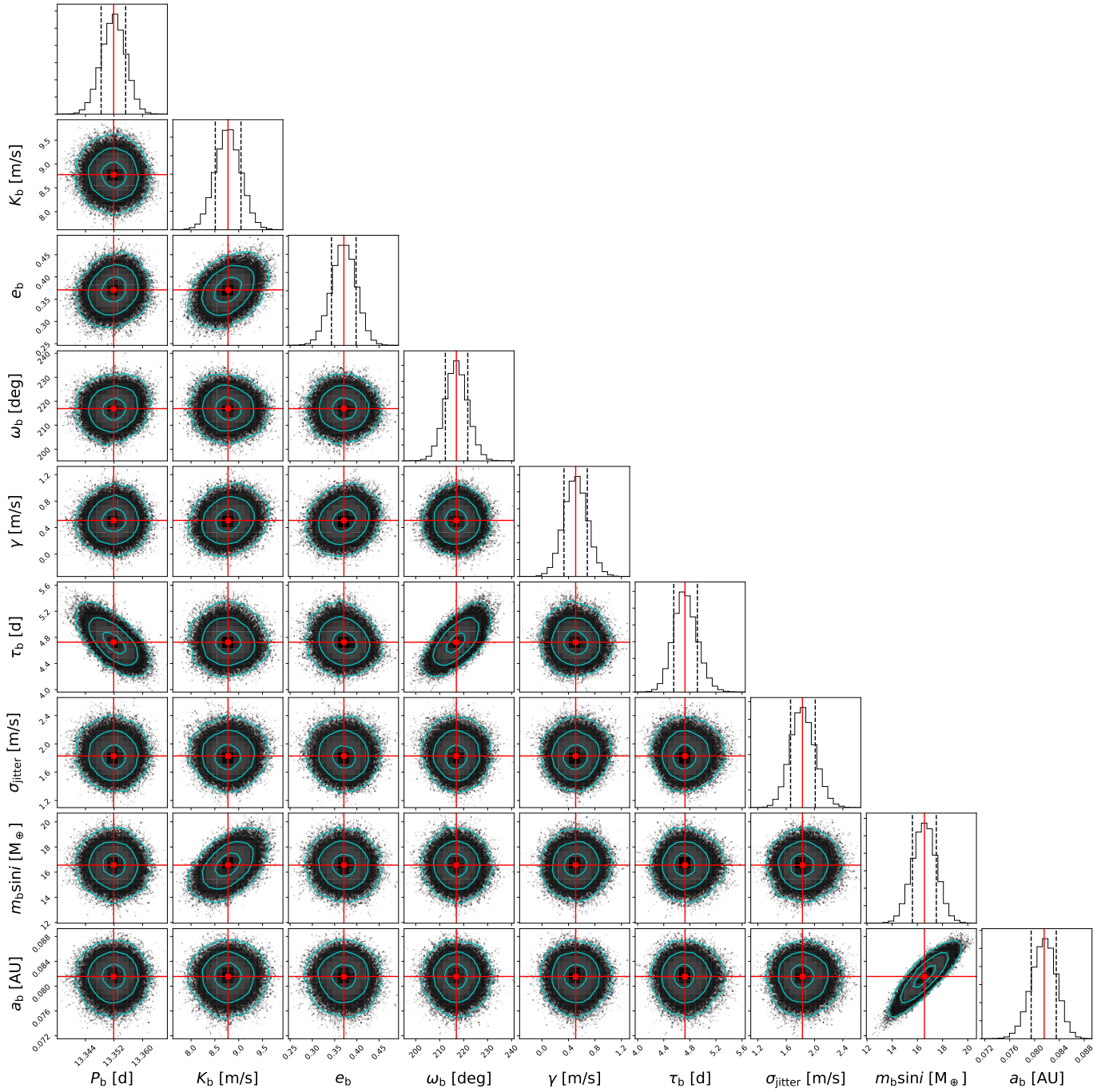


**Fig. B.2.** Same as Fig. B.1 but for the eccentric single-planet Keplerian model.

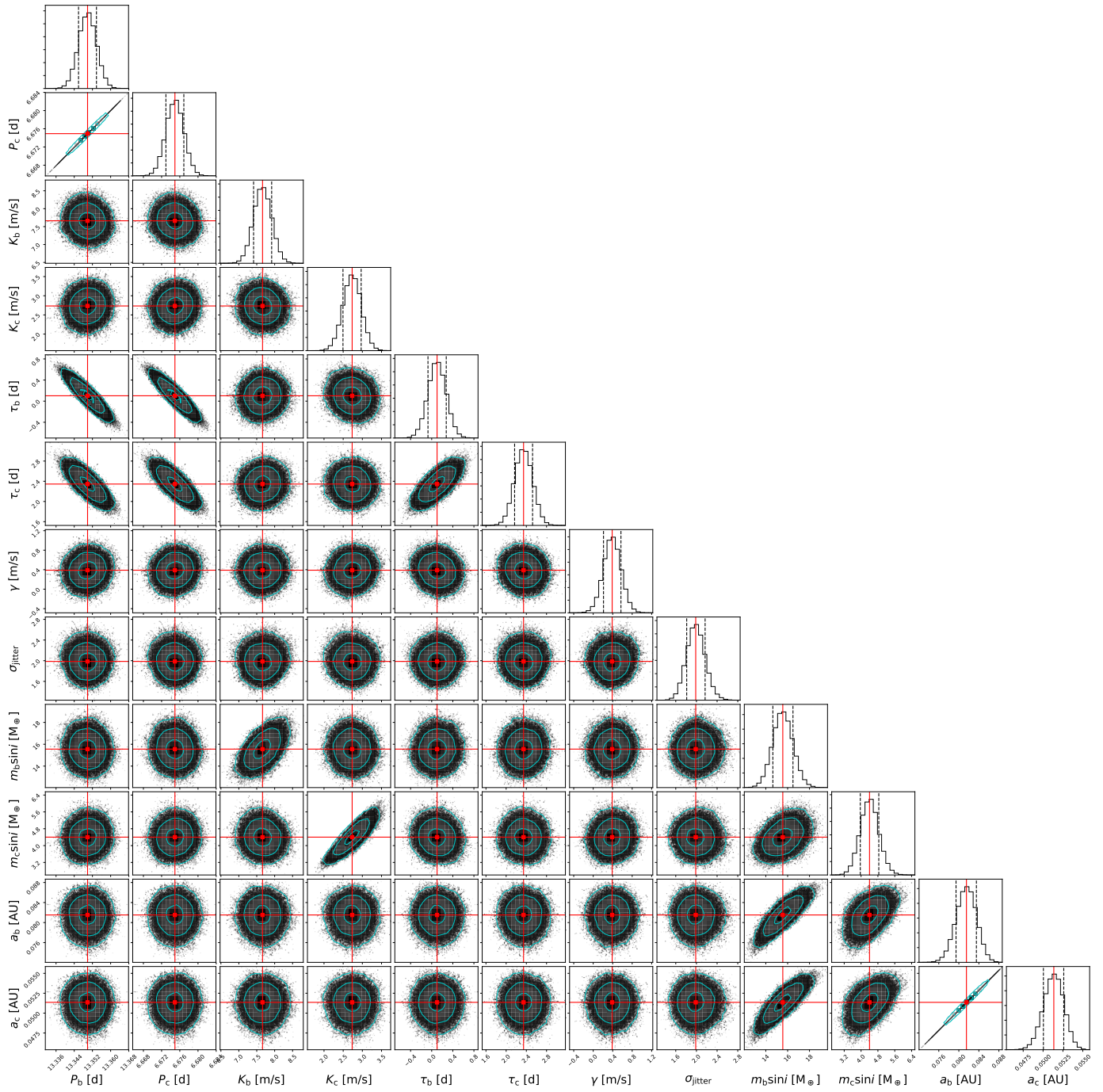


**Fig. B.3.** Same as Fig. B.1 but for the two-planet Keplerian model on circular orbits with a period ratio of 2:1.

## Appendix C: Radial velocities of GJ 4276

Table C.1. continued.

Table C.1. Barycentric Julian date, radial velocities, and formal uncertainties for GJ 4276.

| BJD         | RV (m s <sup>-1</sup> ) | $\sigma_{RV}$ (m s <sup>-1</sup> ) | BJD         | RV (m s <sup>-1</sup> ) | $\sigma_{RV}$ (m s <sup>-1</sup> ) |
|-------------|-------------------------|------------------------------------|-------------|-------------------------|------------------------------------|
| 2457572.656 | 3.60                    | 2.03                               | 2458132.329 | 7.91                    | 3.89                               |
| 2457592.602 | 3.37                    | 2.36                               | 2458134.272 | 0.05                    | 2.15                               |
| 2457603.619 | -8.50                   | 3.11                               | 2458135.303 | -5.76                   | 1.84                               |
| 2457610.546 | 3.53                    | 1.72                               | 2458136.306 | -8.59                   | 1.41                               |
| 2457612.517 | -3.72                   | 1.91                               | 2458138.319 | -1.71                   | 2.32                               |
| 2457618.462 | 0.21                    | 2.04                               | 2458139.319 | 2.36                    | 1.93                               |
| 2457619.542 | 5.18                    | 1.69                               | 2458140.321 | 8.12                    | 1.83                               |
| 2457620.491 | 4.62                    | 1.70                               | 2458141.387 | 7.82                    | 1.63                               |
| 2457621.515 | 4.97                    | 1.69                               | 2458143.277 | 4.20                    | 1.62                               |
| 2457622.477 | 7.59                    | 1.62                               | 2458144.278 | 6.19                    | 2.82                               |
| 2457628.501 | -8.30                   | 1.44                               | 2458149.292 | -9.06                   | 1.91                               |
| 2457629.505 | -14.72                  | 1.98                               | 2458159.288 | 8.75                    | 2.62                               |
| 2457643.487 | -6.80                   | 1.47                               | 2458249.639 | 8.22                    | 1.82                               |
| 2457937.636 | -7.59                   | 1.61                               | 2458263.662 | 10.49                   | 2.94                               |
| 2457948.647 | -7.85                   | 1.64                               | 2458270.656 | -9.49                   | 2.39                               |
| 2457954.573 | 7.69                    | 1.66                               | 2458284.631 | -6.51                   | 1.69                               |
| 2457960.578 | -2.08                   | 1.39                               | 2458290.631 | 6.73                    | 1.94                               |
| 2457961.548 | -5.11                   | 1.27                               | 2458291.634 | 4.76                    | 1.75                               |
| 2457969.522 | 3.71                    | 1.38                               | 2458292.638 | 1.13                    | 1.56                               |
| 2457970.466 | 6.85                    | 1.47                               | 2458293.645 | -0.85                   | 1.48                               |
| 2457975.539 | -7.87                   | 1.96                               | 2458296.629 | -14.35                  | 1.83                               |
| 2457976.584 | -12.65                  | 1.77                               | 2458297.620 | -8.54                   | 1.51                               |
| 2457977.512 | -9.26                   | 1.54                               | 2458300.615 | 4.96                    | 2.00                               |
| 2457982.533 | 2.94                    | 1.51                               | 2458303.611 | 10.32                   | 2.84                               |
| 2457986.547 | -3.51                   | 1.57                               | 2458304.630 | 4.17                    | 2.94                               |
| 2457999.432 | 0.29                    | 1.85                               | 2458305.624 | 4.64                    | 1.79                               |
| 2458000.497 | -4.17                   | 1.66                               | 2458306.622 | 4.94                    | 1.86                               |
| 2458001.470 | -4.53                   | 1.36                               | 2458309.589 | -9.87                   | 1.90                               |
| 2458002.655 | -10.19                  | 1.46                               | 2458313.607 | 3.33                    | 1.39                               |
| 2458008.516 | 1.83                    | 1.54                               | 2458315.596 | 7.10                    | 2.95                               |
| 2458009.622 | 1.33                    | 1.48                               | 2458316.596 | 5.01                    | 1.68                               |
| 2458026.548 | 3.43                    | 1.97                               | 2458317.624 | 8.02                    | 2.07                               |
| 2458029.417 | -4.00                   | 1.77                               | 2458318.617 | 6.41                    | 2.03                               |
| 2458032.565 | 6.92                    | 2.10                               | 2458324.627 | -7.49                   | 1.60                               |
| 2458033.375 | 7.82                    | 1.87                               | 2458326.621 | 4.03                    | 1.40                               |
| 2458034.555 | 9.38                    | 2.20                               | 2458327.603 | 9.50                    | 1.41                               |
| 2458035.498 | 6.22                    | 2.51                               | 2458330.590 | 8.47                    | 1.29                               |
| 2458047.456 | 2.70                    | 1.80                               | 2458332.595 | 4.96                    | 1.27                               |
| 2458048.458 | 4.55                    | 1.55                               | 2458336.603 | -9.74                   | 1.53                               |
| 2458050.361 | 2.97                    | 1.96                               | 2458337.671 | -8.30                   | 1.49                               |
| 2458052.457 | -1.19                   | 1.44                               | 2458338.509 | -5.47                   | 1.64                               |
| 2458053.418 | -1.22                   | 1.75                               | 2458339.580 | 4.10                    | 1.64                               |
| 2458055.536 | -6.62                   | 1.47                               | 2458340.620 | 6.97                    | 1.35                               |
| 2458059.511 | 10.06                   | 1.75                               | 2458343.563 | 4.52                    | 1.52                               |
| 2458079.404 | 0.41                    | 1.75                               | 2458345.561 | 1.04                    | 1.43                               |
| 2458084.341 | -10.03                  | 1.55                               | 2458346.542 | -1.60                   | 1.53                               |
| 2458092.477 | 5.58                    | 1.36                               |             |                         |                                    |
| 2458093.333 | 3.55                    | 1.19                               |             |                         |                                    |
| 2458110.362 | -9.05                   | 1.76                               |             |                         |                                    |
| 2458118.407 | 3.71                    | 1.66                               |             |                         |                                    |
| 2458120.361 | 0.99                    | 2.67                               |             |                         |                                    |
| 2458121.269 | -2.72                   | 1.48                               |             |                         |                                    |
| 2458122.275 | -8.60                   | 1.36                               |             |                         |                                    |
| 2458123.268 | -7.80                   | 1.38                               |             |                         |                                    |



## 5.4 Further publications

In this section I present further publications that were produced by members within the CARMENES collaboration and directly benefit from an accurate correction of telluric absorption. The topics of the publications can be divided into studies of atmospheric characterizations of exoplanetary atmospheres based on the analysis of transmission spectra (papers 1-7), detection and characterization of exoplanetary systems using radial velocity measurements (papers 8-10), magnetic field measurements in M dwarfs (paper 11), determination of fundamental stellar parameters (papers 12 & 13), chromospheric activity study of M dwarfs based on the analysis of the helium triplet at 10830 Å (paper 14), and the detection and characterization of spectroscopic binary M dwarfs (paper 15). The large variety of scientific topics highlights the importance of a proper telluric line treatment in the analysis of high-resolution spectra, especially in the near-infrared wavelength domain.

The sections about the telluric correction procedure in Nortmann et al. (2018) and Salz et al. (2018) was written by myself. I performed the telluric correction of the CARMENES spectra in all the publications and provided additional information, for example about the atmospheric conditions during the observations and precipitable water vapor data. Further, I provided high S/N stellar templates constructed from uncorrected as well as from corrected spectral series. Finally, I computed radial velocities from telluric corrected spectra for those publications that deal with the analysis of radial velocity data.

1. *Ground-based detection of an extended helium atmosphere in the Saturn-mass exoplanet WASP-69 b*  
Nortmann, L., Pallé, E., Salz, M., Sanz-Forcada, J., **Nagel, E.**, Alonso-Floriano, F. J., Czesla, S., Yan, F., Chen, G., Snellen, I. A. G., Zechmeister, M., Schmitt, J. H. M. M., López-Puertas, M., Casasayas-Barris, N., Bauer, F. F., Amado, P. J., Caballero, J. A., Dreizler, S., Henning, T., Lampón, M., Montes, D., Molaverdikhani, K., Quirrenbach, A., Reiners, A., Ribas, I., Sánchez-López, A., Schneider, P. C., Zapatero Osorio, M. R., *Science*, 362, 1388N (2018)
2. *Detection of He I  $\lambda$  10830 Å absorption on HD 189733 b with CARMENES high-resolution transmission spectroscopy*  
Salz, M., Czesla, S., Schneider, P. C., **Nagel, E.**, Schmitt, J. H. M. M., Nortmann, L., Alonso-Floriano, F. J., López-Puertas, M., Lampón, M., Bauer, F. F., Snellen, I. A. G., Pallé, E., Caballero, J. A., Yan, F., Chen, G., Sanz-Forcada, J., Amado, P. J., Quirrenbach, A., Ribas, I., Reiners, A., Béjar, V. J. S., Casasayas-Barris, N., Cortés-Contreras, M., Dreizler, S., Guenther, E. W., Henning, T., Jeffers, S. V., Kaminski, A., Kürster, M., Lafarga, M., Lara, L. M., Molaverdikhani, K., Montes, D., Morales, J. C., Sánchez-López, A., Seifert, W., Zapatero Osorio, M. R., Zechmeister, M., *Astronomy & Astrophysics*, 620A, 97S (2018)
3. *Multiple water band detections in the CARMENES near-infrared transmission spectrum of HD 189733 b*  
Alonso-Floriano, F. J., Sánchez-López, A., Snellen, I. A. G., López-Puertas, M., **Nagel, E.**, Amado, P. J., Bauer, F. F., Caballero, J. A., Czesla, S., Nortmann, L., Pallé, E., Salz, M., Reiners, A., Ribas, I., Quirrenbach, A., Aceituno, J., Anglada-Escudé, G., Béjar, V. J. S., Guenther, E. W., Henning, T., Kaminski, A., Kürster, M., Lampón, M., Lara, L. M., Montes, D., Morales, J. C., Tal-Or, L., Schmitt, J. H. M. M., Zapatero Osorio, M. R., Zechmeister, M., *Astronomy & Astrophysics*, 621A, 74A (2019)

4. *He I  $\lambda$  10 830 Å in the transmission spectrum of HD 209458 b*  
Alonso-Floriano, F. J., Snellen, I. A. G., Czesla, S., Bauer, F. F., Salz, M., Lampón, M., Lara, L. M., **Nagel, E.**, López-Puertas, M., Nortmann, L., Sánchez-López, A., Sanz-Forcada, J., Caballero, J. A., Reiners, A., Ribas, I., Quirrenbach, A., Amado, P. J., Aceituno, J., Anglada-Escudé, G., Béjar, V. J. S., Brinkmüller, M., Hatzes, A. P., Henning, T., Kaminski, A., Kürster, M., Labarga, F., Montes, D., Pallé, E., Schmitt, J. H. M. M., Zapatero Osorio, M. R.,  
Astronomy & Astrophysics, 629A, 110A (2019)
5. *Water vapor detection in the transmission spectra of HD 209458 b with the CARMENES NIR channel*  
Sánchez-López, A., Alonso-Floriano, F. J., López-Puertas, M., Snellen, I. A. G., Funke, B., **Nagel, E.**, Bauer, F. F., Amado, P. J., Caballero, J. A., Czesla, S., Nortmann, L., Pallé, E., Salz, M., Reiners, A., Ribas, I., Quirrenbach, A., Anglada-Escudé, G., Béjar, V. J. S., Casasayas-Barris, N., Galadí-Enríquez, D., Guenther, E. W., Henning, T., Kaminski, A., Kürster, M., Lampón, M., Lara, L. M., Montes, D., Morales, J. C., Stangret, M., Tal-Or, L., Sanz-Forcada, J., Schmitt, J. H. M. M., Zapatero Osorio, M. R., Zechmeister, M.,  
Astronomy & Astrophysics, 630A, 53S (2019)
6. *Atmospheric characterization of the ultra-hot Jupiter MASCARA-2b/KELT-20b. Detection of CaII, FeII, NaI, and the Balmer series of H ( $H\alpha$ ,  $H\beta$ , and  $H\gamma$ ) with high-dispersion transit spectroscopy*  
Casasayas-Barris, N., Pallé, E., Yan, F., Chen, G., Kohl, S., Stangret, M., Parvainen, H., Helling, Ch., Watanabe, N., Czesla, S., Fukui, A., Montañés-Rodríguez, P., **Nagel, E.**, Narita, N., Nortmann, L., Nowak, G., Schmitt, J. H. M. M., Zapatero Osorio, M. R.  
Astronomy & Astrophysics, 628A, 9C (2019)
7. Yan, F., Casasayas-Barris, N., Molaverdikhani, K., Alonso-Floriano, F. J., Reiners, A., Pallé, E., Henning, T., Mollière, P., Chen, G., Nortmann, L., Snellen, I. A. G., Ribas, I., Quirrenbach, A., Caballero, J. A., Amado, P. J., Azzaro, M., Bauer, F. F., Cortés-Contreras, M., Czesla, S., Khalafinejad, S., Lara, L. M., López-Puertas, M., Montes, D., **Nagel, E.**, Oshagh, M., Sánchez-López, A., Stangret, M., Zechmeister, M.  
Submitted to Astronomy & Astrophysics
8. *Detection and characterization of an ultra-dense sub-Neptunian planet orbiting the Sun-like star K2-292*  
Luque, R., Nowak, G., Pallé, E., Dai, F., Kaminski, A., **Nagel, E.**, Hidalgo, D., Bauer, F., Lafarga, M., Livingston, J., Barragán, O., Hirano, T., Fridlund, M., Gandolfi, D., Justesen, A. B., Hjorth, M., Van Eylen, V., Winn, J. N., Esposito, M., Morales, J. C., Albrecht, S., Alonso, R., Amado, P. J., Beck, P., Caballero, J. A., Cabrera, J., Cochran, W. D., Csizmadia, Sz., Deeg, H., Eigmüller, Ph., Endl, M., Erikson, A., Fukui, A., Grziwa, S., Guenther, E. W., Hatzes, A. P., Knudstrup, E., Korth, J., Lam, K. W. F., Lund, M. N., Mathur, S., Montañés-Rodríguez, P., Narita, N., Nespral, D., Niraula, P., Pätzold, M., Persson, C. M., Prieto-Arranz, J., Quirrenbach, A., Rauer, H., Redfield, S., Reiners, A., Ribas, I., Smith, A. M. S.,  
Astronomy & Astrophysics, 623A, 114L (2019)
9. *Planetary system around the nearby M dwarf GJ 357 including a transiting, hot, Earth-sized planet optimal for atmospheric characterization*  
Luque, R., Pallé, E., Kossakowski, D., Dreizler, S., Kemmer, J., Espinoza, N., Burt,

- J., Anglada-Escudé, G., Béjar, V. J. S., Caballero, J. A., Collins, K. A., Collins, K. I., Cortés-Contreras, M., Díez-Alonso, E., Feng, F., Hatzes, A., Hellier, C., Henning, T., Jeffers, S. V., Kaltenegger, L., Kürster, M., Madden, J., Molaverdikhani, K., Montes, D., Narita, N., Nowak, G., Ofir, A., Oshagh, M., Parviainen, H., Quirrenbach, A., Reffert, S., Reiners, A., Rodríguez-López, C., Schlecker, M., Stock, S., Trifonov, T., Winn, J. N., Zapatero Osorio, M. R., Zechmeister, M., Amado, P. J., Anderson, D. R., Batalha, N. E., Bauer, F. F., Bluhm, P., Burke, C. J., Butler, R. P., Caldwell, D. A., Chen, G., Crane, J. D., Dragomir, D., Dressing, C. D., Dynes, S., Jenkins, J. M., Kaminski, A., Klahr, H., Kotani, T., Lafarga, M., Latham, D. W., Lewin, P., McDermott, S., Montañés-Rodríguez, P., Morales, J. C., Murgas, F., **Nagel, E.**, Pedraz, S., Ribas, I., Ricker, G. R., Rowden, P., Seager, S., Shectman, S. A., Tamura, M., Teske, J., Twicken, J. D., Vanderspeck, R., Wang, S. X., Wohler, B.,  
*Astronomy & Astrophysics*, 628A, 39L (2019)
10. *A giant exoplanet orbiting a very-low-mass star challenges planet formation models*  
 Morales, J. C., Mustill, A. J., Ribas, I., Davies, M. B., Reiners, A., Bauer, F. F., Kosakowski, D., Herrero, E., Rodríguez, E., López-González, M. J., Rodríguez-López, C., Béjar, V. J. S., González-Cuesta, L., Luque, R., Pallé, E., Perger, M., Baroch, D., Johansen, A., Klahr, H., Mordasini, C., Anglada-Escudé, G., Caballero, J. A., Cortés-Contreras, M., Dreizler, S., Lafarga, M., **Nagel, E.**, Passegger, V. M., Reffert, S., Rosich, A., Schweitzer, A., Tal-Or, L., Trifonov, T., Zechmeister, M., Quirrenbach, A., Amado, P. J., Guenther, E. W., Hagen, H. J., Henning, T., Jeffers, S. V., Kaminski, A., Kürster, M., Montes, D., Seifert, W., Abellán, F. J., Abril, M., Aceituno, J., Aceituno, F. J., Alonso-Floriano, F. J., Ammler-von Eiff, M., Antona, R., Arroyo-Torres, B., Azzaro, M., Barrado, D., Becerril-Jarque, S., Benítez, D., Berdiñas, Z. M., Bergond, G., Brinkmöller, M., del Burgo, C., Burn, R., Calvo-Ortega, R., Cano, J., Cárdenas, M. C., Cardona Guillén, C., Carro, J., Casal, E., Casanova, V., Casasayas-Barris, N., Chaturvedi, P., Cifuentes, C., Claret, A., Colomé, J., Czesla, S., Díez-Alonso, E., Dorda, R., Emsenhuber, A., Fernández, M., Fernández-Martín, A., Ferro, I. M., Fuhrmeister, B., Galadí-Enríquez, D., Gallardo Cava, I., García Vargas, M. L., Garcia-Piquer, A., Gesa, L., González-Álvarez, E., González Hernández, J. I., González-Peinado, R., Guàrdia, J., Guijarro, A., de Guindos, E., Hatzes, A. P., Hauschildt, P. H., Hedrosa, R. P., Hermelo, I., Hernández Arabi, R., Hernández Otero, F., Hintz, D., Holgado, G., Huber, A., Huke, P., Johnson, E. N., de Juan, E., Kehr, M., Kemmer, J., Kim, M., Klüter, J., Klutsch, A., Labarga, F., Labiche, N., Lalitha, S., Lampón, M., Lara, L. M., Launhardt, R., Lázaro, F. J., Lizon, J. -L., Llamas, M., Lodieu, N., López del Fresno, M., López Salas, J. F., López-Santiago, J., Magán Madinabeitia, H., Mall, U., Mancini, L., Mandel, H., Marfil, E., Marín Molina, J. A., Martín, E. L., Martín-Fernández, P., Martín-Ruiz, S., Martínez-Rodríguez, H., Marvin, C. J., Mirabet, E., Moya, A., Naranjo, V., Nelson, R. P., Nortmann, L., Nowak, G., Ofir, A., Pascual, J., Pavlov, A., Pedraz, S., Pérez Medialdea, D., Pérez-Calpena, A., Perryman, M. A. C., Rabaza, O., Ramón Ballesta, A., Rebolo, R., Redondo, P., Rix, H. W., Rodler, F., Rodríguez Trinidad, A., Sabotta, S., Sadegi, S., Salz, M., Sánchez-Blanco, E., Sánchez Carrasco, M. A., Sánchez-López, A., Sanz-Forcada, J., Sarkis, P., Sarmiento, L. F., Schäfer, S., Schlecker, M., Schmitt, J. H. M. M., Schöfer, P., Solano, E., Sota, A., Stahl, O., Stock, S., Stuber, T., Stürmer, J., Suárez, J. C., Tabernero, H. M., Tulloch, S. M., Veredas, G., Vico-Linares, J. I., Vilardell, F., Wagner, K., Winkler, J., Wolthoff, V., Yan, F., Zapatero Osorio, M. R.  
*Science*, 365, 6460 (2019)

11. *Magnetic fields in M dwarfs from the CARMENES survey*  
Shulyak, D., Reiners, A., **Nagel, E.**, Tal-Or, L., Caballero, J. A., Zechmeister, M., Béjar, V. J. S., Cortés-Contreras, M., Martin, E. L., Kaminski, A., Ribas, I., Quirrenbach, A., Amado, P. J., Anglada-Escudé, G., Bauer, F. F., Dreizler, S., Guenther, E. W., Henning, T., Jeffers, S. V., Kürster, M., Lafarga, M., Montes, D., Morales, J. C., Pedraz, S., *Astronomy & Astrophysics*, 626A, 86S, (2019)
12. *The CARMENES search for exoplanets around M dwarfs. Photospheric parameters of target stars from high-resolution spectroscopy. II. Simultaneous multiwavelength range modeling of activity insensitive lines*  
Passegger, V. M., Schweitzer, A., Shulyak, D., **Nagel, E.**, Hauschildt, P. H., Reiners, A., Amado, P. J., Caballero, J. A., Cortés-Contreras, M., Domínguez-Fernández, A. J., Quirrenbach, A., Ribas, I., Azzaro, M., Anglada-Escudé, G., Bauer, F. F., Béjar, V. J. S., Dreizler, S., Guenther, E. W., Henning, T., Jeffers, S. V., Kaminski, A., Kürster, M., Lafarga, M., Martín, E. L., Montes, D., Morales, J. C., Schmitt, J. H. M. M., Zechmeister, M.,  
*Astronomy & Astrophysics*, 627A, 161P, (2019)
13. *Stellar atmospheric parameters of FGK-type stars from high-resolution optical and near-infrared CARMENES spectra*  
Marfil, E., Tabernero, H. M., Montes, D., Caballero, J. A., Soto, M. G., Gonzalez Hernandez, J. I., Kaminski, A., **Nagel, E.**, Jeffers, S. V., Reiners, A., Ribas, I., Quirrenbach, A., Amado, P. J.  
Submitted to *Monthly Notices of the Royal Astronomical Society*
14. *The CARMENES search for exoplanets around M dwarfs. The He I triplet at 10830 Å across the M dwarf sequence*  
Fuhrmeister, B., Czesla, S., Hildebrandt, L., **Nagel, E.**, Schmitt, J. H. M. M., Hintz, D., Johnson, E. N., Sanz-Forcada, J., Schöfer, P., Jeffers, S. V., Caballero, J. A., Zechmeister, M., Reiners, A., Ribas, I., Amado, P. J., Quirrenbach, A., Bauer, F. F., Béjar, V. J. S., Cortés-Contreras, M., Díez-Alonso, E., Dreizler, S., Galadí-Enríquez, D., Guenther, E. W., Kaminski, A., Kürster, M., Lafarga, M., Montes, D.,  
Submitted to *Astronomy & Astrophysics*
15. *The CARMENES search for exoplanets around M dwarfs. Nine new double-line spectroscopic binary stars*  
Baroch, D., Morales, J. C., Ribas, I., Tal-Or, L., Zechmeister, M., Reiners, A., Caballero, J. A., Quirrenbach, A., Amado, P. J., Dreizler, S., Lalitha, S., Jeffers, S. V., Lafarga, M., Béjar, V. J. S., Colomé, J., Cortés-Contreras, M., Díez-Alonso, E., Galadí-Enríquez, D., Guenther, E. W., Hagen, H. J., Henning, T., Herrero, E., Kürster, M., Montes, D., **Nagel, E.**, Passegger, V. M., Perger, M., Rosich, A., Schweitzer, A., Seifert, W.,  
*Astronomy & Astrophysics*, 619A, 32B (2018)

## 6 Summary

CARMENES is the first spectrograph aiming at a radial velocity precision of  $1 \text{ m s}^{-1}$  in the red optical and near-infrared wavelength range. Mounted at the 3.5 m telescope at the Calar Alto Observatory and operated by a consortium of eleven Spanish and German institutions, it conducts an exoplanet survey targeting a sample of  $\sim 300$  M dwarfs. With 750 GTO nights the survey will be one of the largest surveys ever conducted. CARMENES has been specifically designed and optimized to search for Earth-like planets in the habitable zones of low-mass stars. Radial velocity searches around these stars benefit from larger Doppler amplitudes and shorter orbital periods compared to solar-like stars. The large wavelength coverage ranging from  $0.52$  to  $1.71 \mu\text{m}$  provides a powerful tool to discriminate between true planetary companions and signals induced by stellar magnetic activity.

This thesis focused on velocimetry studies in the context of extrasolar planets using data taken with CARMENES. The first part of this PhD work deals with the telluric correction of CARMENES spectra and its impact on radial velocity precision. The motivation for this project arose from the fact that telluric contamination affects the entire spectral range covered by CARMENES and becomes very serious in the near-infrared wavelength range. Although there are atmospheric windows with only little telluric contamination, micro-telluric absorption is present at almost all near-infrared wavelengths. The standard procedure of telluric line treatment in the CARMENES radial velocity pipeline is to mask telluric features above a threshold of 5%. While the results are satisfactory in the visible channel, the broad telluric bands lead to extended masks. As a result, neglecting large masked sections of the stellar spectrum lowers the radial velocity precision. Moreover, shallow telluric lines still present in the spectroscopic data can introduce systematic effects and increase the error of the radial velocity precision.

A very common technique to correct for telluric lines is using telluric standard star observations close in time and airmass as the target observation. To save valuable telescope time in CARMENES, standard stars are not observed regularly during the night. Instead of using standard stars, synthetic atmospheric transmission spectra can be alternatively used and fitted to the observations. An accurate fit requires a clear defined continuum and isolated telluric lines. Both conditions are not fulfilled in M dwarf spectra.

To address this problem, I developed the Template Division Telluric Modeling technique. Based on the Earth's barycentric movement and taking advantage of the relative shift between telluric lines and stellar lines, this approach is able to disentangle chunks of the telluric spectrum and the stellar spectrum. The chunks of the telluric spectrum are then used to compute an atmospheric transmission model over the entire wavelength range of CARMENES and to derive telluric-free spectra. The quality of the TDTM approach and the correction was demonstrated by correcting spectral time series of the A0-type star 109 Vir and the M3.5-type star GJ 273 obtained with the visual and near-infrared channel of CARMENES. Telluric absorption lines with depths of up to  $\sim 50\%$  were corrected near the noise level.

In the next step, the impact of the telluric correction on the radial velocity precision was investigated by applying the TDTM technique to a time series of 22 visual and 13 near-

infrared spectra of GJ 1012. This star was selected because it shows a very low radial velocity variability in the visual range. New radial velocities were computed from the telluric corrected spectra employing a mask that excludes only telluric features deeper than 30 % and compared them to the radial velocities computed with the standard radial velocity pipeline, which employs a mask that excludes features deeper than 5 %. It was found that no significant improvement in radial velocity precision was obtained in the visual channel after the telluric correction. In the near-infrared, the impact of the telluric correction is significant. The radial velocity scatter was decreased by almost a factor of two from  $9.5 \text{ m s}^{-1}$  to  $5.7 \text{ m s}^{-1}$ .

So far, there is little knowledge on how to treat telluric features in precise radial velocity analyses. With CARMENES it is possible to study these effects in great detail. These results are in particular relevant for current and planned near-IR high-precision spectroscopic programs.

The second part of this thesis deals with the detection and characterization of the planetary system around the weakly active M4.0 V dwarf star GJ 4276 using 100 precise radial velocities obtained with CARMENES. A generalized Lomb-Scargle periodogram analysis revealed the presence of a signal at 13.35 d with a FAP below 0.1 %. To check whether this signal is not modulated by stellar activity, the periodograms of several activity indicators were examined. None of the indicators revealed a link between stellar activity and the supposed planetary signal. Furthermore, the stellar rotation period of  $\sim 64$  d was determined using photometry from MEarth, ASAS-SN, and T150. No evidence for additional planetary companions was found in the radial velocity data.

To determine the orbital parameters of the system, three Keplerian models were fitted to the radial velocity measurements, a single-planet on a circular orbit, a single-planet on an eccentric orbit, and two planets on circular orbits with a period ratio 2:1. The fit qualities of the circular planet model and the more complex models were compared by means of likelihood ratio tests. These tests indicate that the circular single-planet solution can be excluded with high confidence. An in-depth statistical analysis based on likelihood ratio tests using simulated data sets derived from the best-fit eccentric and the two-planet model showed that none of the two scenarios can be rejected. Based on the single-planet eccentric model, it was found that the planet GJ 4276 b is a Neptune-like planet with a minimum mass of  $\sim 16 M_{\oplus}$ , an orbital period of 13.4 d, a semi-major axis of 0.08 au, and an eccentricity of 0.37.

# Bibliography

- Alonso-Floriano, F. J., Morales, J. C., Caballero, J. A., et al. 2015, in *A&A*, 577, A128
- Anglada-Escudé, G., Amado, P. J., Barnes, J., et al. 2016, in *Nature*, 536, 437
- Anglada-Escudé, G. & Butler, R. P. 2012, in *Astrophys. Journal Supplement*, 200, 15
- Artigau, É., Astudillo-Defru, N., Delfosse, X., et al. 2014, in *Society of Photo-Optical Instrumentation Engineers (SPIE) Conference Series*, Vol. 9149, in *Proc. SPIE*, 914905
- Auvergne, M., Bodin, P., Boissard, L., et al. 2009, in *A&A*, 506, 411
- Bailey, J., Simpson, A., & Crisp, D. 2007, in *Proc. SPIE*, 119, 228
- Bakos, G., Noyes, R. W., Kovács, G., et al. 2004, in *Proc. SPIE*, 116, 266
- Ballard, S. & Johnson, J. A. 2016, in *Astrophys. Journal*, 816, 66
- Baranne, A., Queloz, D., Mayor, M., et al. 1996, in *A&A Supplement*, 119, 373
- Bauer, F. F., Zechmeister, M., & Reiners, A. 2015, in *A&A*, 581, A117
- Bean, J. L., Seifahrt, A., Hartman, H., et al. 2010, in *Astrophys. Journal*, 713, 410
- Beaulieu, J. P., Bennett, D. P., Fouqué, P., et al. 2006, in *Nature*, 439, 437
- Bedell, M., Hogg, D. W., Foreman-Mackey, D., Montet, B. T., & Luger, R. 2019, in *Astronomical Journal*, 158, 164
- Bertaux, J. L., Lallement, R., Ferron, S., Boonne, C., & Bodichon, R. 2014, in *A&A*, 564, A46
- Bond, I. A., Udalski, A., Jaroszyński, M., et al. 2004, in *Astrophys. Journal*, 606, L155
- Bonfils, X., Delfosse, X., Udry, S., et al. 2013, in *A&A*, 549, A109
- Bowler, B. P. 2016, in *Proc. SPIE*, 128, 102001
- Burke, C. J., Christiansen, J. L., Mullally, F., et al. 2015, in *Astrophys. Journal*, 809, 8
- Burrows, A., Sudarsky, D., & Hubeny, I. 2004, in *Astrophys. Journal*, 609, 407

- Butler, R. P., Marcy, G. W., Fischer, D. A., et al. 1999, in *Astrophys. Journal*, 526, 916
- Butler, R. P., Marcy, G. W., Williams, E., et al. 1996, in *Proc. SPIE*, 108, 500
- Caballero, J. A., Cortés-Contreras, M., Alonso-Floriano, F. J., et al. 2016, in 19th Cambridge Workshop on Cool Stars, Stellar Systems, and the Sun (CS19), Cambridge Workshop on Cool Stars, Stellar Systems, and the Sun, 148
- Campbell, B. & Walker, G. A. H. 1979, in *Proc. SPIE*, 91, 540
- Charbonneau, D., Brown, T. M., Latham, D. W., & Mayor, M. 2000, in *Astrophys. Journal*, 529, L45
- Chauvin, G., Lagrange, A. M., Dumas, C., et al. 2004, in *A&A*, 425, L29
- Clough, S. A., Shephard, M. W., Mlawer, E. J., et al. 2005, in *Journal of Quantitative Spectroscopy and Radiative Transfer*, 91, 233
- Cortés-Contreras, M., Béjar, V. J. S., Caballero, J. A., et al. 2017, in *A&A*, 597, A47
- Cosentino, R., Lovis, C., Pepe, F., et al. 2012, in Society of Photo-Optical Instrumentation Engineers (SPIE) Conference Series, Vol. 8446, in *Proc. SPIE*, 84461V
- Crane, J. D., Shectman, S. A., Butler, R. P., et al. 2010, in Society of Photo-Optical Instrumentation Engineers (SPIE) Conference Series, Vol. 7735, in *Proc. SPIE*, 773553
- Cumming, A., Marcy, G. W., & Butler, R. P. 1999, in *Astrophys. Journal*, 526, 890
- Cunha, D., Santos, N. C., Figueira, P., et al. 2014, in *A&A*, 568, A35
- Dressing, C. D. & Charbonneau, D. 2013, in *Astrophys. Journal*, 767, 95
- Dressing, C. D. & Charbonneau, D. 2015, in *Astrophys. Journal*, 807, 45
- Dumusque, X., Udry, S., Lovis, C., Santos, N. C., & Monteiro, M. J. P. F. G. 2011, in *A&A*, 525, A140
- Endl, M., Cochran, W. D., Kürster, M., et al. 2006, in *Astrophys. Journal*, 649, 436
- Fischer, D. A., Anglada-Escude, G., Arriagada, P., et al. 2016, in *Proc. SPIE*, 128, 066001
- Fischer, D. A. & Valenti, J. 2005, in *Astrophys. Journal*, 622, 1102
- Fortier, A., Beck, T., Benz, W., et al. 2014, in Society of Photo-Optical Instrumentation Engineers (SPIE) Conference Series, Vol. 9143, in *Proc. SPIE*, 91432J
- Fulton, B. J., Petigura, E. A., Howard, A. W., et al. 2017, in *Astronomical Journal*, 154, 109
- Gaia Collaboration, Brown, A. G. A., Vallenari, A., et al. 2018, in *A&A*, 616, A1



- Giguere, M. J., Fischer, D. A., Payne, M. J., et al. 2015, in *Astrophys. Journal*, 799, 89
- Gonzalez, G. 1997, in *Monthly Notices of the Royal Astronomical Society*, 285, 403
- Gordon, I. E., Rothman, L. S., & Toon, G. C. 2011, *Journal of Quantitative Spectroscopy and Radiative Transfer*, 112, 2310
- Gray, D. F. 2005, *The Observation and Analysis of Stellar Photospheres*
- Gullikson, K., Dodson-Robinson, S., & Kraus, A. 2014, in *Astronomical Journal*, 148, 53
- Henry, G. W., Marcy, G. W., Butler, R. P., & Vogt, S. S. 2000, in *Astrophys. Journal*, 529, L41
- Horrobin, F. & Rein, H. 2019, in *Monthly Notices of the Royal Astronomical Society*, 2221
- Howard, A. W. 2013, *Science*, 340, 572
- Howard, A. W., Marcy, G. W., Johnson, J. A., et al. 2010, *Science*, 330, 653
- Huélamo, N., Figueira, P., Bonfils, X., et al. 2008, in *A&A*, 489, L9
- Jeffers, S. V., Schöfer, P., Lamert, A., et al. 2018, in *A&A*, 614, A76
- Johnson, J. A., Butler, R. P., Marcy, G. W., et al. 2007, in *Astrophys. Journal*, 670, 833
- Kausch, W., Noll, S., Smette, A., et al. 2015, in *A&A*, 576, A78
- Koch, D. G., Borucki, W. J., Basri, G., et al. 2010, in *Astrophys. Journal*, 713, L79
- Konacki, M., Torres, G., Jha, S., & Sasselov, D. D. 2003, in *Nature*, 421, 507
- Kürster, M., Endl, M., Rouesnel, F., et al. 2003, in *A&A*, 403, 1077
- Lallement, R., Bertin, P., Chassefiere, E., & Scott, N. 1993, in *A&A*, 271, 734
- Laughlin, G., Bodenheimer, P., & Adams, F. C. 2004, in *Astrophys. Journal*, 612, L73
- Lin, D. N. C., Bodenheimer, P., & Richardson, D. C. 1996, in *Nature*, 380, 606
- Livingston, W. & Wallace, L. 1991, *An atlas of the solar spectrum in the infrared from 1850 to 9000 cm<sup>-1</sup> (1.1 to 5.4 micrometer)*
- Mahadevan, S., Ramsey, L. W., Terrien, R., et al. 2014, in *Society of Photo-Optical Instrumentation Engineers (SPIE) Conference Series*, Vol. 9147, in *Proc. SPIE*, 91471G
- Maiolino, R., Rieke, G. H., & Rieke, M. J. 1996, in *Astronomical Journal*, 111, 537

- Marcy, G., Butler, R. P., Fischer, D., et al. 2005, *Progress of Theoretical Physics Supplement*, 158, 24
- Mayor, M., Marmier, M., Lovis, C., et al. 2011, arXiv e-prints, arXiv:1109.2497
- Mayor, M., Pepe, F., Queloz, D., et al. 2003, *The Messenger*, 114, 20
- Mayor, M. & Queloz, D. 1995, in *Nature*, 378, 355
- Morales, J. C., Mustill, A. J., Ribas, I., et al. 2019, *Science*, 365, 1441
- Muterspaugh, M. W., Lane, B. F., Kulkarni, S. R., et al. 2010, in *Astronomical Journal*, 140, 1657
- Nagel, E., Czesla, S., Schmitt, J. H. M. M., et al. 2019, in *A&A*, 622, A153
- National Academies of Sciences, E. & Medicine. 2018, *Exoplanet Science Strategy* (Washington, DC: The National Academies Press)
- Nortmann, L., Pallé, E., Salz, M., et al. 2018, *Science*, 362, 1388
- Nutzman, P. & Charbonneau, D. 2008, in *Proc. SPIE*, 120, 317
- Pepe, F., Lovis, C., Ségransan, D., et al. 2011, in *A&A*, 534, A58
- Pepe, F., Mayor, M., Galland, F., et al. 2002, in *A&A*, 388, 632
- Pepe, F. A., Cristiani, S., Rebolo Lopez, R., et al. 2010, in *Society of Photo-Optical Instrumentation Engineers (SPIE) Conference Series*, Vol. 7735, in *Proc. SPIE*, 77350F
- Perryman, M. 2011, *The Exoplanet Handbook*
- Perryman, M., Hartman, J., Bakos, G. Á., & Lindgren, L. 2014, in *Astrophys. Journal*, 797, 14
- Plavchan, P., Latham, D., Gaudi, S., et al. 2015, arXiv e-prints, arXiv:1503.01770
- Pollacco, D. L., Skillen, I., Collier Cameron, A., et al. 2006, in *Proc. SPIE*, 118, 1407
- Quirrenbach, A., Amado, P. J., Caballero, J. A., et al. 2016, in *Society of Photo-Optical Instrumentation Engineers (SPIE) Conference Series*, Vol. 9908, in *Proc. SPIE*, 990812
- Quirrenbach, A., Amado, P. J., Mandel, H., et al. 2010, in *Society of Photo-Optical Instrumentation Engineers (SPIE) Conference Series*, Vol. 7735, in *Proc. SPIE*, 773513
- Quirrenbach, A., Amado, P. J., Ribas, I., et al. 2018, in *Society of Photo-Optical Instrumentation Engineers (SPIE) Conference Series*, Vol. 10702, in *Proc. SPIE*, 107020W
- Rauer, H., Catala, C., Aerts, C., et al. 2014, *Experimental Astronomy*, 38, 249

- Reiners, A., Bean, J. L., Huber, K. F., et al. 2010, in *Astrophys. Journal*, 710, 432
- Reiners, A., Ribas, I., Zechmeister, M., et al. 2018a, in *A&A*, 609, L5
- Reiners, A., Zechmeister, M., Caballero, J. A., et al. 2018b, in *A&A*, 612, A49
- Ricker, G. R., Winn, J. N., Vanderspek, R., et al. 2015, *Journal of Astronomical Telescopes, Instruments, and Systems*, 1, 014003
- Rothman, L. S., Gordon, I. E., Barbe, A., et al. 2009, in *Journal of Quantitative Spectroscopy and Radiative Transfer*, 110, 533
- Rudolf, N., Günther, H. M., Schneider, P. C., & Schmitt, J. H. M. M. 2016, in *A&A*, 585, A113
- Sahlmann, J., Lazorenko, P. F., Ségransan, D., et al. 2014, in *A&A*, 565, A20
- Salz, M., Czesla, S., Schneider, P. C., et al. 2018, in *A&A*, 620, A97
- Santos, N. C., Israelian, G., & Mayor, M. 2004, in *A&A*, 415, 1153
- Schmitt, J. H. M. M., Fleming, T. A., & Giampapa, M. S. 1995, in *Astrophys. Journal*, 450, 392
- Seager, S. 2010, *Exoplanets*
- Seager, S. & Mallén-Ornelas, G. 2003, in *Astrophys. Journal*, 585, 1038
- Seifahrt, A., Käufel, H. U., Zängl, G., et al. 2010, in *A&A*, 524, A11
- Setiawan, J., Henning, T., Launhardt, R., et al. 2008, in *Nature*, 451, 38
- Smette, A., Sana, H., Noll, S., et al. 2015, in *A&A*, 576, A77
- Tonry, J. & Davis, M. 1979, in *Astronomical Journal*, 84, 1511
- Tsapras, Y. 2018, *Geosciences*, 8, 365
- Tuomi, M., Jones, H. R. A., Barnes, J. R., Anglada-Escudé, G., & Jenkins, J. S. 2014, in *Monthly Notices of the Royal Astronomical Society*, 441, 1545
- Vacca, W. D., Cushing, M. C., & Rayner, J. T. 2003, in *Proc. SPIE*, 115, 389
- Vogt, S. S., Allen, S. L., Bigelow, B. C., et al. 1994, in *Society of Photo-Optical Instrumentation Engineers (SPIE) Conference Series*, Vol. 2198, in *Proc. SPIE*, ed. D. L. Crawford & E. R. Craine, 362
- Widemann, T., Bertaux, J. L., Querci, M., & Querci, F. 1994, in *A&A*, 282, 879

Williams, I. P. & Cremin, A. W. 1968, in *Quarterly Journal of the Royal Astronomical Society*, 9, 40

Wright, J. T., Marcy, G. W., Howard, A. W., et al. 2012, in *Astrophys. Journal*, 753, 160

Zechmeister, M., Reiners, A., Amado, P. J., et al. 2018, in *A&A*, 609, A12

## **Eidesstattliche Versicherung / Declaration on oath**

Hiermit versichere ich an Eides statt, die vorliegende Dissertationsschrift selbst verfasst und keine anderen als die angegebenen Hilfsmittel und Quellen benutzt zu haben.

Die eingereichte schriftliche Fassung entspricht der auf dem elektronischen Speichermedium.

Die Dissertation wurde in der vorgelegten oder einer ähnlichen Form nicht schon einmal in einem früheren Promotionsverfahren angenommen oder als ungenügend beurteilt.

---

Ort, Datum

---

Unterschrift